"MOLECULAR SPECTROSCOPY AND DYNAMICS OF REACTIVE CHEMICAL INTERMEDIATES STUDIED USING LASER INDUCED FLUORESCENCE (LIF), SINGLE VIBRONIC LEVEL (SVL) EMISSION AND RESONANCE ENHANCED MULTIPHOTON IONIZATION (REMPI) SPECTROMETRY."

Lloyd Godfrey Muzangwa
Marquette University

"MOLECULAR SPECTROSCOPY AND DYNAMICS OF REACTIVE CHEMICAL INTERMEDIATES STUDIED USING LASER INDUCED FLUORESCENCE (LIF), SINGLE VIBRONIC LEVEL (SVL) EMISSION AND RESONANCE ENHANCED MULTIPHOTON IONIZATION (REMPI) SPECTROMETRY."

by

MUZANGWA LLOYD. G, BSc. (HONS.) BIOCHEMISTRY

A dissertation submitted to the Faculty of the Graduate School,
Marquette University,
In partial fulfillment of the requirements for the
Degree of Doctor of Philosophy

Milwaukee, Wisconsin, USA

May 2013

ABSTRACT

In the studies of complex chemical processes, it is necessary to postulate mechanisms involving transient intermediates such as radicals, ions, and pre-reactive complexes so that we can better understand and utilize them. The detection and characterization of these intermediates affords in ideal cases determination of the detailed chemical mechanism, which, in turn, can permit the development of rational strategies for removing undesired products and enhancing the yield of the desired species. This dissertation describes spectroscopic studies of transient molecules and molecular complexes. Laser Induced Fluorescence (LIF), Single Vibronic Level (SVL) emission and Resonance Enhanced Multiple Photon Ionization (REMPI) spectroscopy has been used to probe the electronic states of NiI, NiBr, NiCl, CCN and chlorobenzene clusters $(ClBz)_n$ where n = 1-4. In this work, term energies and a complete set of vibrational parameters were derived for all the electronic states accessible for NiI, NiBr, NiCl and CCN. These vibrational parameters were compared to the recent high level *ab initio* calculations. REMPI spectra of chlorobenzene clusters formed in a He/Ar supersonic jet were obtained. Different types of non-covalent interactions (π-π stacking, CH/π interactions, and halogen bonding) were found to be in operation in the ClBz clusters. To rationalize the experimental results, the clusters were characterized computationally using Density Functional Theory (DFT) and Time-Dependent DFT methods in combination with correlation consistent basis sets.

ACKNOWLEDGMENTS

Isaac Newton once said "If I have been able to see further than others, it is because I have stood on the shoulders of giants". I would like to thank my supervisor Dr Scott A. Reid who has the attitude and the substance of a genius for his mentorship, guidance, patience, leadership and his depth of understanding in the subject of my research. I would also like to thank my committee members Dr Daniel Sem, Dr James Kincaid and Dr Qadir Timerghazin for their support and mentorship and lastly but not least my lab mates for their persistent help and support.

TABLE OF CONTENT

LIST OF TABLES

LIST OF FIGURES

LIST OF ABBREVIATIONS

SVL: Single Vibronic Level

LIF: Laser Induced Fluorescence

REMPI: Resonance Enhanced Multiple photon Ionization

R2PI: Resonant Two Photon Ionization

R2C2PI: Resonant Two Color Two Photon Ionization

DFT: Density Functional Theory

MP2: Møller–Plesset perturbation theory

DF: Dispersed fluorescence

BO: Born-Oppenheimer (BO) approximation

FC: Franck- Condon

RT: Renner-Teller

TDDFT: Time-dependent density functional theory

TOF: Time-of-flight

VUV: Vacuum- Ultraviolet

ZPE: Zero Point Energy (ZPE),

BSSE: Basis Set Superposition Error

 [13.9]: Notation representing 13 900 cm^{-1}

Chapter 1.   INTRODUCTION

1.1. Reactive Chemical Intermediates

A chemical reactive intermediate is a molecular entity that is formed from the reactants (or proceeding intermediates) and reacts further to give the directly observed products of a chemical reaction.[1] Most chemical reactions are stepwise, that is they take more than one elementary step to complete. Reactive chemical intermediates are usually short lived and are very difficult to isolate. Also, owing to the short lifetime, they do not remain in the product mixture.[2-4] Reactive chemical intermediates include species such as radicals, carbenes and ions which are shown in Figure 1.1.

Most chemical processes including not only laboratory and industrial chemical syntheses but also those which occur in flames, propellant systems, the initiation of energetic materials, atmospheric pollution, chemical vapor deposition, and plasma processing consist of a complicated sequence of interrelated reactions in which neutral and charged molecular fragments play essential roles.[5-11] Although these fragments may be present in only very small concentration, they are highly reactive. If a specific molecular fragment is removed from the system, as by introducing a scavenger molecule, the reactions in which that fragment participates stop.[8,10] However, other parts of the overall process continue, resulting in very significant changes in product distribution and yield.[8,10]

In recent years, there has been great progress in the development of techniques suitable for monitoring chemical reaction intermediates. Molecular spectroscopy is especially well suited to this task.[5,8-10] A wide variety of recently developed laser-based spectroscopic detection schemes are not only highly sensitive but also space and time specific.[8,10]

This dissertation provides a comprehensive study of transient intermediates including radicals, carbenes, and pre-reactive complexes using molecular spectroscopy techniques of Laser Induced Fluorescence (LIF), Single Vibronic Level (SVL) emission and Resonance Enhanced Multiple Photon Ionization (REMPI) spectroscopy.

1.1.1.   Radicals

Radicals (often referred to as free radicals) are open shell atoms, molecules or ions with an unpaired electron. Free radicals may have positive, negative, or zero charge. One of the fundamental tenets of molecular structure and bonding is that closed-shell electronic configurations are stable. The corollary to this principle is that species with unpaired electrons - radicals - are transient or reactive intermediates. With some exceptions, these unpaired electrons cause radicals to be highly chemically reactive.

Most radicals may be considered to have arisen by homolytic cleavage of normal electron-pair bonds, every cleavage having produced two separate entities, each of which contains a single, unpaired electron from the broken bond (in addition to all the rest of the normal, paired electrons of the atoms).

Certain free radicals are stabilized by their peculiar structures; they exist for appreciable lengths of time, given the right conditions. They are many types of radicals, however, including such simple ones as those studied in this work, including NiX (I, Br, Cl, F.) shown in Figure 1.1, and CCN radical.

1.1.1.1. Formation and Detection of Radicals

Virtually all chemical bonds are made up of two electrons, and bonds therefore can break in two different ways. In the first, both electrons in the bond remain attached to one of the fragments:

$$A \text{----} B \text{ ------>} A^+ + :B^-$$
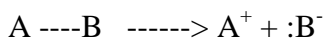
Since the two fragments are differently charged, this process is called heterolysis, and the charged fragments are of course called ions. In the second bond-breaking process, the two electrons in the bond divide symmetrically:

$$A \text{----} B \text{ -----> } A^{\cdot} + B^{\cdot}$$
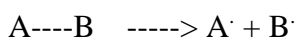
This process is called homolysis and the fragments are radicals.

Most radicals are so reactive that they normally are difficult to detect. However, the presence and nature of even these reactive radicals can frequently be detected by the magnetic properties due to the odd electron. The earliest method of detecting radical species was by magnetic susceptibility measurements. Substances with unpaired electrons are paramagnetic and interact with a magnetic field. In 1945 a technique was invented by Zavoisky which directly measures the para-magnetism of an odd electron.[12] The method is called electron spin resonance (ESR).[12] Radicals show characteristic spectroscopic properties and reactivity in their ground and excited states. Since they are unstable and short-lived, their spectroscopic properties and reactions have to be examined through suitably designed experimental procedures, such as flash photolysis and matrix isolation spectroscopy, to mention a two examples.[13]

The invention of the laser has made it possible to study radicals using the very sensitive and selective detection methods such as laser-induced fluorescence (LIF) and Dispersed Fluorescence (DF) spectroscopy which are described in this dissertation. Thanks to these and related advances, a large amount of experimental data have been accumulated for various kinds of radicals, noting that a highly accurate theoretical analysis has become an indispensable tool for obtaining a detailed interpretation of these data.

1.1.2. Metal Containing Intermediates

When a reaction intermediates contains a metal (usually transition metals), it is called a metal containing intermediate. These metal containing intermediates play a key role in many chemical processes for example breaking the C-C or C-H bonds.[14,15] Chemists have long sought means to selectively break, or activate, the C-C and C-H bonds of alkanes in low-energy conditions. Cracking of alkanes by metal catalyst, usually at high temperature, has a long history.[14] The making and breaking of C-C-bonds is of central importance in organic chemistry, for example certain transition metal cations (M^+ and M^{2+}) break the C-C or C-H bonds(or both) of alkenes at 300 K.[14] Frequently, these reactions proceed only in the presence of an organometallic catalyst whereby those containing transition metals are of particular importance. Familiar examples are the Ziegler polymerization, the metathesis reaction as well as acetylene and olef in cyclooligomerization.[16] In order to understand the mechanism of these reactions it is advantageous to isolate and determine the structure of intermediates involved and this has indeed been carried out for many reactions.[16] For example, most of the 3d-series cations Sc^+ through Ni^+ react with propane and larger alkanes, leading to products from H_2 or CH_4 elimination.[14] An example of a Nickel containing intermediate is also shown in Figure 1.1.

1.1.3. Carbenes

A carbene is a highly reactive organic molecule with a divalent carbon atom, where the carbene carbon is linked to two adjacent groups by covalent bonds, and possesses two nonbonding electrons. Carbenes are essential transient molecules that are implicated in a wide variety of chemical processes, including organic and organometallic reactions, combustion, stratospheric and interstellar chemistry.[17-21] Considering a prototype carbene CH_2, the carbon atom can be either linear or bent, each geometry describable by a certain degree of hybridization. The linear geometry implies an sp-hybridized carbene center with two nonbonding degenerate orbitals.

Bending the molecule breaks this degeneracy and the carbon atom adopts sp^2-type hybridization. The chemistry of carbenes is fascinating because the divalent carbon gives rise to singlet and triplet configurations of similar energy but very different chemical reactivity.[22-32] Figure 1.1 illustrates a representation of a singlet and a triplet carbene.

1.1.4. Ions

An ion is an atom or molecule in which the total number of electrons is not equal to the total number of protons, giving the atom or molecule a net positive or negative electrical charge. Ions can be created by both chemical and physical means.

In chemical terms, if a neutral atom or molecule loses one or more electrons, it has a net positive charge and is known as a cation. If an atom gains electrons, it has a net negative charge and is known as an anion. An ion consisting of a single atom is an monatomic ion; if it consists of two or more atoms, it is a molecular or polyatomic ion. There are additional names used for ions with multiple charges. For example, an ion with a −2 charge is known as a dianion and an ion with a +2 charge is known as a dication. A zwitterion is a neutral molecule with positive and negative charges at different locations within that molecule. Examples of monohalocarbocation and halobenzene cation are also presented in Figure 1.1.
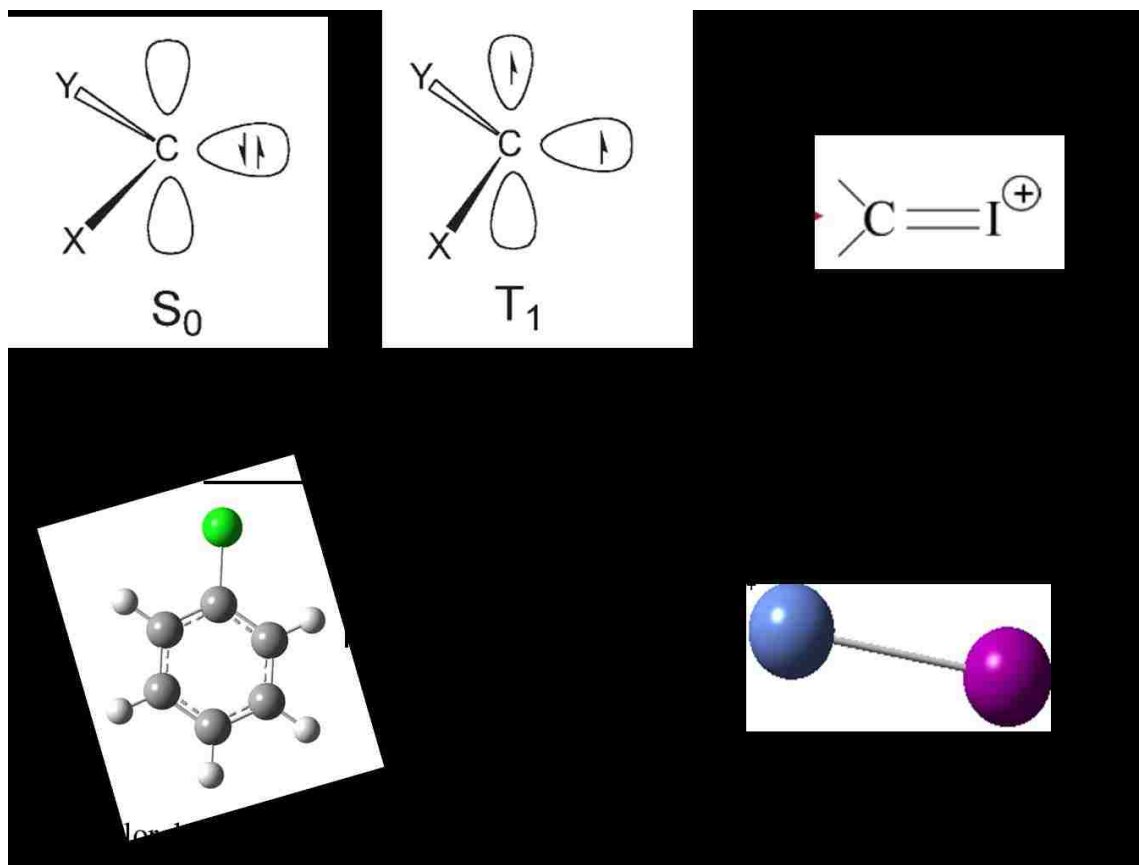
Figure 1.1 Representative examples of Reactive Chemical Intermediates.

1.2. Outline of Report

The outline of this report is as follows, Chapter 2 describes the experimental setup for Laser Induced Fluorescence (LIF), Single Vibronic Level (SVL) emission and Resonance Enhanced Multiple Photon Ionization (REMPI) spectroscopy, and the computational methods used in this work .Chapters 3 probes the SVL and LIF spectroscopy of the NiI, NiBr and NiCl and chapter 4 will analyzes the periodic trends observed for the set of the nickel monohalides series. Chapter 5 describes the SVL and LIF spectroscopy of CCN radical while chapter 6 interrogates the spectroscopy of halobenzene ions and their clusters using Resonance Enhanced Multiple Photon Ionization (REMPI) - TOF mass spectroscopy.

Chapter 2.   **EXPERIMENTAL AND COMPUTATIONAL METHODS**

(a) Experimental Challenges

(b) Laser Induced Fluorescence (LIF) Spectroscopy

(c) Single Vibronic Level (SVL) Emission spectroscopy

(d) Resonance Enhanced Multiphoton Ionization (REMPI)

2.1. Challenges of studying transient molecules

Theoretical calculations on molecules containing transient species have proven to be difficult. In particular the electronic structure of nickel monohalides and halobenzene clusters is challenging for theoretical models. This is because nickel and halobenzene clusters have high number of electrons which makes it computationally expensive to calculate. Also the fact that the low lying atomic states of nickel are energetically close; there is possible mixing of states and spin-orbit interaction which leads to pertubations.[33] In addition, for heavy elements one must properly treat relativistic effects, which have a substantial influence on the outer valence electrons.[34] Moreover NiX and CCN are open shell species, which are challenging to treat computational as they require methods which account for more electron-electron correlation.

However recent advances in methodology and the availability of fast super computers have now made it possible to also obtain quantitative information for many molecular systems containing transient molecules and transition metals.[35] Nowadays, *ab initio* calculations can yield more and more accurate potential-energy curves (PECs), and then the spectroscopic constants and vibrational properties of molecules can be reliably determined. *Ab initio* calculations thus, are an effective method to investigate properties of transient molecules.

From an experimental viewpoint this complexity is frequently exacerbated by states of high multiplicity and different isotopes with large nuclear spins and magnetic moments. Transient molecules therefore also represent a challenge to experimentalists. Another consequence of many low-lying states with different occupations of the nd, (n+1)s, and (n+l)p orbitals is the variety of bonding mechanisms that can occur.[36] These challenges may result in complicated spectrum that may lead to incorrect assignments if proper caution is not practiced.

2.2. Experimental Set up overview

The overall experimental setup for Single Vibronic Level (SVL) and laser induced fluorescence (LIF) can be pictured in Figure 2.1, and can be divided into three main categories; pulsed discharge, laser system and detection.
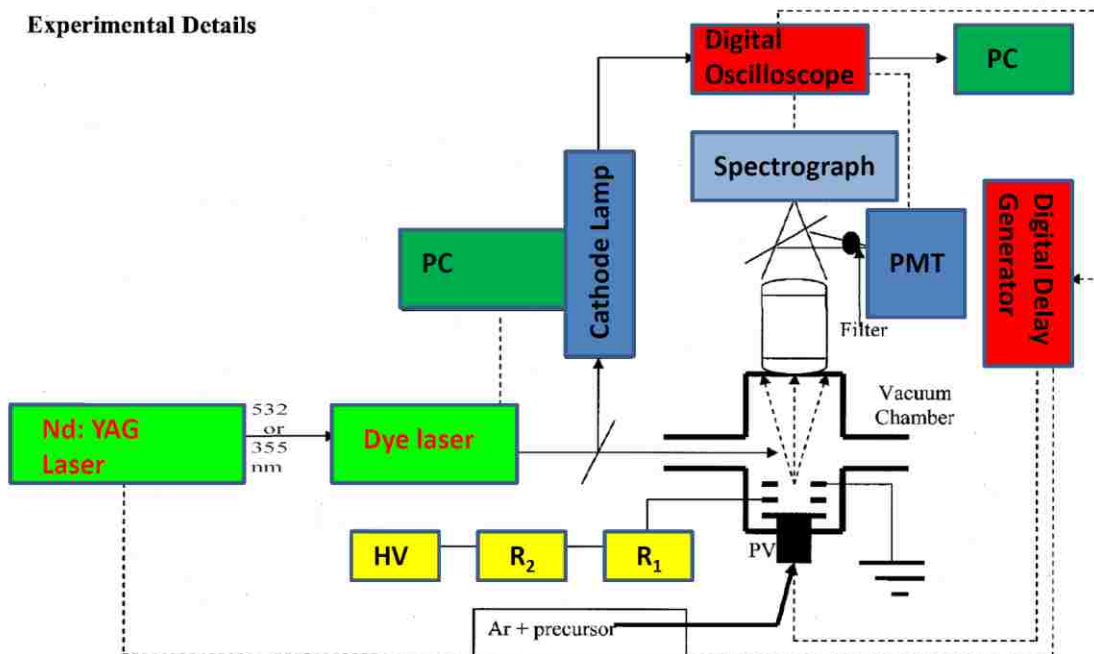
Figure 2.1: Generalized schematic layout of the Single Vibronic Level (SVL) emission and Laser Induced Fluorescence (LIF) experiment using pulsed lasers.

2.3. Pulsed discharge methods

In recent years, the pulsed jet discharge method has been extensively applied to examine the spectroscopy and dynamics of many species. Although fragmentation in the discharge source is less selective than photolysis, and the fragmentation efficiency is typically smaller,[37] the technique works well when matched with a selective and sensitive detection technique like LIF.

Figure 2.2 shows a picture of a discharge nozzle (General Valve Series 9, orifice diameter = 0.5 mm). A pulsed discharge nozzle can be operated simply in a DC mode, where a high DC voltage is applied and the entrance (exit) of the gas pulse into the channel turns on (off) the discharge. This design works well, since the background pressure in the vacuum chamber is insufficient to support a discharge in the absence of the gas pulse. However, one disadvantage of the DC discharge for fluorescence experiments is that the signal sits on top of large background from excited species in plasma(Ar*/He*). Figure 2.2 shows how to solve this problem, where a high voltage (HV) pulsed power supply is used to generate short HV pulse (10-50 μs) which is centered within the gas pulse. If the HV pulse is short enough, due to the distance between discharge and detection region (typically 1 cm) the discharge background and laser induced fluorescence can be separated in time, as shown in Figure 2.3. In this case, a short high-voltage pulse can be used to help discriminate against the discharge glow.

However by detecting with a gated boxcar integrator (which is a is an analogue technique which relies on the incoherent nature of any noise component to increase the signal to noise ratio of a repetitive input)[38] makes it possible to simultaneously collect two spectra of two species with different life times in one scan. Example of two spectra collected simultaneously for CCN radical using two different gates (short gate and long gate) is shown in Figure 2.4; Note in the lower trace of the long gate spectra, they are some additional features in that channel which can be attributed to C_2 Swan band system which can be identified in the spectrum.
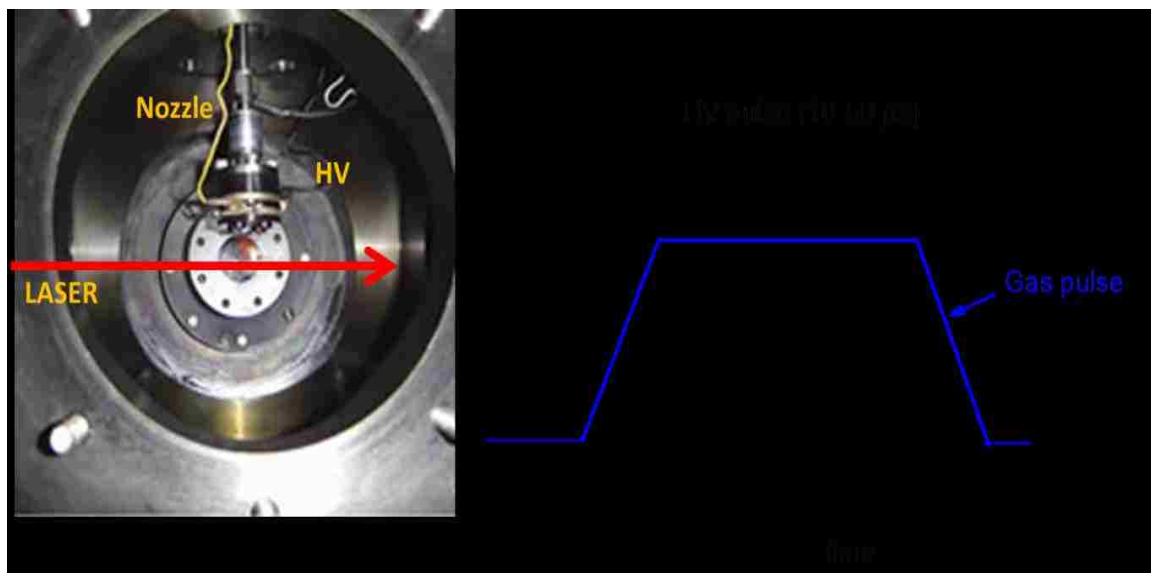
Figure 2.2: Schematic diagram illustrating pulsed discharge technique and high voltage (HV) pulser used to reduce background on laser induced fluorescence.
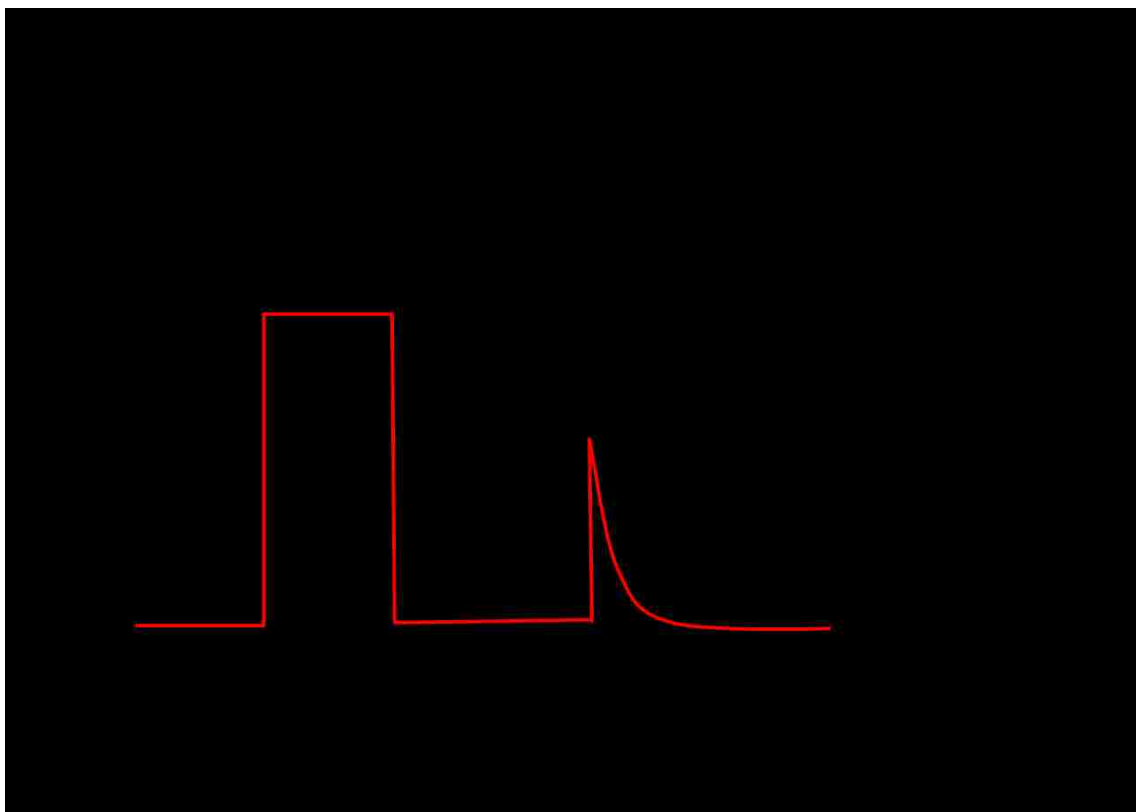
Figure 2.3: Schematic diagram illustrating how pulsed discharge technique and high voltage (HV) pulser separates in time the background and fluorescence.
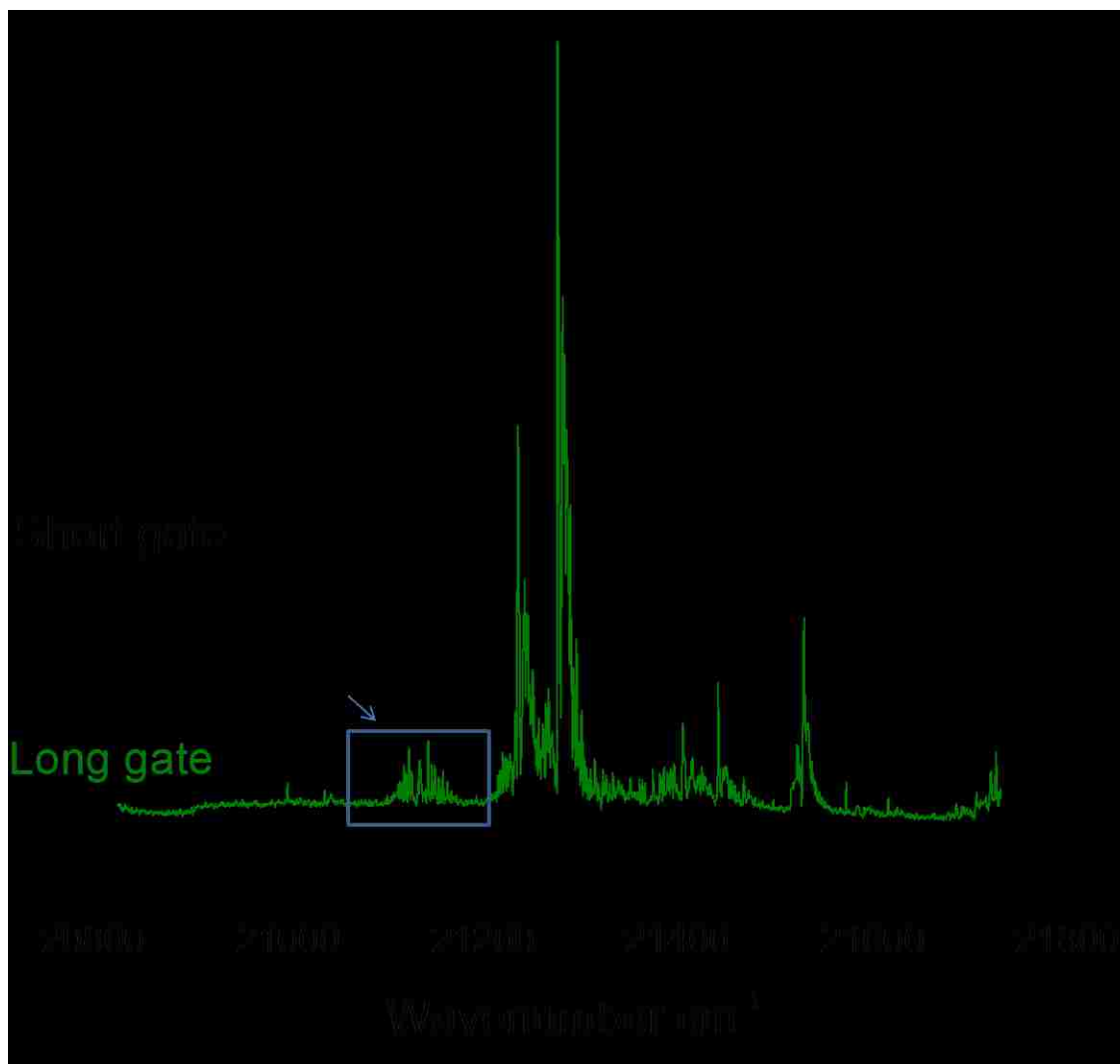
Figure 2.4: Low resolution laser induced fluorescence (LIF) spectrum of CCN using long gate (lower trace) and short gate (upper trace).

2.4. Laser Induced Fluorescence (LIF) Spectroscopy

Fluorescence-based methods have been very important in detection of various classes of transient species [32,39-56] also significant for detection of transition metal monohalides.[40-44,47,50,53,54,56]. Laser induced fluorescence (LIF) is a very sensitive, selective and background-free technique for fluorescing states. The advantage of performing LIF experiments is that it gives us rich information. We can get information on the excited state structure and symmetries; we can also get information on the excited state photo-physics on the molecule as well as the excited state vibrational frequencies.

2.5. Single Vibronic Level (SVL) Emission spectroscopy

In this technique, emission is dispersed by a spectrograph (with a grating) from a specific (laser-excited) upper state level. The emission spectrum obtained reveals the vibronic structure of the ground state. SVL emission has high sensitivity compared to IR absorption. First, two relatively strong electronic transitions are used, rather than a much weaker vibrational transition. Second, for molecules that undergo geometry change upon electronic excitation, the Franck-Condon factors for absorption and emission allow observation of long vibrational progressions in the mode that corresponds to the geometry change.

By using SVL emission spectroscopy the resulting spectrum, especially for transition metal monohalides which may have spectral congestion, can be cleaner because only a single, or a few, rotational levels in the upper electronic state are populated by the excitation laser. Selection of the vibronic level for study also gives a high degree of species specificity; that is, only transitions arising from the laser excited species will appear in the spectra. This will greatly simplify spectral analysis. We can also obtain information on the ground state structure and symmetries from SVL emission, as well as the ground state vibrational frequencies. Thus, SVL emission is a powerful method for the detection of highly excited vibrational energy levels in an excited state of a different symmetry, allowing fluorescence down to infrared-forbidden vibrational levels of the ground state. If the Frank-Condon factors are favorable, the SVL emission spectrum exhibits large progressions of highly excited vibrational levels.

Figure 2.5 displays a schematic representation of a typical Single Vibronic Level (SVL) emission experiment using a pulsed discharge source and charge-coupled device (CCD) equipped spectrograph.
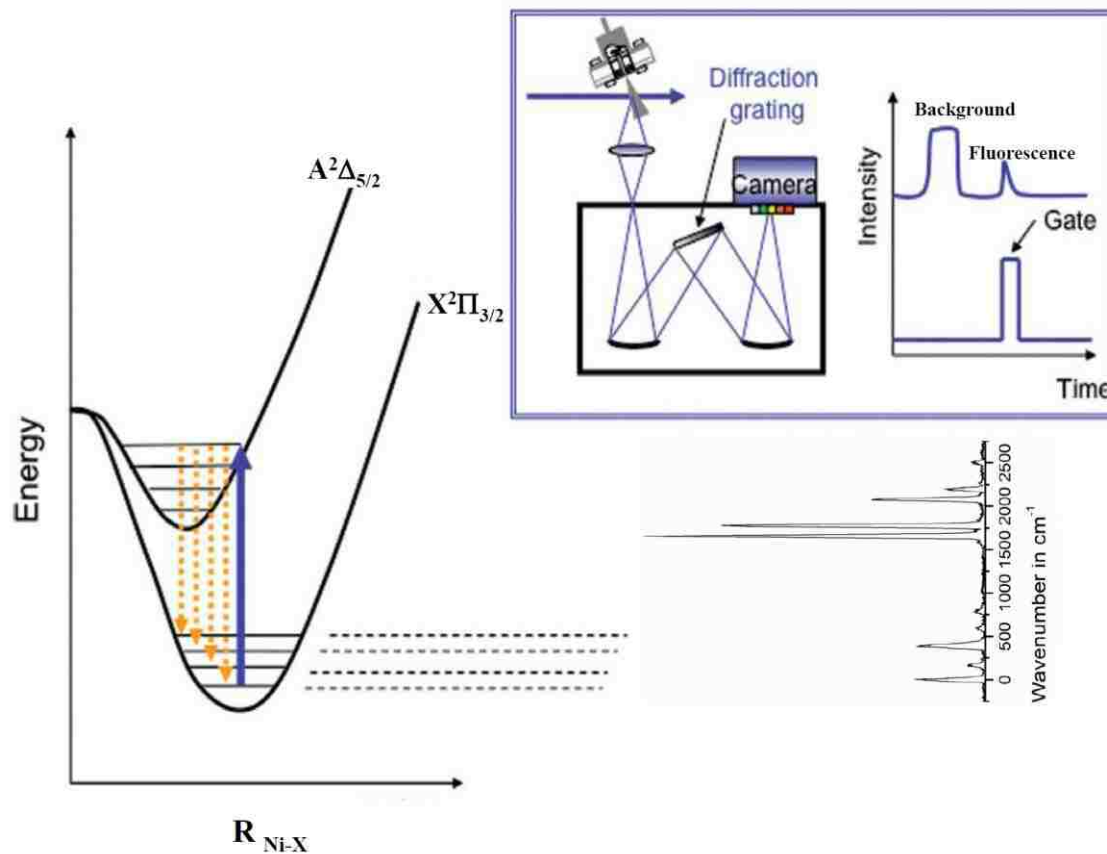
Figure 2.5 : Illustration of the SVL emission technique applied to probe the low-lying states of nickel monohalides. Modern spectrographs are usually equipped with a gated, intensified CCD detector as shown in the figure.

2.6. LIF and SVL experimental details

The laser system consisted of an etalon narrowed dye laser (Lambda-Physik Scanmate 2E) operating on dyes Coumarin 440 and Coumarin 460, pumped by the second or third harmonic (355 nm) of a Nd:YAG laser. The grating was scanned under computer control. A quartz window was used to direct a portion of the dye laser fundamental into a Fe-Ne and Fe-Ar hollow cathode lamp for absolute wavelength calibration using the optogalvanic effect; the optogalvanic and fluorescence signals were recorded simultaneously.

As also shown in Figure 2.1, these measurements utilized a mutually orthogonal geometry of laser, molecular beam, and detector, where the laser beam crossed the molecular beam at a distance of ~10 mm downstream. Fluorescence was collected and collimated by a f/2.4 plano-convex lens, and focused into the spectrograph using a f-matching f/3.0 plano-convex lens. Insertion of an aluminum mirror into the beam path at 45° allowed collection of the total fluorescence, which was filtered via an appropriate long-pass cutoff filter (Corion or Edmund Scientific) prior to striking a photomultiplier tube (PMT) detector (Oriel) held at typically ~ -1000 V. In acquiring emission spectra, the fluorescence signal was first optimized and the wavelength then set on the band of interest. The mirror was subsequently removed to allow fluorescence to enter the spectrograph.

A second removable mirror assembly was used to direct the output of a Fe:Ne and Fe:Ar hollow cathode lamp into the spectrograph for wavelength calibration; these spectra were typically obtained immediately before or after emission spectra. Background spectra were also obtained with the laser blocked to check for emission lines from species in the discharge. Calibration spectra were acquired with a slit width of 10 μm and 1000 shot accumulation; photon counting was not used. The emission spectra were typically acquired with a slit width of 100 - 160 μm, although spectra from intense bands were acquired with a narrower slit width. Lower and higher resolution spectra were obtained using, respectively, a 600 1/mm grating blazed at 500 nm and an 1800 1/mm holographic grating. The spectrograph was operated in a "step and glue" mode where the grating was sequentially stepped and the spectra recorded at each grating position in order to cover the entire spectral region of interest. Spectra were calibrated in each range by first fitting the Ar or Ne emission lines to a Gaussian line shape function, using Origin 7.5 software. The observed positions were then compared against the known values,[57] and the deviations fit to a second order polynomial to obtain a calibration curve which was applied to the corresponding emission spectrum. Bands in the emission spectra were also fit to a Gaussian line shape function. The uncertainty in the derived band positions was +/- 2cm^{-1}. The ground state energies were fit to an expression of the form:

$$G^0(v) = v_i \omega_i^0 + v_i^2 \, \omega_e x_e$$

2.7. Mass Spectrometry and Resonance Enhanced Multiple Photon Ionization (REMPI)

Mass spectrometry has been used for many years for quantitative and or qualitative analysis in the fields of petroleum chemistry, organic, inorganic chemistry, and gas analysis.[3,58-60] Chemists, biochemists, and pharmacologist have applied this technique with notable success to their particular structural determination problems.[58] The ability of mass spectrometer to separate and identify isotopes (elements with different atomic weights, but the same atomic number but has the same chemical properties) has aided physicist and chemists in achieving a better understanding of the atomic and molecular structure.[59]

The development of modern mass spectrometers has been related to advances in lasers, signal-processing technologies, ion optics and detection, fast and high performing electronics.[61] This has been particularly true for the time-of-flight (TOF) mass spectrometry,[61] which plays an increasingly important role in all of the biological research areas as well as ion reaction dynamics field.

Mass spectrometers can be characterized by the ionization sources, mass analyzers, and detectors that are used (Table 2.1). In general, they are made up of different components according to the intended use and sometimes even hybrids are possible. For example, resonance enhanced multiple photon ionization time of flight (REMPI-TOF-MCP) was used to study state-selected halobenzene ions.

Table 2.1   Classification of components consisting of mass spectrometer.

Ionization Methods	Electron ionization (EI)
	Chemical ionization (CI)
	Fast atom bombardment (FAB)
	Field Ionization (FI)
	Photoionization (PI)
	* Multiphoton ionization (MPI)
Mass Analyzers	Magnetic (B)
	Double-focusing (EB)
	Ion cyclotron resonance (ICR)
	Quadrupole (Q)
	Quadrupole ion trap (ITMS)
	Time-of-flight (TOF)
Detectors	Faraday cup
	Electron multiplier (EM)
	Photon multiplier (PM)
	Microchannel plate (MCP)
	Array detectors
	Image currents

2.7.1.   Ionization Methods

A molecule (*M*) can be generally ionized through interaction with the energetic electrons, particles, or photons.

$$M + E \rightarrow M^+ + e-$$
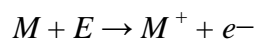
Here, ionization energy (*IE*) is defined as the minimal energy required for removal of an electron in that molecule. Ionizations can occur through various methods, such as electron ionization (EI), charge exchange ionization (CI), photoionization (PI), electrospray ionization (ESI), matrix-assisted laser desorption ionization (MALDI) and multiple photon ionization (MPI); these can be chosen, depending on the volatility, thermal stability, and physical state of the transient molecules.

2.8. Nonlinear optical phenomena

In general, most photochemical processes involve first the electronic transition by absorption or scattering of one or more photons, followed by nuclear motion on the excited electronic state(s), internal conversion to the ground electronic state, and finally relaxed into minima representing photoproducts. Practically, scattering and multiphoton processes require the intense light fields available only from lasers.

Multiphoton and light scattering processes are called nonlinear optical phenomena, because unlike stimulated absorption, they do not depend linearly on the excitation power.

2.9. Resonance Enhanced Multiphoton Ionization (REMPI)

Resonance enhanced multi photon ionization (REMPI) is a very sensitive technique for the gas-phase detection of many molecules. With a simple time-of-flight collection scheme, the created ions can be mass selected and counted with near unit efficiency, while background interference can be almost completely suppressed. The REMPI technique typically involves a resonant single or multiple photon absorption to an electronically excited intermediate state followed by another photon which ionizes the atom or molecule. If the absorption photon has the same wavelength as the excitation photon, the REMPI scheme is called Resonance Two Photon Ionization (R2PI). If the absorption photon has different wavelength as the excitation photon, then the scheme is known as Resonance Two Color Two Photon Ionization (R2C2PI). The difference between R2PI and R2C2PI scheme is illustrated in Figure 2.6. However they are also other REMPI schemes which involve more than two photons for example R3P, R3C3PI2 and so on. In addition REMPI provides useful spectroscopic information about neutral molecules and their ions that cannot be obtained from a single photon experiments.
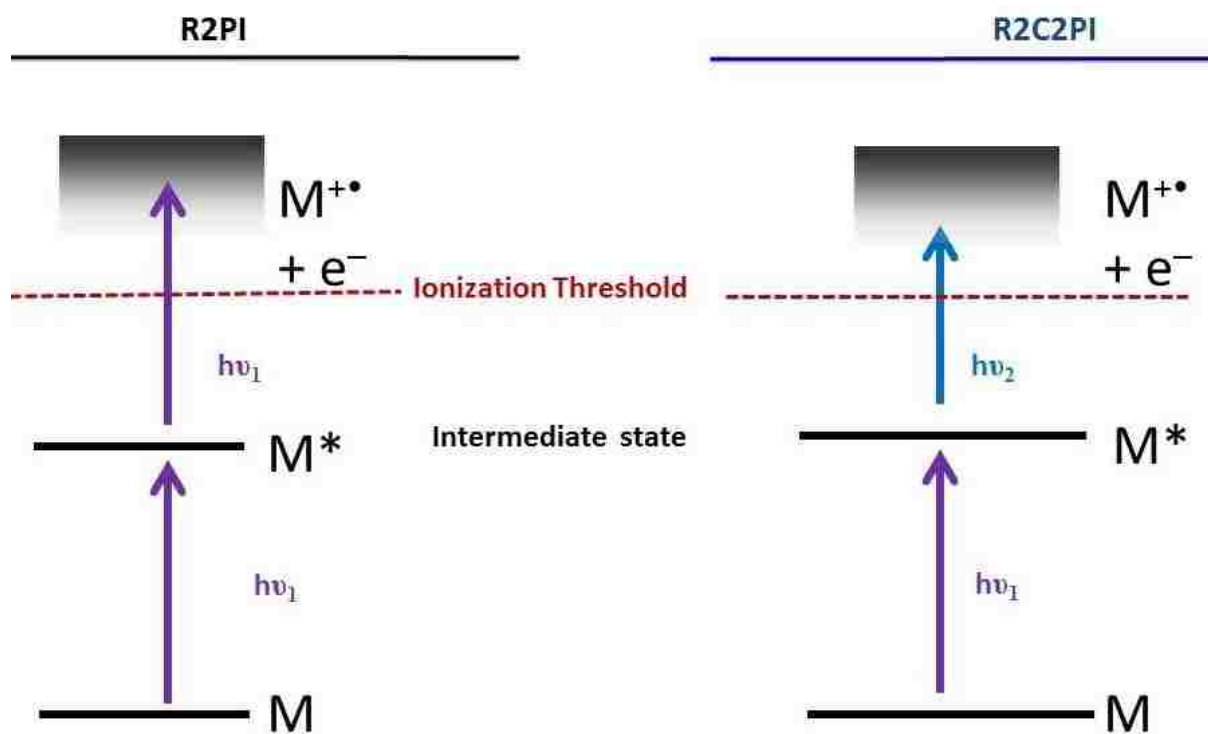
Figure 2.6 **:** Schematics representation of the R2PI and R2C2PI scheme.

2.10.   REMPI Experimental set up

Our experiments utilized a linear time-of-flight mass spectrometer (TOFMS) coupled with a supersonic molecular beam source based upon a General Valve pulsed nozzle. A schematic of the experimental apparatus is shown in figure Figure 2.7. A 1% mixture of the halobenzene precursor in He, generated by passing the high purity gas over a sample of halobenzene held in a temperature controlled bath, at a total pressure of typically ~ 1-2 bar was expanded from the 1.0 mm diameter nozzle of the pulsed valve, and passed through a 1.0 mm diameter skimmer into the differentially pumped flight tube of a one-meter linear TOFMS, similar to one described in our previous work.[62-64] The flight tube was evacuated by a 250 L/s turbo-molecular pump, with a gate valve used to isolate the detector, which was kept under vacuum at all times to minimize moisture on the MCP. The main chamber was evacuated with a water-baffled diffusion pump (Varian VHS-4). With the nozzle on, typical pressures were ~ 5 x 10^{-5} mbar (main chamber) and ~ 1 x 10^{-6} mbar (flight tube). The background pressure in the flight tube could be lowered further by liquid nitrogen cooling of the vacuum shroud; however, this was not required in the present experiments.
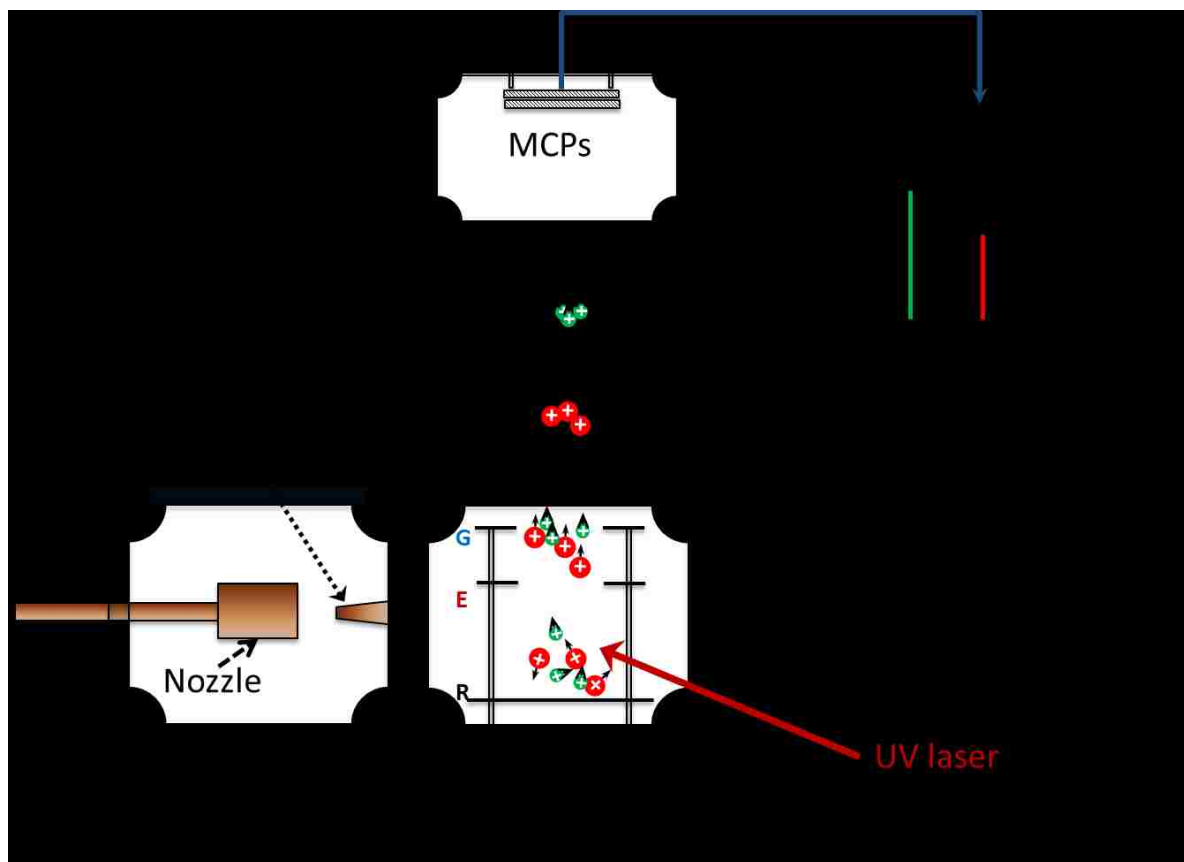
Figure 2.7: Schematic of the experimental apparatus used for the R2PI experiments.

2.11.   The Born-Oppenheimer approximation

To fully understand any system, the total energy must be derived. To determine the energy, the Schrödinger equation must be solved,

$$\widehat{H}\psi = E\psi$$

In which, $\widehat{H}$ is the Hamiltonian operator, ψ is the system's wavefunction, and E is the energy of the system. The Hamiltonian is an operator which describes the energy (both kinetic (T) and potential (V)) of a system in terms of the position and momentum operators. In order to solve equation for energy, approximations must be made. The Born-Oppenheimer (BO) approximation is based on the fact that the electrons are much lighter than the nuclei. This coupled with the fact that the magnitude of all the potential energy terms in the molecular Hamiltonian are approximately equal (i.e. electrons and nuclei experience similar forces), indicates that the electrons move much faster than the nuclei. As a result, the nuclei can be considered as stationary on the time scale of the electronic motion, and solve for the electronic ground-state first, and then calculate the energy of the system in that configuration and solve for the nuclear motion. This separation of electronic and nuclear motion is known as the Born-Oppenheimer approximation.[65]

The vibrational problem of a diatomic is simplified by the fact that there exists only a single mode, the displacement of the internuclear distance[2] R from its equilibrium value R_e in which the nuclear motion is several orders of magnitude slower than that of electrons. If this is repeated for a series of nuclear positions, a potential energy curve can be generated which describes the potential in which the nuclei move.

It is also important to note that within the B-O approximation, each electronic state of the molecule has its own characteristic potential energy curve. As a result each state has different characteristics (bond length, vibrational frequencies, rotational constants etc.). In the spirit of the Born-Oppenheimer (BO) approximation, the most probable transition in the absorption spectrum are the vertical transition as indicated in Figure 2.8.

In general, the greater the change in bond length upon excitation, the greater the number of vibrational states contributing to the progression. So in the absence of a change in geometric coordinates, no Frank-Condon progression is observed.

2.12.   The Frank-Condon principle

The Franck- Condon principle also deals with the relative timescales for electronic and nuclear motions. In an electronic transition, the electron will move from one orbital to the other. The timescale for this motion is much faster than that of nuclear motion. In other words, the nuclei are 'frozen' on the timescale of the transition.

The intensity of the transition is governed by the overlap of the wave-function of the ground state and the excited state which is responsible for the transition. Both excitation and emission intensities are governed by the Frank-Condon overlap of the two states involved in the transition. This phenomenon can be pictured in Figure 2.8.
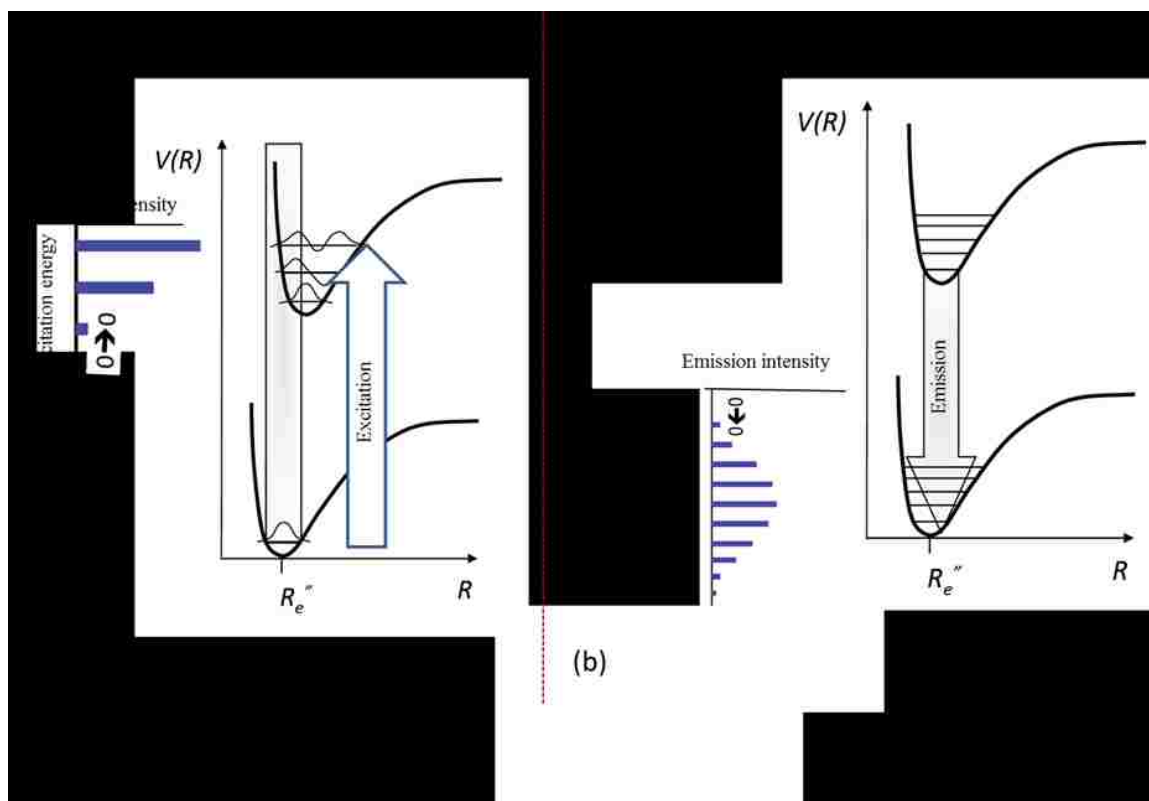
Figure 2.8 : Displaced potential energy curves leading to Frank-Condon progression in excited (a) and relaxed emission (b) spectrum.

2.13.   Renner-Teller (RT) effect

Most of the areas and methods of molecular physics and spectroscopy assume the validity of the Born-Oppenheimer approximation. The nuclei generally move much more slowly than the electrons, the frequencies associated with electronic transitions are much higher than vibrational frequencies, and one can consider separately the three types of molecular motion: electronic, vibrational, and rotational. These statements are no longer necessarily valid for electronic states which are degenerate or at least close to degeneracy, and the Born-Oppenheimer approximation breaks down.

Degenerate electronic states usually occur in molecules having a high degree of symmetry. The symmetric equilibrium geometry which causes the electronic degeneracy is, in general, lowered in the course of molecular vibrations, and this may lead to splitting of the potential. The molecular potential is usually expressed in terms of a polynomial expansion in displacements r, and, in nonlinear molecules, the linear terms may lead to coupling of the electronic and vibrational degrees of freedom. The resulting breakdown of the Born-Oppenheimer approximation is in this case known as the Jahn-Teller effect. In linear molecules the symmetry is lowered during bending vibrations. The results of this coupling in linear molecules are referred to as the Renner-Teller effect, or simply the Renner effect. The CCN radical is one of the prototypical examples for triatomic molecules exhibiting the Renner-Teller (RT) effect, which originates from coupling between the vibrational and electronic angular momenta.

2.14.   Computational Methods

2.14.1. Introduction

Computational chemistry (also known as molecular modeling) is the application of computer-based models to the simulation of chemical processes and the computation of chemical properties. Computational chemistry is a valuable tool for modern research to bypass tedious, time consuming and costly, and sometimes dangerous experiments. There are some properties of a molecule that can be obtained computationally more easily than by experimental means. Thus, many modern researchers are now using computational modeling to gain additional understanding of the compounds being examined. Some computational methods can be used to model not only stable molecules, but also short-lived, unstable intermediates and even transition states. In this way, they can provide more insight into the reaction and molecules and provide information which could be impossible to obtain through observation. [66] In general, modern research uses computational chemistry to predict, support and complement experimental results.

In particular for our research, we use various computational methods, always trying to get as accurate a result as possible, however we choose our methods and basis sets depending on the computational cost to the calculations, the parameters to be calculated and the nature of the system to be studied. Often we base our choice of method on literature precedent. The next section describes briefly the various methods used in our studies.

2.14.2. Hartree Fock

The Hartree Fock (HF) method is the most common *ab initio* method that is implemented in nearly every computational chemistry program.[67,68] The HF equation describes the many electron wavefunction as an antisymmetrized product (the slater determinant) of one-electron wavefunctions. The HF method can be pictured in the flow chart below.

Hartree-Fock Method
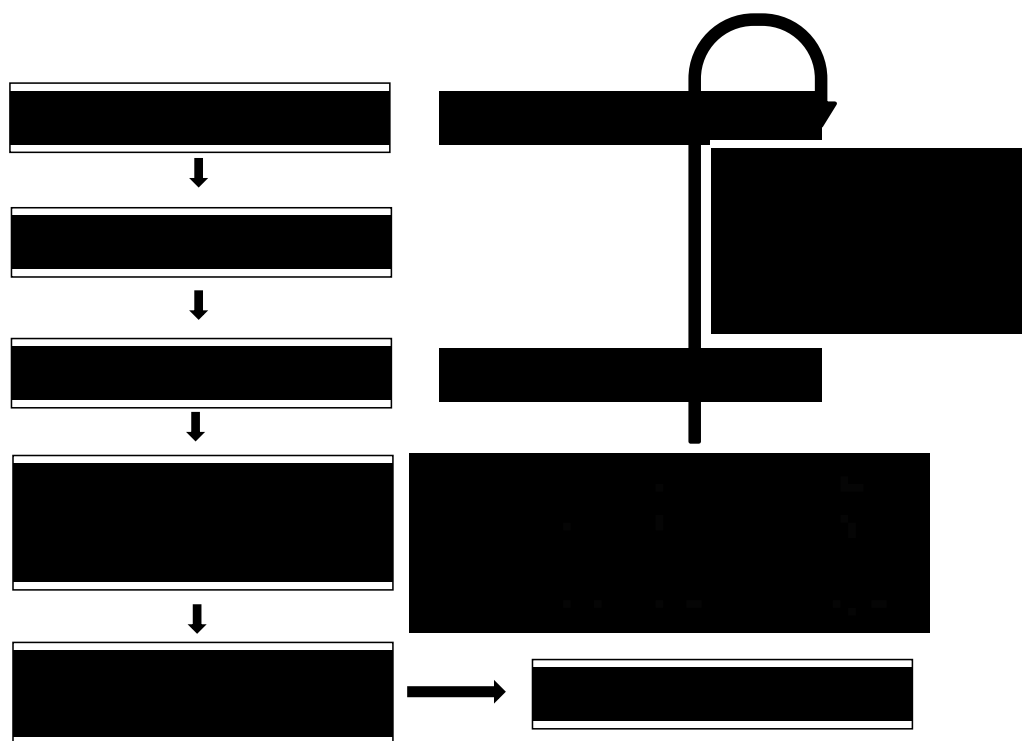
Each electron moves independently in the spin orbital space and it experience a Coulombic repulsion due to the average positions of electrons.[67] HF theory provides a very well defined energy, one which can be converged in the limit of an infinite basis set.[69]

The HF method will tend to give an energy which is too large, since the electron-electron repulsion is overestimated. This is because in the self-consistent field approach, we assume that the motion of the electrons is uncorrelated, so that each electron feels the average (mean) field of all other electrons. In the mean field approach, the effective potential for a given electron depends on the functional form of the orbitals for all other electrons. HF methods recover about 99% of the total energy; however, the 1% is comparable to the energy changes in chemical reactions and thus is very important.

2.14.3. The Møller -Plesset (MPn) Methods

The Møller–Plesset perturbation theory (MP) was published as early as 1934 by Christian Møller and Milton S. Plesset. Here, higher excitations are taken into account by a perturbation operator within the many-body perturbation theory. The HF problem is treated as the unperturbed wave function and their residual part of the Hamiltonian is treated as a perturbation.[70] Within the Perturbation theory, the Hamiltonian is partitioned as $H = H_0 + P$, where H_0 is an unperturbed HF Hamiltonian for which eigenfunctions can be found and P is the perturbation. The application of the perturbation theory is justified if the contribution of electron correlation energy (the 'perturbation') is small.[70] The Møller-Plesset (MP) methods are typically referred to by the acronym MPn, where *n* indicates the order at which the perturbation theory is truncated. MP methods (MP2, MP3, MP4,...) are implemented in many computational chemistry codes. Higher level MP calculations, generally only MP5, are possible in some codes.

However, they are rarely used because of their high cost. Prior to the widespread usage of the methods based on Density Functional Theory, the MP2 method was one of the least expensive ways to improve on Hartree-Fock and it was thus often the first correlation method to be applied to new problems. It can successfully model a wide variety of systems, and MP2 geometries are usually quite accurate. However, there are problems for which MP2 fails as well.[66]

2.14.4. Density Functional Methods

The recently acquired popularity of approximate DFT as a new method accounting for electron correlation stems, in large measure, from its computational ease. This makes it amenable to larger molecules at a fraction of the time required for HF or post-HF computations.[70] When compared to conventional quantum chemistry methods, Density functional Theory (DFT) is particularly appealing since it does not rely on the knowledge of the N-electron wave function but only of the electron density. DFT theory provides an expression for the ground state energy of a system of interacting electrons in an external potential as a function of the ground state electronic density.[71,72]

DFT methods offer many advantages such as adding some degree of electron correlation, providing good results at lower computational cost and being more robust than Hartree Fock for open shell system treatment.

However the DFT methods encounter some limitations like poor description of long range interactions, and the need to know the dependence of a chemical property on the density. [69] DFT methods are broadly classified into two methods: pure DFT and hybrid DFT. They are designated on the basis of type of correlation energy functional, the exchange energy functional, and potential.[67] The pure methods consist of BLYP, PW91 and SVWN5. Similarly, the hybrid DFT method consists of B3pw91, M06 and M06-2X.[67] Zhao and Truhlar have recently developed the M06 family of local (M06-L) and hybrid (M06, M06-2X) meta-GGA functionals that show promising performance for noncovalent interactions. [73-75]

2.14.5.   Time Dependent Density Functional Theory (TD-DFT)

Time-dependent density functional theory (TDDFT) is a quantum mechanical theory used in physics and chemistry to investigate the properties and dynamics of many-body systems in the presence of time-dependent potentials, such as electric or magnetic fields. Time-dependent density-functional theory (TDDFT) extends the basic ideas of ground-state density functional theory (DFT) to the treatment of excitations or more general time-dependent phenomena. TDDFT can be viewed an alternative formulation of time-dependent quantum mechanics but, in contrast to the normal approach that relies on wave-functions and on the many-body Schrödinger equation, its basic variable is the one-body electron density.[76]

The effect of such fields (electric or magnetic) on molecules and solids can be studied with TDDFT to extract features like excitation energies, frequency-dependent response properties, and photo-absorption spectra.

2.14.6. Gaussian-type basis sets

By definition, a basis set is a mathematical description of orbitals of a system, which is used for approximate theoretical calculation or modeling.[67] Different basis sets are used in computational chemistry, in order to derive chemical information by solving Schrodinger equation. Generally in electronic structure modeling, the most important factor is the number of basis functions to be used. The smallest number of basis function possible is called the minimum basis set.[67,69] In this case the hydrogen and helium atoms would require only one s-function to contain all the electrons. There are different types of basis sets, but most known are the Pople's and Dunning's basis sets.[69]

The Pople's basis sets are typically *split valence double-zeta* basis sets and this class includes basis sets such as 3-21G, 6-21G, etc. In last decade, Dunning and co-workers[69] developed another type of basis set called "*correlation consistent and polarization valence split basis sets*" with the generic acronym cc-pVnZ (n=D: double, T: triple, Q: quadruple).[69] The advantage of using these basis sets is that: (a) they include shells of polarization functions (d, f, g etc.) and (b) as their size increases, the calculated energy tend to converge to the complete basis set limit (CBS).[69]

However in order to calculate and treat anions, highly excited states, or supermolecular complexes which are more spatially diffused, the basis set has to be more flexible to allow a weakly bound electron to localize far from the remaining density. In this case, the basis set is augmented with diffuse functions, symbolized by "aug" prefix for the Dunning's basis sets and "+" sign for Pople's family. For instance, aug-cc-pVTZ basis set has f, d, p and s diffuse functions on the heavy atoms and d, p and s function on H and He atoms.[69]

Chapter 3.   SINGLE VIBRONIC LEVEL (SVL) EMISSION SPECTROSCOPY AND LASER INDUCED FLUORESCENCE (LIF) OF THE NICKEL MONOHALIDES

3.1. Introduction to Metal containing Monohalides

Spectroscopic studies of transition metal diatomics have been an active research area in the past few decades.[77-81] The chemistry of transition metal monohalides is fascinating since transition metal monohalides are important model systems for understanding the role of the d electrons in chemical bonding.[82] The halides are important in areas ranging from industry[83], biological(catalysis)[84], organometallic chemistry[85,86],surface science[87] to astrophysics[88,89]. Because of high cosmic abundance of transition metal elements in stars, it is likely that some of these halide molecules may exist in significant amount in astrophysical sources.[80,81] In particular, diatomic metal halides have attracted significant attention in spectroscopy[40,47,49,53,77-84,87,90-107], photo physics and theoretical studies[82,92,106-116], because their electronic energy systems offer simple and essential models to understand the nature of transition metal containing molecules.[105]

Low resolution spectra of nickel monohalides have been reported intermittently since the 1930s,[77] but their assignments to various electronic transitions were often incomplete or incorrect as a result of complex perturbations in the observed spectra. The newly developing interest in small transition metal compounds is paving the way for the study of spectral properties of transition metal containing complexes.

Nickel monohalides (NiX; X=F, Cl, Br, I), have received much attention in the recent years, and the electronic structure of NiF [40,90-97,101,104,106,107] and NiCl[47,49,53,99,100,106,107] is now relatively well understood, while information on NiI and NiBr is still fragmented, although their ground states have been identified (Figure 3.1).[98,102,103] These molecules possess a number of low-lying electronic states, as depicted in Figure 3.2. The close proximity of the low lying electronic states in these species results in many perturbations which may complicate the spectra and make these species challenging from a theoretical viewpoint. Therefore, to understand the chemistry of these species, application of high resolution spectroscopic techniques, together with thorough theoretical investigation will enable improved understanding of the electronic structure of these species. The general similarity in five low-lying states in the monohalides series (see Figure 3.2) makes it reasonable to compare the general trends for the five lowest electronic states since they almost lie in the same energy level for the different species.

Ni   **X**
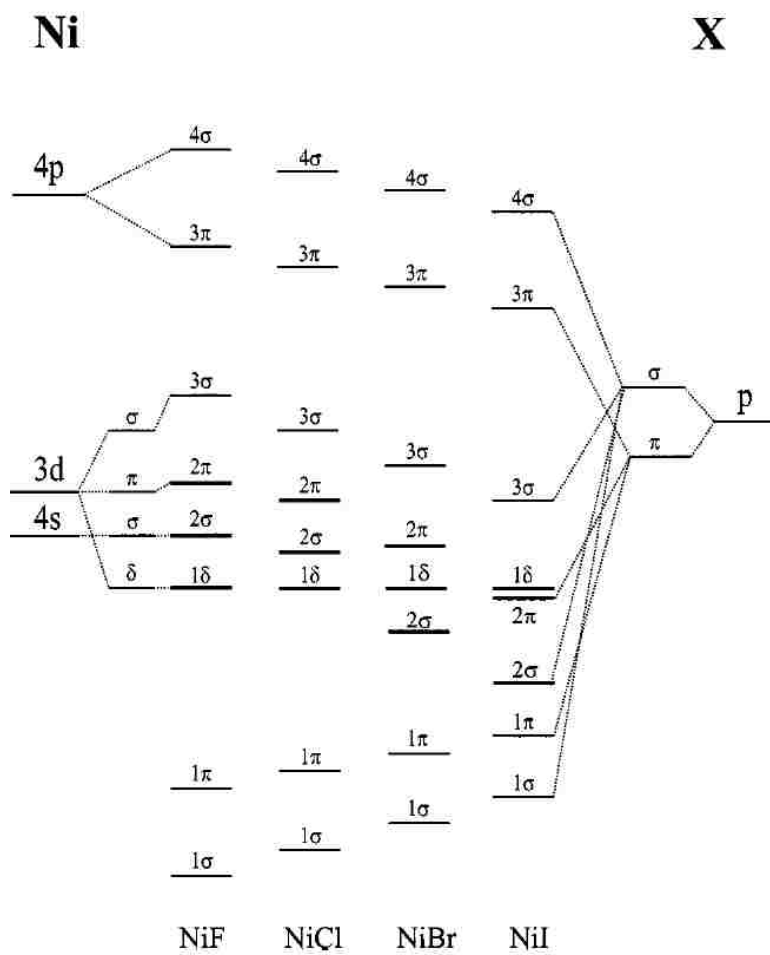
Figure 3.1 : Molecular orbital energy level diagram of nickel monohalides. Taken from Reference [102]
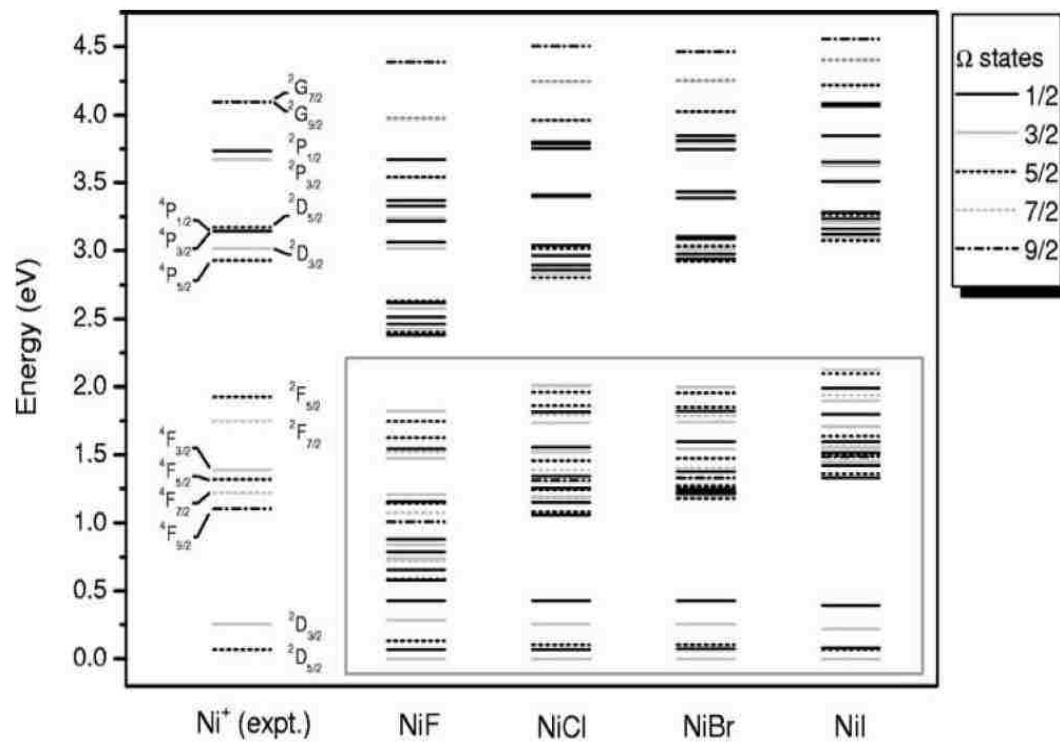
Figure 3.2 : Vertical excitation energies of nickel monohalides electronic states. Taken from Reference.[106]

3.2. Electronic structure of transition metal monohalides

The diatomic transition metal halides and hydrides MX (M=transition metal, X=H, F, Cl, Br, I) are highly ionic species represented as M^+X^-. Unpaired electrons mainly stay on the metal atom because of the closed shell structure of the X^- ion, and thus the resulting electronic states approximately maintain the character of the metallic ion M^+. It is well known that the nature of metal monohydride species MH often reflects nearly complete M^+ character. Such approximation constitutes a model which is a powerful method to analyze the remarkably complex and perturbed system.[117] Figure 3.3 shows the potential energy curves of the Λ-s states of various nickel monohalides, illustrating the density of predicted levels.
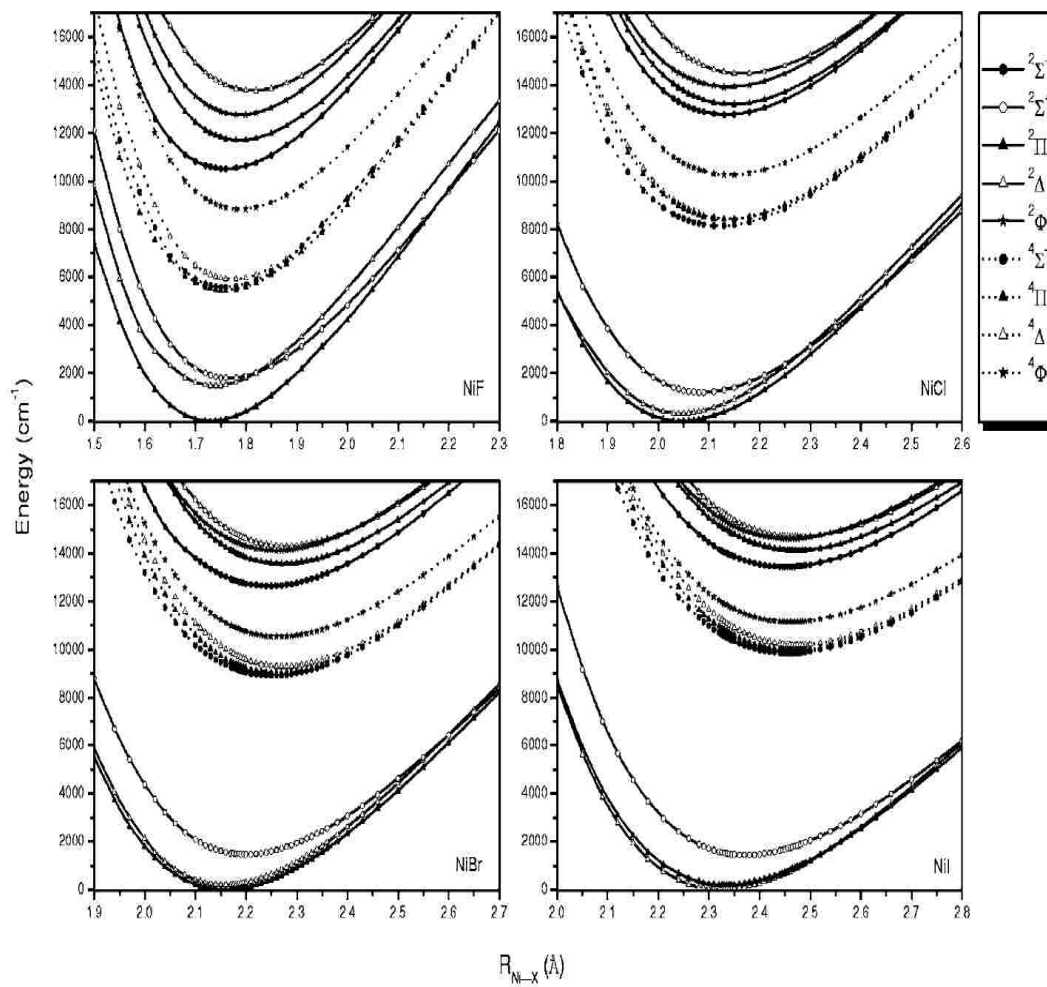
Figure 3.3 : Potential energy curves of the Λ-S states of NiX. Taken from Reference [106]

3.3. Notation and term symbols

The molecular term symbol is a shorthand expression of the group representation and angular momenta that characterize the state of a molecule; i.e., its electronic quantum state. It has the general form:

$$^{2S+1}\Lambda_{\Omega}^{\pm}$$

Where:

S is the total spin quantum number

Λ is the projection of the orbital angular momentum along the internuclear axis

Ω is the projection of the total angular momentum along the internuclear axis

$+/-$ is the reflection symmetry along an arbitrary plane containing the internuclear axis

For diatomic molecules the letters Σ, Π, Δ, Φ are used in the term symbol to represent = 0, 1, 2 and 3 respectively. For molecules with completely filled shells, the electron spin cancel therefore the quantum number S =0 (therefore the multiplicity (2S+1) equals 1, a singlet). When molecule has no completely filled shells, S=1 (therefore the multiplicity equals 2, a doublet).

For the purpose of simplifying the assignment of our spectrum, we use these notations and symbols. For example [13.9] $^2\Pi_{3/2}$ - $X^2\Delta_{5/2}$ represents a transition from the ground state $X^2\Delta_{5/2}$ to the excited state $^2\Pi_{3/2}$ with excitation energy of 13 900 cm^{-1}.

3.4. Literature survey on NiX

There has been progress on both theoretical and experimental aspects of the NiX species before we embarked on this study. Good knowledge of electronic structure of the ground and excited states of nickel monohalides has been obtained through years of hard work by many workers; however, for the latter two nickel monohalides, namely, NiBr and NiI, only limited spectroscopic information is available. The following section will summarize the work that has been done by other groups, and then later describe the details of the experimental work that we have done for these molecules.

3.4.1. NiI

In the nickel monohalides series, comparatively little is known about NiI. Tam and co-workers[102] observed and analyzed the laser induced fluorescence spectrum of NiI in the visible region between 588 and 720 nm. Molecular transition bands were generally easily identified because of the small rotational constant B value (0.065 cm^{-1}) and reasonably large vibrational separation (230 cm^{-1}). Two transition systems: [13.9] $^2\Pi_{3/2}$ - X$^2\Delta_{5/2}$ and [14.6] $^2\Delta_{5/2}$ - X$^2\Delta_{5/2}$ were observed and analyzed in their work.

The limited experimental work done on NiI by LIF[102,118] and microwave spectroscopy[105] has focused only on the two lowest energy electronic states. Indeed, the NiI ground state has been unambiguously identified as the $X^2\Delta_{5/2}$ only in the last decade, in the high resolution studies of Cheng and co-workers.[102,118] Bernath and co-workers[97,101] used Fourier transform (FT) spectroscopy to study many electronic transitions in the visible region above 600 nm and also in the near infrared region[101] from 9 500 to 13 000 cm^{-1}. However, no transitions were reported for a gap between 13 000 and 16 000 cm^{-1} as well as above 21 000 to 23 000 cm^{-1} (which was measured in our work).

3.4.2.   NiBr

The spectroscopy of NiBr has been investigated by several groups, most extensively by Leung and co-workers.[98,119] Band spectra attributed to NiBr molecule had earlier been studied by Mesnage in 1939[120] and later by Krishnamurty in 1952[121] using various discharge techniques. Reddy and Rao in 1960[122] recorded 62 emission bands in the violet region using heavy current and high frequency discharges. Four electronic states of NiBr have been studied using the technique of laser vaporization/reaction with supersonic cooling and laser induced fluorescence spectroscopy. High resolution LIF spectrum in the region 724 - 810 nm were recorded and analyzed.[98] Jianjun and co-workers also measured the spectrum of NiBr in the region between 604 - 666 nm.[123]

Recently, Leung and co-workers using laser vaporization/reaction free jet expansion and LIF identified and confirmed that $X^2\Pi_{3/2}$ state is the ground state and the next low lying state is $A^2\Delta_{5/2}$ state, and determined that the two low lying states are separated by only 37.25 cm^{-1} .[98]

3.4.3.   NiCl

In general, the energy levels of metal halides correlate with those of metal hydrides (MH). However the low-lying electronic energy levels of NiH appear to differ somewhat from those of the nickel monohalides. For NiH, the ground state is $^2\Delta$ similar to NiI while NiCl, NiBr and NiF have a $^2\Pi$ ground state.[49,53] A total of six electronic transitions of NiCl has been recorded by high –resolution Fourier transform spectroscopy.[49,53] A characteristic emission spectrum of NiCl was also recorded in the spectral region of 20 000 - 25 000 cm^{-1}.[49,53]

3.5. Outline of Chapter

In this chapter, we focus on the identification and characterization of the low lying electronic states ($X^2\Pi_{3/2}$, $A^2\Delta_{5/2}$, $X^2\Pi_{1/2}$, $A^2\Delta_{3/2}$ and $B^2\Sigma^+_{1/2}$) of NiI, NiCl and NiBr using laser induced fluorescence (LIF) and single vibronic level (SVL) emission spectroscopy. In this study we have obtained new LIF and SVL spectra of jet-cooled NiI, NiBr and NiCl in the visible region. New band systems of NiI[39] , NiBr[63] and NiCl[63] have been identified in the range 21 150 - 22 410 cm^{-1}. Assignments of the excited states have been made based upon rotational simulations using the PGOPHER program[124] and transitions observed in the emission spectra. Further, building upon the LIF and SVL emission studies, theoretical calculations were used to complement and compare with the experimental results. Results were also compared with previous work, including a study of the ground and excited states using high resolution Fourier transform(FT) and microwave spectroscopy.[105] The vibrational parameters are compared to the recent high level *ab initio* calculations by Zhou and Liu.[33] The data set derived in this chapter affords a detailed analysis of periodic trends in the nickel monohalide series.

3.5.1. Experimental details

NiI, NiBr and NiCl was produced using a pulsed discharge source, wherein Ni atoms sputtered from stainless steel electrodes (Type 303 stainless contains 8–10% Ni) reacted with an appropriate halogen-containing precursor seeded in ~3 bar Ar (Airgas). A rotational temperature in the range of 50 K was determined from preliminary fits of the fluorescence excitation spectra [124]. A variety of halogen-containing precursors, including CH_3I, CD_3I, $^{13}CD_3I$, CH_2Br_2, and C2Cl4 (Sigma-Aldrich, 99.5+ %) were employed in order to identify the species observed. Typically, discharge was initiated by a -1.3 kV pulse, with a width of 1000 μs, through a current limiting 80 kΩ ballast resistor. A pulse width of 200 μs was used initially, and was subsequently reduced to 50 μs to improve signal-to-noise. The timing of laser, nozzle and discharge firing was controlled by an 8-channel pulse/digital delay generator (Berkeley Nucleonics). SVL emission spectra were obtained using a 0.3 m spectrograph (Action SR303i with ISTAR CCD) in photon counting mode; the slit width was varied in the range 100-160 μm, with a narrower slit employed to improve spectral resolution. Spectra were integrated over 15,000 - 20,000 laser shots, and were calibrated using the output of a Fe: Ar hollow cathode lamp (Photron). The majority of the spectra recorded as part of the present study were collected using a 600 lines/mm grating. In some instances, it was necessary to employ an 1800 lines/mm grating in order to improve resolution. Bands in the emission spectra were fitted to a Gaussian line shape function, using Origin 7.5 software; previous studies have shown the validity of this approach.[102,118,125] The uncertainty in the derived band positions is ± 2 cm^{-1}.

3.6. Theoretical calculations

The low-lying electronic states of the nickel monohalides, i.e., NiI, NiBr, NiCl, and NiF, were investigated by Zou and Liu [106] using multireference second-order perturbation theory with relativistic effects taken into account. For the energetically lowest states, the potential energy curves and corresponding spectroscopic constants (vertical and adiabatic excitation energies, equilibrium bond lengths, vibrational frequencies, and rotational constants) were reported. The calculated results were in very good agreement with those of experimental data.[106] In particular, the ground state of NiI is shown to be different from those of NiF, NiCl, and NiBr, being in line with the recent experimental observation.[102] Multiconfigurational self-consistent field (MCSCF) is a method in quantum chemistry used to generate qualitatively correct reference states of molecules in cases where Hartree–Fock and density functional theory are not adequate. The calculation of electronic excited states is typically a multiconfiguratinal problem, and therefore it should preferably be treated with multiconfiguratinal methods such as CASSCF. To guarantee the required degeneracy of the relevant states, state-averaged complete active space self-consistent field (State- Averaged SA-CASSCF) calculations were performed by using the MOLCAS program package.[106] SA-CASSCF calculations, are methods in which one single set of molecular orbitals is used to compute all the states of a given spatial and spin symmetry. The obtained density matrix is the average for all states included, although each state will have its own set of optimized configuration interaction (CI) coefficients.

The use of a SA-CASSCF procedure has a great advantage. For example, all states in a SA-CASSCF calculation are orthogonal to each other, which is not necessarily true for state specific calculations.

Yang and co-workers also studied the potential-energy curves, spectroscopic terms, vibrational levels, and the spectroscopic constants of the ground and low-lying excited states of NiI by employing the complete active space self-consistent-field method with relativistic effective core potentials followed by multireference configuration-interaction calculations.[126]

3.7. SVL emission spectroscopy of low-lying states of NiI

In the case of the nickel iodide NiI radical, only limited knowledge had been available, until Tam *et al*.[102,127] observed the first high-resolution LIF spectrum of the two isotopomers ^{58}NiI and ^{60}NiI. Indeed, the ground state has been unambiguously identified only in the last decade, in the high resolution studies of Cheung and co-workers. [102,118] Assignment of the ground state in that work as $^2\Delta_{5/2}$ is consistent with NiH, but differs from the lighter monohalides analogues, which feature a $^2\Pi_{3/2}$ ground state.

In this present chapter, three new band systems of NiI have been identified in the range 21 150 – 22 410 cm^{-1}. Assignments of the symmetries of the excited states have been made based upon rotational simulations and transitions observed in the emission spectra.

However, the detailed rotational and vibrational analysis of these bands is discussed later. Here we focus on the use of these new band systems to probe the vibrational structure of the five low-lying ($T_e < 2200$ cm^{-1}) electronic states of NiI with SVL emission spectroscopy. Three of these low-lying states are observed here for the first time, and the harmonic frequencies for all five low-lying states were derived from SVL emission spectra and are compared to recent *ab initio* values[107].

3.7.1.   Spectral Analysis: Single vibronic level emission spectra for NiI

Three new band systems of NiI have been observed in the range 21 150 – 22 410 cm^{-1}, originating from the Ni$^+$ ($3d^84s^1$) configuration [107]. Excited state symmetries have been assigned based on rotational simulations using PGOPHER program [124] and analysis of the single vibronic level emission spectra. In the following discussion, these states will be identified using the nomenclature adopted by Tam et al.[102,118] with T_0 values in thousands wavenumbers given in square brackets: for example [21.1]$^2\Pi_{3/2}$ representing a doublet Π state with excitation energy of 21 100 cm^{-1}. A detailed rotational and vibrational analysis of these band systems will be discussed later.

SVL emission spectra were obtained from several bands in each of the three progressions; a total of 10 emission spectra were collected, each containing numerous bands extending up to 3746 cm^{-1} above the X$^2\Delta_{5/2}$ state origin.

Examples are shown in Figure 3.4, which displays SVL emission spectra collected via the

$v = 0$ level of the $[21.1]^2\Pi_{3/2}$ and $[21.3]^2\Delta_{5/2}$ bands. It is possible to identify five distinct

vibrational progressions. In addition to the $X^2\Delta_{5/2}$ and $A^2\Pi_{3/2}$ states characterized in

previous work, [102,105,118] three additional electronic states have been identified. Based on

the theoretical work of Zou and Liu [107], these are assigned as the $A^2\Pi_{1/2}$, $X^2\Delta_{3/2}$, and

$B^2\Sigma^+_{1/2}$ states. Comparison of SVL spectra recorded via different vibrational levels in the

excited states show consistent sets of levels with an intensity pattern reflecting the nodal

structure of the vibrational wavefunction.
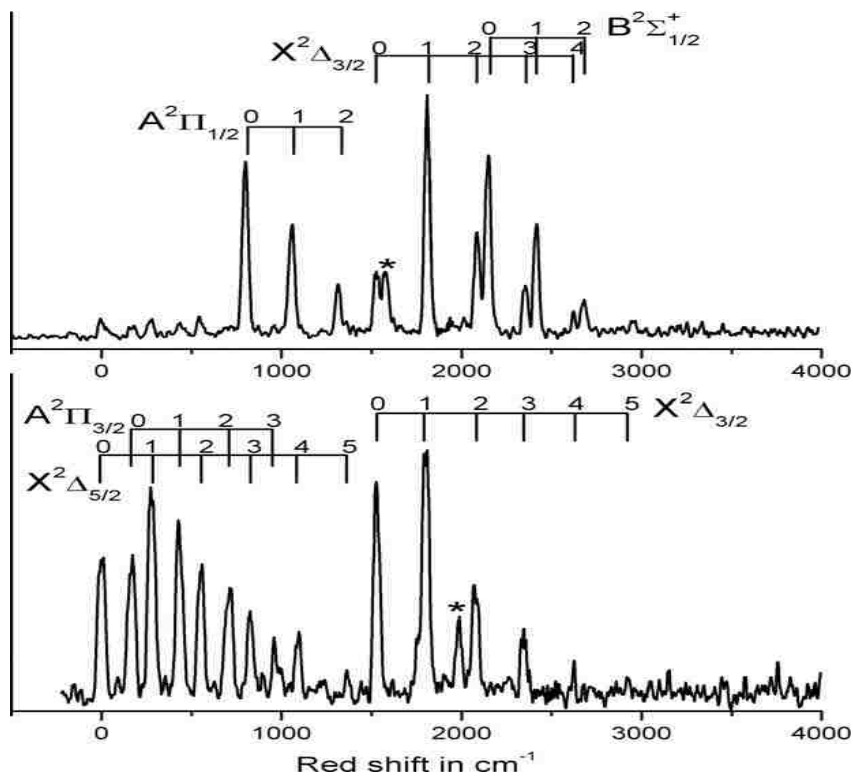
Figure 3.4 : SVL spectra of NiI recorded via (0-0) of the $[21.3]^2\Delta_{5/2}$ (lower trace) and (0-0) of the $[21.1]^2\Pi_{3/2}$ (upper trace) excited state origin bands; the x-axis labels the shift in cm^{-1} from the excitation line. Although not labeled, the $X^2\Delta_{5/2}$ and $A^2\Pi_{3/2}$ states appear weakly in the $[21.1]^2\Pi_{3/2}$ spectrum. Features labeled with an asterisk arise from the discharge background.
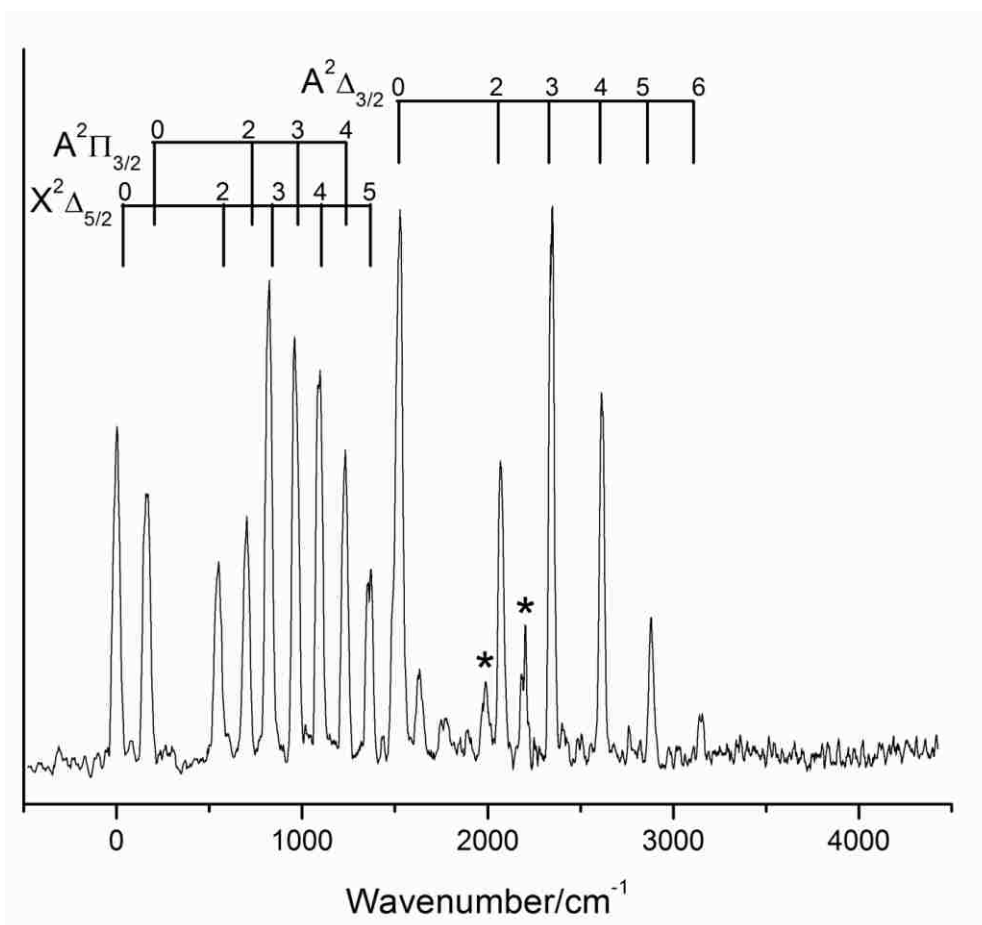
Figure 3.5: SVL spectra of NiI recorded via (0-2) of the $[21.6]^2\Pi_{3/2}$ excited state bands; the x-axis labels the shift in cm^{-1} from the excitation line. Features labeled with an asterisk arise from the discharge background.

The calibrated emission spectra peak energies have been fit to a Dunham expansion in order to derive term energies and vibrational constants for the five electronic states, and these are given in Table 3.1. Included also in Table 3.1 are the previous experimental[105,118] and theoretical[107] ω_e and T_e values. Note that previous experiments obtained vibrational information through the measurement of hot-band spectra, and therefore only anharmonic frequencies were reported. The experimental peak energies, their assignments and their deviation from the energies predicted by the Dunham expansion are provided in Table 3.2. As expected, the theoretical values overestimate the experimentally derived harmonic frequencies; however, the trends in the two sets are in good agreement. This can be seen in Figure 3.7, where the experimental values are plotted with the *ab initio* values, which were scaled so that the $X^2\Delta_{5/2}$ frequency is coincident with the experimental value. Experimental T_0 values are also in good agreement with the calculated T_e values, with the exception of the $X^2\Delta_{5/2}$ state, which appears ~200 cm^{-1} higher than predicted.

The theoretical predictions of NiI Ω states up to ~16,000 cm^{-1} predict a gradual if not monotonic decrease in vibrational frequency with increasing energy[107]. Following with this trend, our preliminary analysis indicates that the harmonic vibrational frequencies of the new states identified in this work in the region 21 000 – 22 000 cm^{-1} are on the order of 220 cm^{-1}. More analysis on the excited state in this region will be discussed later. We also note that the $X^2\Delta_{5/2}$ and $A^2\Pi_{3/2}$ states are observed in emission spectra recorded via the origin level of all three excited states observed in the present study, but with considerable variation in intensity.

In SVL spectra recorded via the two $^2\Pi_{3/2}$ states, the $X^2\Delta_{5/2}$ and $A^2\Pi_{3/2}$ progressions are very weak, as can be seen in the upper trace of Figure 3.4. This is in contrast to the SVL spectrum recorded via the origin of the $[21.3]^2\Delta_{5/2}$ state (also shown in Figure 3.4) where the intensity of these two bands is considerably larger. A change in the Frank Condon profile can be seen when different bands are excited. For example compare Figure 3.4 and Figure 3.5, which show a shift in Frank Condon profile observed from exciting $[21.6]^2\Pi_{3/2}$ band as compared to $[21.3]^2\Delta_{5/2}$. From the FC principle we can derive FC factors, which are defined as the squared overlap integral of the two wavefunctions for the excited and ground state. The FC factor determines how the intensity is distributed among the vibrational bands. However no further spectra intensity modeling was performed for this work.

3.7.2. Perturbations

Irregular behavior is an excellent operational definition of perturbation phenomena.[125] The study of perturbations involves going beyond the Born-Oppenheimer approximation. One starts with a zero-order model H^0 in which each electronic state is associated with a potential energy curve, an electronic eigenfunction which depends on internuclear distance and a set of rotational-vibrational eigenvalues and eigenfunctions.[125]

There are different types of perturbations, for example (a) local perturbations between electronic states of different or same symmetry, (b) perturbations involving interactions between components of the same vibrational quantum number of one or several electronic states and (c) interaction between rotational levels and vibrational levels of different electronic states.[125]

For our purpose we are going to concentrate on interactions between vibrational levels between electronic states of different symmetry, this is the interaction between the spin and the orbital angular momenta of the electron (spin-orbit interaction). These interactions remove degeneracy of the levels of an electronic state. The mixing of the states provides a mechanism for observation of forbidden transitions and homogeneous ($\Delta\Omega = 0$) perturbations[125] (which are the ones observed in our study).

Table 3.1 : Vibrational constants and term energies (in cm^{-1}) of the five low-lying electronic states of NiI observed in the present work.

	$X\,^2\Delta_{5/2}$	$A\,^2\Pi_{3/2}$	$A\,^2\Pi_{1/2}$	$X\,^2\Delta_{3/2}$	$B\,^2\Sigma^+_{1/2}$	Source
T$_0$	0	162.7 (1.2)[a]	787.8 (2.9)	1529.8 (1.8)	2140.2 (2.2)	This work
		164				Ref. [102]
		139	812	1332	2210	Ref. [107]
ω_e	278.5 (0.3)	273.2 (0.7)	260.0 (5.1)	277.5 (1.4)	268.0 (2.2)	This work
	276[b]	271[b]				Ref. [118]
	276.67[b]					Ref. [102]
	290	283	274	287	281	Ref. [107]
x_e	-0.74 (0.03)	-0.85 (0.06)	-0.45 (1.25)	-0.89 (0.17)	0.02 (0.36)	This work

[a] One standard error given in parenthesis; [b] anharmonic values.

3.7.3. Perturbations involving the low-lying electronic states of NiI

An examination of the residuals between the observed energies and those predicted by the Dunham expansion has identified the presence of homogenous perturbations in the low-lying electronic states; this can be seen in Figure 3.6. The ground $X^2\Delta_{5/2}$ state is apparently free of perturbations, at least up to the v = 8 level, as all of the vibrational states can be fit to the Dunham expansion within experimental error. The first obvious perturbation appears for the v = 5 and v = 6 levels of the $A^2\Pi_{3/2}$ state at 1497.52 and 1773.53 cm^{-1}, which are shifted in energy by -5.3 and 7.8 cm^{-1}, respectively (these are in Table 3.2).

Since these are interactions between the spin and orbital angular momenta (spin-orbit interaction), under the $\Delta\Omega = 0$ selection rule[125], the only candidate for the perturbing level is the v = 0 level of $X^2\Delta_{3/2}$. The most important objective of deperturbation are a perfect fit of the observed spectral lines, confirmation of line assignments, proof of the mechanism of the perturbation and determination of perturbation parameters.[125] The quality of the fit establishes the credibility of the model and reduces the possibility of misassigned lines. Deperturbation analysis using analytical expressions appropriate for a three level system[125] (perturbation involving three interacting levels) yield the following estimates for the matrix elements:

$$\langle \tilde{A}^2 \Pi_{3/2}; v = 5 | \hat{H}' | \tilde{X}^2 \Delta_{3/2}; v = 0 \rangle = 12 \; cm^{-1}; \langle \tilde{A}^2 \Pi_{3/2}; v = 6 | \hat{H}' | \tilde{X}^2 \Delta_{3/2}; v = 0 \rangle = 43 cm^{-1}$$

At higher energies, another obvious perturbation involves the $B^2\Sigma^+_{1/2}$ $v = 1$ and $v = 2$ levels at 2415.76 and 2665.03 cm^{-1}, shifted by 7.6 and -11.1 cm^{-1}, respectively (highlighted in Table 3.2). Again, the magnitude of the shift is small, suggesting a weak interaction. Under the $\Delta\Omega = 0$ selection rule[125], the perturbing states must be vibrational levels of the $A^2\Pi_{1/2}$ state. For example, the $v = 6$ level of $A^2\Pi_{1/2}$ is predicted from the Dunham parameters to lie at 2329 cm^{-1}, and likely interacts with the $B^2\Sigma^+_{1/2}$ $v = 1$ level. As a consequence of this interaction, the former would be expected to appear in the emission spectra; however, we did not observe this level within our signal to noise. The level perturbing $v=2$ of $B^2\Sigma^+_{1/2}$ is likely to be a higher lying level of the $A^2\Pi_{1/2}$ state, pushing it down by -11cm^{-1}.

Note that the vibrational progression observed in the $A^2\Pi_{1/2}$ state (up to $v = 3$) is significantly shorter than for any of the other four levels. As evident in Figure 3.6 , the residuals between experimental and predicted peak positions become larger to higher energy, indicating significant perturbations in the level structure. Given the presence of five electronic states within roughly 2 200 cm^{-1} of the ground state, this is not surprising.

Generally the theoretical predictions are in good agreement with experiment, as shown in Figure 3.7.
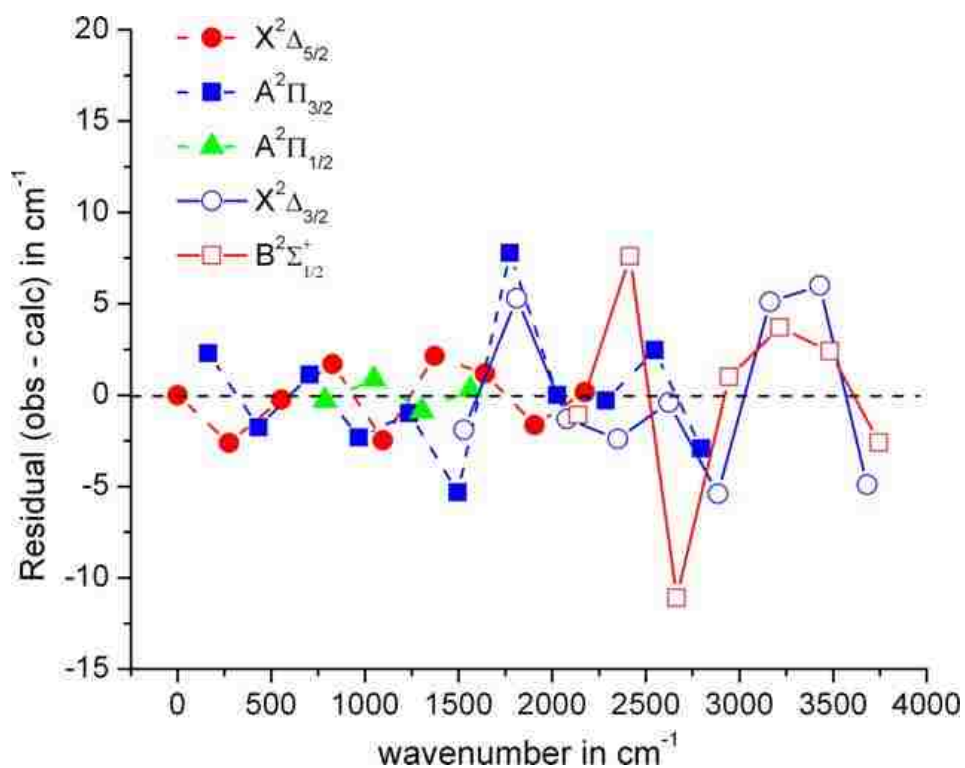
Figure 3.6 : Residuals (Obs – Calc) of the vibrational levels observed in this work for the five lowest lying electronic states of NiI. The x-axis labels the energy in cm^{-1} above the vibrationless level of the ground state. Calculated values were determined from Dunham expansion fits, as described in the text.
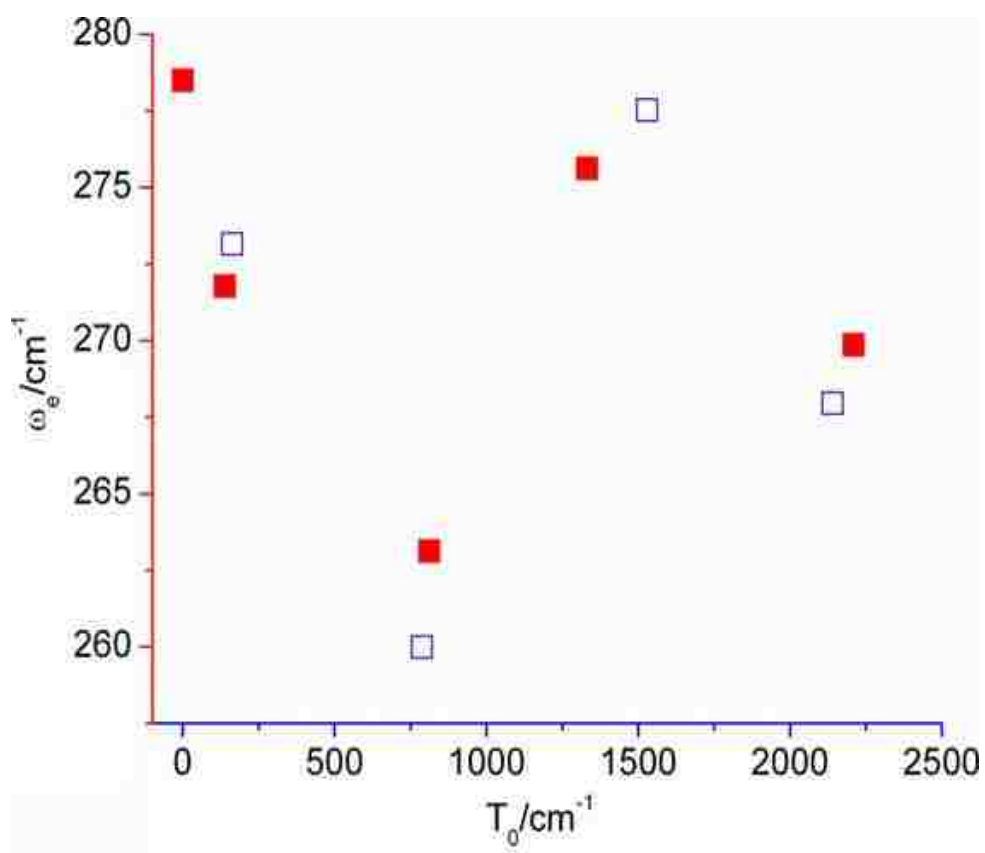
Figure 3.7 : A comparison of experimentally-derived we and To values for five low-lying electronic states of NiI (blue open squares) with theoretical vibrational frequencies (scaled, red squares) and Te values from ref [39].

Table 3.2 : Term energies and assignments of the low-lying electronic states of NiI observed in this work. The deviations (Obs –Cal) between experimental energies and those predicted by a fit of the experimental values to the Dunham expansion are also shown.

State	V	Energy/ Cm^{-1} Calc	Energy /Cm^{-1} Obs	Obs-Cal
X$^2\Delta_{5/2}$	0	0	0	0
	1	277	274	-2
	2	553	552	0
	3	826	828	2
	4	1099	1096	-2
	5	1370	1372	2
	6	1639	1641	1
	7	1908	1906	-1
	8	2174	2175	0
A$^2\Pi_{3/2}$	0	162	164	2
	1	434	432	-1
	2	703	705	1
	3	971	969	-2
	4	1238	1237	-1
	5	**1502**	**1497**	**-5**
	6	**1765**	**1773**	**7**
	7	2026	2026	0
	8	2286	2286	0
	9	2544	2546	2
	10	2800	2797	-2
A$^2\Pi_{1/2}$	0	787	787	0
	1	1046	1047	1
	2	1305	1304	-1
	3	1562	1562	0
X$^2\Delta_{3/2}$	0	1529	1527	-2
	1	1805	1810	5
	2	2079	2078	-1
	3	2351	2349	-2
	4	2622	2621	0
	5	2890	2885	-5
	6	3157	3162	5
	7	3422	3428	6
	8	3686	3681	-5

Table 3.2:

Table 3.2 Continued		Energy/ Cm^{-1}	Energy /Cm^{-1}	
State	v	Calc	Obs	Obs-cal
$B^2\Sigma^+_{1/2}$	0	2140	2139	-1
	1	**2408**	**2415**	**7**
	2	**2676**	**2665**	**-11**
	3	2944	2945	1
	4	3212	3216	3
	5	3480	3482	2
	6	3748	3745	-2

3.7.4. Summary

Five low-lying electronic states of NiI have been observed and vibrationally characterized (three for the first time) using single vibronic level emission spectroscopy, following the first observation of three excited state band systems in the range 21 150 – 22 410 cm^{-1}. The derived harmonic frequencies and term energies of the five low-lying electronic states are in good agreement with the theoretical values of Zou and Liu [107] and the trend in the calculated ω_e values is replicated extremely well by the experimental values determined in the present work. The agreement can also be shown in Figure 3.7. A number of homogeneous perturbations involving electronic states with different symmetry have been identified, which arise from interactions between vibrational levels of the $A^2\Pi_{3/2}$ and $X^2\Delta_{3/2}$ states and $A^2\Pi_{1/2}$ and $B^2\Sigma^+_{1/2}$ states. There are no other low-lying states with $\Omega = 5/2$, and the ground $X^2\Delta_{5/2}$ state remains unperturbed up to the highest energies measured in this work.

3.8. SVL emission spectroscopy of the low-lying electronic states of NiBr

Recently Leung *et al.*[98], using laser vaporization/free jet expansion and laser-induced fluorescence to probe the spectroscopy of NiBr in the 12 345 to 13 812 cm^{-1} region, identified the ground state as the X$^2\Pi_{3/2}$. In that work, the A$^2\Delta_{5/2}$ state was found to be just 37.25 cm^{-1} above X$^2\Pi_{3/2}$. Assignment of the NiBr ground state was also confirmed in the detailed theoretical study of Zou and Liu. [107]

In this chapter we report five low-lying electronic states of NiBr observed using single vibronic level (SVL) emission spectroscopy, three of which were experimentally observed for the first time. Harmonic frequencies of all five states have been derived from the SVL spectra and were compared to *ab initio* values.[107] These states were assigned as X$^2\Pi_{3/2}$, A$^2\Delta_{5/2}$, X$^2\Pi_{1/2}$, A$^2\Delta_{3/2}$ and B$^2\Sigma^+{}_{1/2}$ based on the theoretical work of Zou and Liu.[107] Vibrational constants have been derived and were found to be in good agreement with theoretical values. In particular, the trend in the theoretical harmonic frequencies of Zou and Liu [107] is reproduced successfully in the experimental values.

The emission spectra of NiBr are not affected to the same extent as for NiI[39] by interactions between vibronic levels, however one possible perturbation observed herein is tentatively attributed to a three level interaction involving X$^2\Pi_{1/2}$ v = 9, and B$^2\Sigma^+{}_{1/2}$ v = 4 and v = 5, within the $\Delta\Omega = 0$ selection rule. A detailed rotational and vibrational analysis of the excitation bands, together with those of the other Nickel monohalides, will be reported later in this chapter. In this section, we focus on examination of the low-lying NiBr electronic states using SVL emission spectra from these upper states.

3.8.1. Spectral Analysis: Single Vibronic Level emission spectra for NiBr

The electronic configurations which give rise to the five low-lying NiBr electronic states observed in the SVL spectra are $(2s)^2(1d)^4(2p)^3$ ($X^2\Pi_{3/2}$ and $X^2\Pi_{1/2}$), $(2s)^2(1d)^3(2p)^4$ ($A^2\Delta_{5/2}$ and $A^2\Delta_{3/2}$) and $(2s)^1(1d)^4(2p)^4$ $B^2\Sigma^+_{1/2}$. The 1d and 2p MOs have predominantly Ni^+ character.

Four new bands systems of NiBr have been observed in the region 21 608 - 22 727 cm^{-1}, which have been assigned by analogy to the NiI system and following rotational simulations of the excited state bands using PGOPHER[124] and from an analysis of the SVL spectra. Three of these are analogous to those observed in our recent study of NiI,[39] being of $[21.6]^2\Pi_{3/2}$, $[21.8]^2\Delta_{5/2}$ and $[22.4]^2\Pi_{3/2}$ symmetry.[102,118] The fourth state is assigned as $[22.3]^2\Sigma^+_{1/2}$. Single vibronic level emission spectra have been recorded via a total of twenty four excited state vibronic cold and hotbands (the latter originate from the vibration-less origin of $A^2\Delta_{5/2}$). Only the $X^2\Pi_{3/2}$ and $A^2\Delta_{5/2}$ states have been previously observed. The emission spectrum obtained with our low resolution (600 l/mm) grating and following excitation of the v = 1 level of $[21.8]^2\Delta_{5/2}$ is shown in the lower trace of Figure 3.8, were emission to the $X^2\Pi_{3/2}$, $A^2\Delta_{5/2}$ and $A^2\Delta_{3/2}$ states can be identified. The absence of the $X^2\Pi_{1/2}$ and $B^2\Sigma^+_{1/2}$ states is consistent with the assigned excited state symmetry of $^2\Delta_{5/2}$, given the relevant selection rules $\Delta\Lambda = 0, \pm 1$ and $\Delta\Omega = 0, \pm 1$.[128] We note that here Λ is only an approximately good quantum number, and our resolution is insufficient to separate spectra from the various $^{58,60}Ni^{79,81}Br$ isotopomers.

Due to the very small splitting of the $X^2\Pi_{3/2}$ and $A^2\Delta_{5/2}$ states, resolving these features in the emission spectrum required the use of a higher resolution (1800 l/mm) grating. The close-proximity of the $X^2\Pi_{3/2}$ and $A^2\Delta_{5/2}$ states, which are separated by just 43(1) cm^{-1}, results in an overlap of the vibrational progressions in these states in the emission spectra. This overlap is particularly severe for the $v = 0$ level of each of these states, which makes deriving accurate peak energies more challenging. This can be seen in Figure 3.8, which shows the SVL spectrum resulting from excitation of the $[21.8]^2\Delta_{5/2}$ $v = 1$ excited state. The lower trace was recorded using a lower resolution spectrograph grating (600 l/mm) and the $X^2\Pi_{3/2}$ and $A^2\Delta_{5/2}$ progressions are clearly overlapped. The use of a higher resolution grating (1800 lines/mm) improves the resolution significantly, as can be seen in the upper trace of Figure 3.8. Higher resolution is essential in order to identify the $B^2\Sigma^+_{1/2}$ state, as the $B^2\Sigma^+_{1/2}$ state origin overlaps severely with the $v = 1$ level of the $A^2\Delta_{3/2}$ state and as a result of the similar vibrational frequency in these states, this overlap affects all subsequent vibronic bands.

Figure 3.9, shows the emission spectrum recorded via the $[21.6]^2\Pi_{3/2}$ $v = 1$ level. The presence of all five low-lying electronic states in the emission spectrum recorded via the $[21.6]^2\Pi_{3/2}$ $v = 1$ level further confirms the assignment of the $^2\Pi_{3/2}$ in the upper state; the $^2\Pi_{3/2}$ configuration is the only state from which transitions to all five states is allowed, given the relevant selection rules $\Delta\Lambda = 0, \pm1$ and $\Delta\Omega = 0, \pm1$.[128]
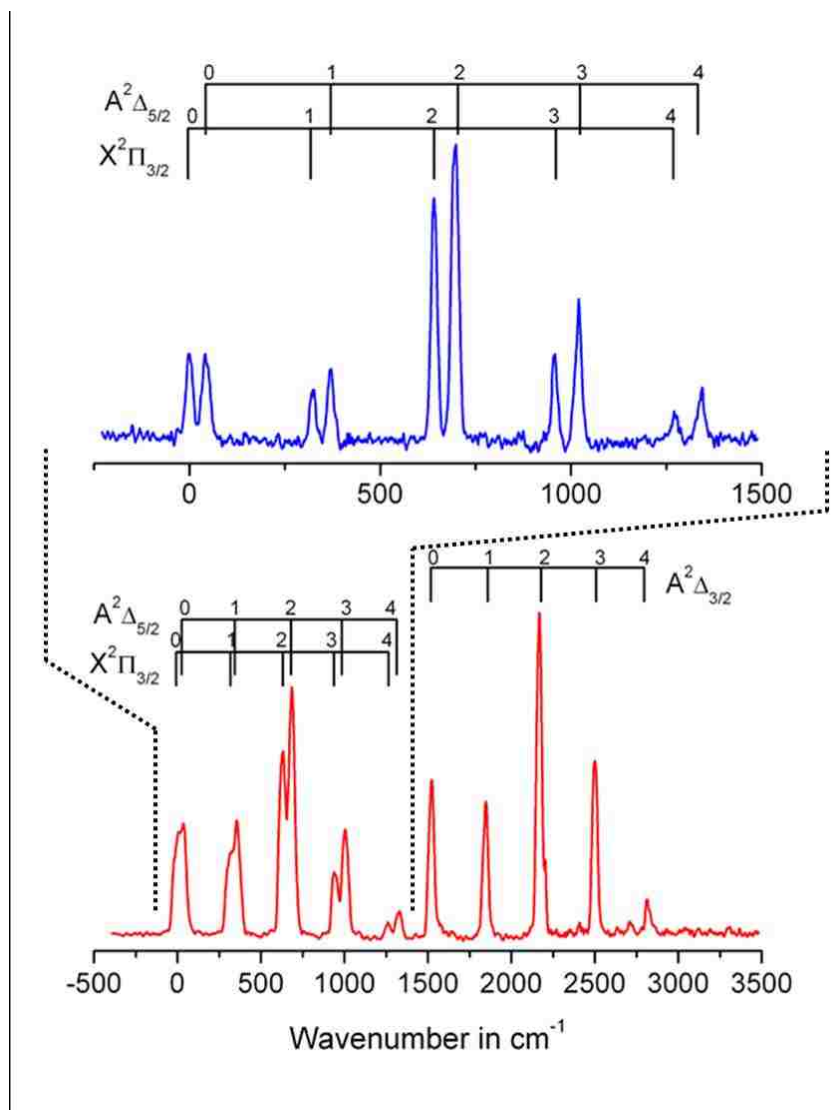
Figure 3.8 : SVL spectrum of NiBr recorded via (0-1) of the $[21.8]^2\Delta_{5/2}$ using a 600 lines/mm grating (lower trace) and an 1800 lines/mm grating (upper trace). Vibronic assignments are indicated.
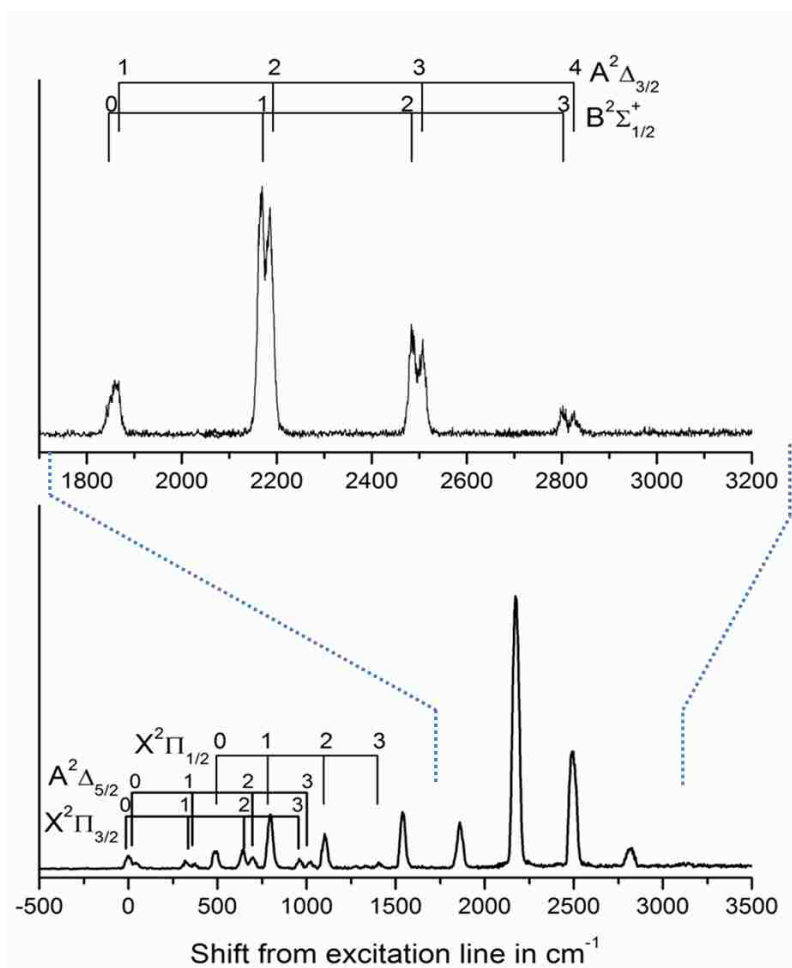
Figure 3.9: SVL spectrum of NiBr recorded via the $[21.6]^2\Pi_{3/2}$ v = 1 level using a 600 lines/mm grating (lower trace) and an 1800 lines/mm grating (upper trace). All five low-lying electronic states are observed.

The calibrated emission spectra peak energies were fit to a (Dunham expansion)[129] to derive term energies, harmonic frequencies, and anharmonicity constants. Note that the previous high resolution studies of Cheung and co-workers succeeded in measuring with high precision the term energy of the $A^2\Delta_{5/2}$ state; however, in that work only transitions from the v=0 level of this state could be identified.[130] Our derived parameters (term energies, harmonic frequencies and anharmonic constants) from the Dunham fit, together with assignments and associated uncertainties, are listed in Table 3.3. Included also in Table 3.3 are previous experimental[98] and theoretical[107] ω_e and T_e values; note that the previous ω_e values represent estimates derived from microwave data. Our experimental T_0 values are in reasonable agreement with the calculated T_e values, with the exception of the $B^2\Sigma^+_{1/2}$ state, which is ~370 cm^{-1} lower than predicted. As expected, the (unscaled) theoretical harmonic frequencies slightly overestimate the experimentally derived values, but the trend in the experimental frequencies is in good agreement with theoretical predictions. The estimated uncertainty of ± 2 cm^{-1} was derived by consideration of the fit uncertainties and error propagation.

An examination of the deviation between the experimentally derived peak energies and the values predicted by the Dunham expansion can reveal the presence of perturbations caused by interactions between vibronic levels. However, the fit residuals (Table 3.4) for all bands observed in the SVL spectra lie within our experimental error of ± 2 cm^{-1}, and no obvious vibronic perturbations were thus identified. This contrasts with our previous study of NiI,[131] where numerous perturbations were observed, due to the larger spin-orbit coupling in that system.

Table 3.3 Vibrational constants and term energies (in cm^{-1}) of the five low-lying electronic states of NiBr observed in the present work.

	$X^2\Pi_{3/2}$	$A^2\Delta_{5/2}$	$X^2\Pi_{1/2}$	$A^2\Delta_{3/2}$	$B^2\Sigma^+_{1/2}$	Source
T_0	0	43.25(1.24)[a]	488.92(1.20)	1537.74(1.75)	1843.08(1.66)	This work
		37[b]				Ref [103]
		165	583	1453	2214	Ref [107]
ω_e	320.39(0.52)	326.87(1.21)	307.04(0.82)	326.91(1.06)	324.58(1.35)	This work
	331	317				Ref [103]
	336	345	328	344	335	Ref [107]
x_e	-0.77(0.09)	-0.81(0.18)	-0.95(0.10)	-0.93(0.13)	-1.26(0.13)	This work

[a] One standard error given in parenthesis; [b] anharmonic values.

3.8.2.   Perturbations involving the low-lying electronic states for NiBr

An examination of the deviation between the experimentally derived peak energies and the values predicted can reveal the presence of perturbations caused by interactions between vibronic levels. The majority of bands observed in the SVL spectra can be fit within experimental error of ± 2 cm^{-1}. This can be seen in Figure 3.10, where the deviation between observed and predicted peak energies is shown for each of the five electronic states observed herein.

The two low energy states $X^2\Pi_{3/2}$ and $A^2\Delta_{5/2}$ are free of perturbations, at least up to $v = 6$ and $v = 7$, the highest energy bands observed in the present study. The first deviation which exceeds experimental error arises for $X^2\Pi_{1/2}$ $v = 3$ and $v = 4$ (at 1396 cm^{-1} and 1700 cm^{-1}), which are shifted by -2.6 cm^{-1} and 2.7 cm^{-1} respectively from their predicted energies. However, under the $\Delta\Omega = 0$ selection rule (as described for NiI in chapter 3), there are no suitable candidates for the source of this perturbation. The $B^2\Sigma^+_{1/2}$ state origin is located at 1845 cm^{-1} and is therefore too high in energy to interact with either of the $X^2\Pi_{1/2}$ state levels. In this instance, these deviations are most likely attributable to experimental error. A potential perturbation arises for $B^2\Sigma^+_{1/2}$ $v = 4$ and $v = 5$ at 3111 cm^{-1} and 3428 cm^{-1}, which are shifted by -3.1 cm^{-1} and 2.7 cm^{-1} respectively from their predicted energies. Under the $\Delta\Omega = 0$ selection rule[125] an interaction with $X^2\Pi_{1/2}$ $v = 9$, which is predicted to lie at 3167cm^{-1}, is possible.

As a result of the three-level interaction, $B^2\Sigma^+_{1/2}$ v = 4 is shifted down in energy and v = 5 is shifted up. Given that the shifts in the $B^2\Sigma^+_{1/2}$ state levels are only just in excess of experimental error, the identification of a perturbation is only tentative.

In general, interactions between electronic states with identical Ω (if present) are weak in NiBr. This is due to the weakening of the spin-orbit interaction as we move from (Iodine) to (Bromine) in the periodic table.

Figure 3.10: Residuals (Obs – Calc) of the vibrational levels observed in this work for the five low-lying electronic states of NiBr. The x-axis labels the energy in cm^{-1} above the vibrationless level of the ground state. Calculated values were determined from fitting experimental energies to the Dunham expansion.

Table 3.4 : Term energies and assignments of the low-lying electronic states of NiBr observed in this work. The deviations (Obs –Cal) between experimental energies and those predicted by a fit of the experimental values to the Dunham expansion are also shown.

State	V	Energy/ cm^{-1} Cal	Energy /cm^{-1} Obs	Obs-Cal
$X^2\Pi_{3/2}$	0	0	0	0
	1	318	320	2
	2	636	638	2
	3	951	950	-1
	4	1266	1264	-2
	5	1578	1579	0
	6	1890	1890	0
$A^2\Delta_{5/2}$	0	43	42	-1
	1	368	368	0
	2	692	694	2
	3	1014	1014	0
	4	1334	1332	-2
	5	1653	1651	-2
	6	1970	1971	1
$X^2\Pi_{1/2}$	0	488	489	1
	1	794	793	-1
	2	1097	1096	-1
	3	1398	1396	-2
	4	1698	1700	2
	5	1995	1997	2
	6	2291	2289	-2
$A^2\Delta_{3/2}$	0	1537	1539	2
	1	1862	1860	-2
	2	2185	2183	-2
	3	2506	2507	1
	4	2824	2827	2
	5	3141	3140	-1
	6	3456	3456	0
	7	3768	3768	
$B^2\Sigma^+_{1/2}$	0	1843	1845	2
	1	2164	2165	1
	2	2484	2483	-1
	3	2800	2800	0
	4	3114	3111	-3
	5	3425	3427	2
	6	3733	3734	1
	7	4039	4037	-2

3.8.3.   Summary

We report LIF and SVL emission spectra of NiBr and NiCl that probe the term energies and vibrational structure of the five low-lying electronic states ($X^2\Pi_{3/2}$, $A^2\Delta_{5/2}$, $X^2\Pi_{1/2}$, $A^2\Delta_{3/2}$ and $B^2\Sigma^+_{1/2}$) that arise from the $3d^9$ configuration of Ni^+. Single vibronic level emission spectra have been recorded following the excitation of vibronic bands in four new bands systems of NiBr. Five low-lying electronic states have been observed; high resolution SVL spectra were recorded in order to resolve members of the $X^2\Pi_{3/2}$ and $A^2\Delta_{5/2}$ and, in particular, the $A^2\Delta_{3/2}$ and $B^2\Sigma^+_{1/2}$ states. The derived harmonic frequencies and term energies are in good agreement with the theoretical values of Zou and Liu [107] and the trend in the theoretical values is reproduced successfully in the experimental values. In contrast to NiI, the spectra of NiBr show few vibronic perturbations, reflecting the smaller spin-orbit coupling in this system. The only perturbation identified herein has been tentatively attributed to a three level interaction involving $X^2\Pi_{1/2}$ v = 9, $B^2\Sigma^+_{1/2}$ v = 4 and $B^2\Sigma^+_{1/2}$ v = 5, via the $\Delta\Omega = 0$ selection rule.

3.9. SVL emission spectroscopy of the low-lying electronic states of NiCl

Previous work by Krouti *et al* [49,53] did not fully investigate the vibrational frequencies for NiCl. Complete analysis of the NiCl constants will help us study the periodic trends of the nickel monohalides series as NiI and NiBr had been previously determined and discussed previously .The overall trend analysis of the nickel monohalides series will be discussed in the next chapter.

3.9.1.   Spectral Analysis for NiCl

For NiCl, all five low-lying states have previously been observed, and the term energies have been determined with reasonable precision.[132-134] However, the vibrational data for these states is not complete, and therefore we conducted similar SVL emission studies on this molecule in order to examine periodic trends among the Nickel monohalides. The SVL emission spectra were collected through three band systems previously identified by Bernath and co-workers using LIF and Fourier-transform emission spectroscopy: $[21.6]\Omega=3/2$, $[21.9]^2\Delta_{5/2}$, and $[22.3]^2\Delta_{3/2}$.[132,134]

In our group, NiCl band systems have been observed in the region 21 621 - 23 182 cm^{-1}. Rotational simulations using the PGOPHER program were done in the same way as for NiI and NiBr to identify the excited state band symmetry.

A discussion of the excitation spectrum analysis and simulations is left to a later section. The band systems observed for NiCl were analogous to those observed in the study of NiI[39] and NiBr. Emission spectra were obtained from the several observed bands in each of the progressions. SVL emission spectra were recorded via a total of sixteen bands in these band systems. The emission spectra were collected; each contained bands extending up to 4169 cm^{-1} above the $X^2\Pi_{3/2}$ ground state origin. An example SVL emission spectrum obtained following excitation of the v=2 level of $[22.7]^2\Pi_{3/2}$ and the v=3 level of $[22.8]^2\Pi_{3/2}$ are shown in Figure 3.11 and Figure 3.12 . Using a variety of pump transitions, we exploit variations in the Frank-Condon factors which can be clearly seen by the difference in Figure 3.11 and Figure 3.12 . In Figure 3.11 given the relevant selection rules, $\Delta\Lambda = 0, \pm1$ and $\Delta\Omega = 0, \pm1,$[128] only vibronic transitions to the $X^2\Pi_{3/2}$,$A^2\Delta_{5/2}$ and $A^2\Delta_{3/2}$ states are allowed and we expect to see only these states in the SVL spectrum. Indeed this is evident in the spectra and also showing a shift in the Frank-Condon profile with intensity shifted to a higher wavenumber. In Figure 3.12 all five low-lying electronic states in the emission spectrum were identified, this also further confirms the symmetry of the excited state as $^2\Pi_{3/2}$.
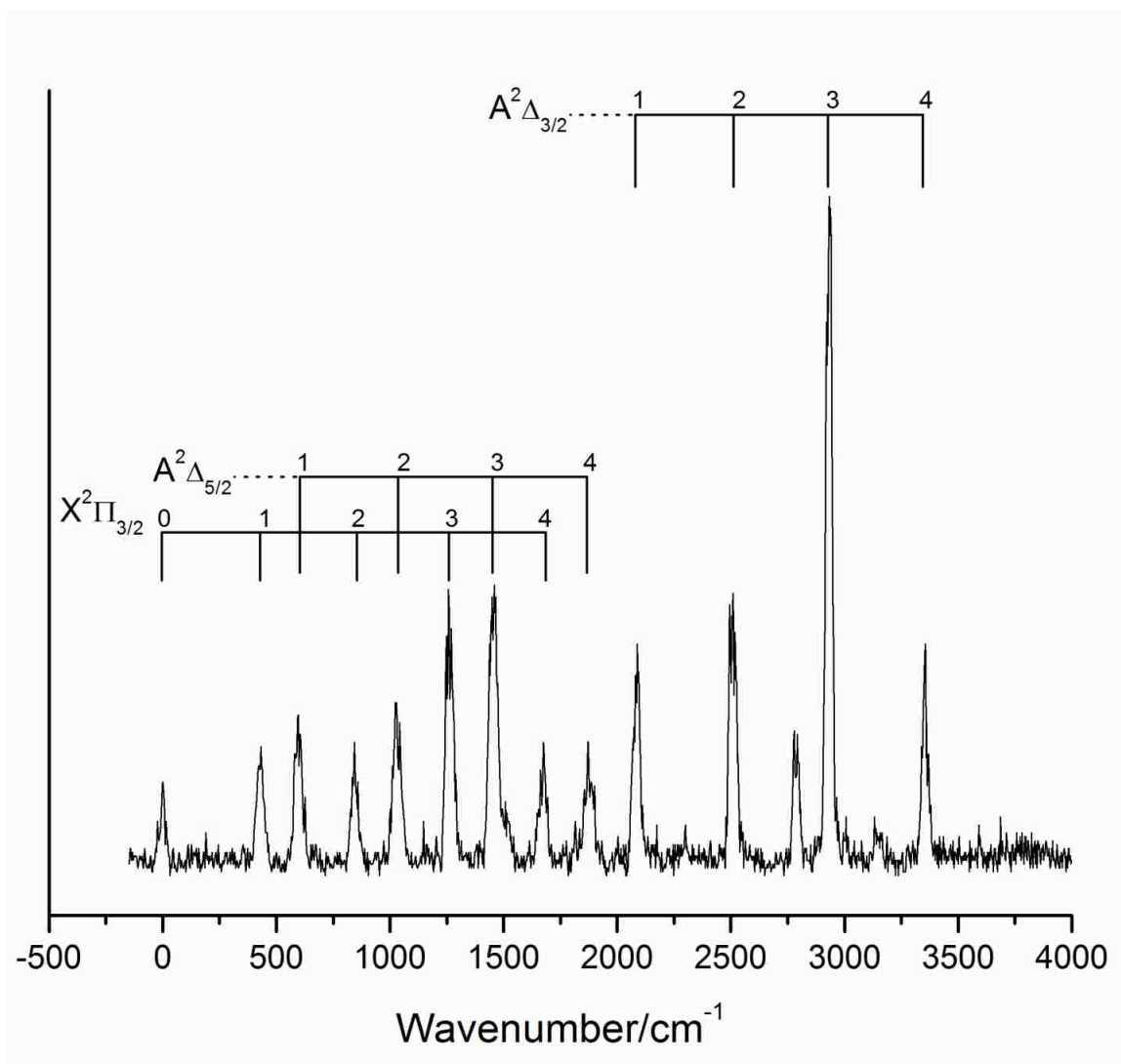
Figure 3.11: SVL spectra of NiCl recorded via (0-2) of the $[22.7]^2\Pi_{3/2}$ excited state bands; the x-axis labels the shift in cm^{-1} from the excitation line.
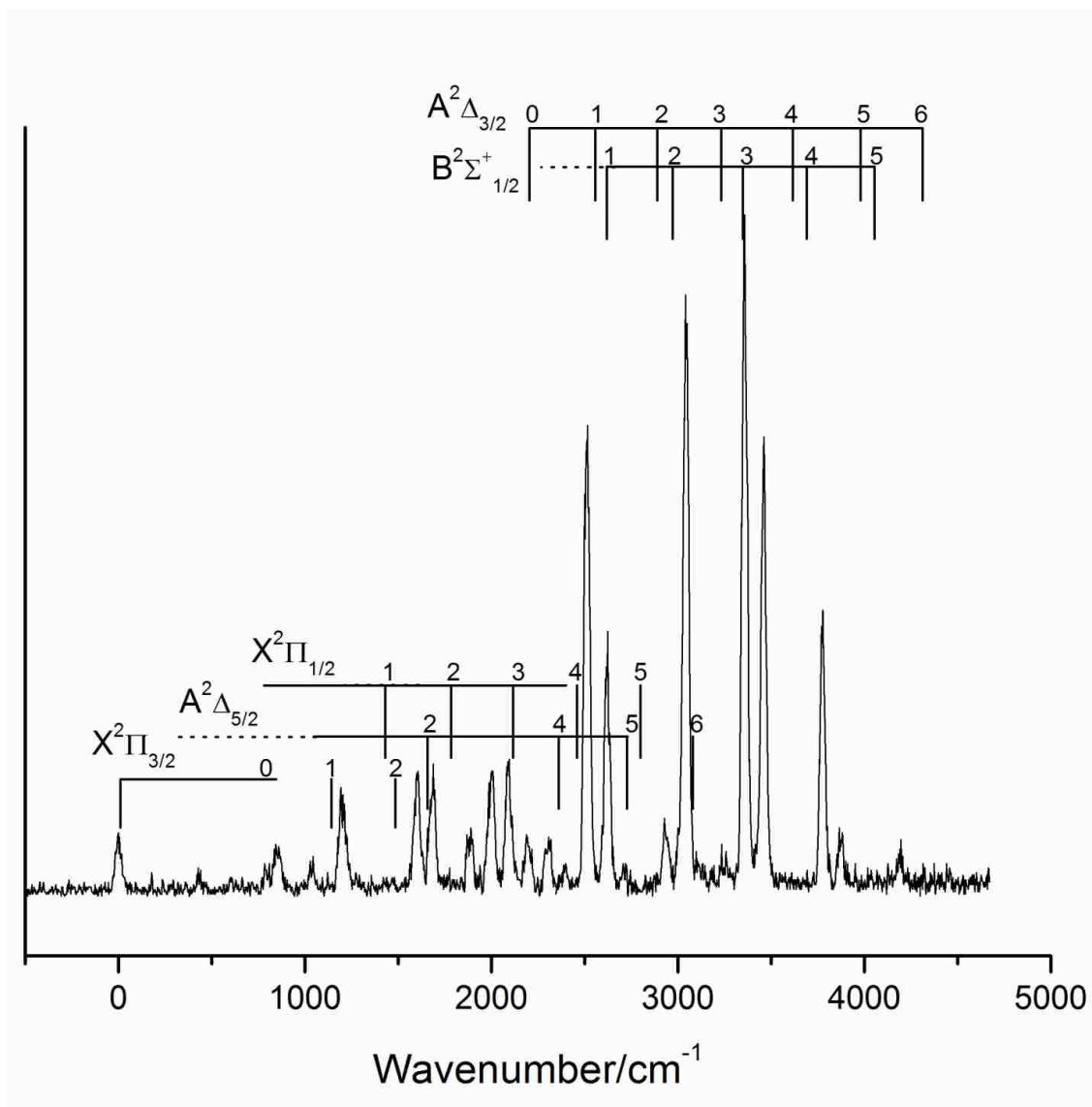
Figure 3.12: SVL spectra of NiCl recorded via (0-3) of the $[22.8]^2\Pi_{3/2}$ excited state bands; the x-axis labels the shift in cm^{-1} from the excitation line.

As for NiBr, the calibrated emission spectra peak energies of NiCl were fit to a Dunham expansion to derive term energies, harmonic frequencies, and anharmonicity constants. The parameters derived from the Dunham fit, together with assignments and associated uncertainties, are listed in Table 3.5. Included also in Table 3.5 are previous experimental[132,134] and theoretical[106] ω_e and T_e values.

Our experimental T_0 values are in good agreement with prior experimental and calculated values. Moreover, the trend in the experimental harmonic frequencies is in good agreement with the theoretical predictions. It can be noted from Table 3.5 that the experimentally derived harmonic vibrational frequencies for this work (21 621 - 23 182 cm^{-1}) are on the order of 430 cm^{-1}. The term energies and assignments of the low-lying electronic states of NiCl observed in this work are shown in Table 3.6. As found for NiBr, the fit residuals for all bands observed in the SVL spectra lie within our experimental error of ± 2 cm^{-1}, and no obvious vibronic perturbations were thus identified or assigned.

Table 3.5: Vibrational constants and term energies (in cm^{-1}) of the five low-lying electronic states of NiCl observed in the present work.

	$X^2\Pi_{3/2}$	$A^2\Delta_{5/2}$	$X^2\Pi_{1/2}$	$A^2\Delta_{3/2}$	$B^2\Sigma^+_{1/2}$	Source
T_0	0	166.90(1.76)[a] 268 158[b]	388.52 (0.26) 473 386	1654.37 (2.50) 1549 1646	1776.56 (10.29) 2002 1768	This work Ref.[107] Ref.[49,53]
ω_e	427.4 (1.76) 433 426	435.1 (1.65) 440 436	403.4 (0.94) 420 ------	433.1 (2.05) 439 432	425.56 (7.95) 433 ------	This work Ref.[107] Ref.[49,53]
x_e	-1.81 (0.49)	-1.62 (0.26)	-0.35(0.15)	-1.94 (0.28)	-1.70 (1.11)	This work

[a] One standard error given in parenthesis; [b] anharmonic values.

3.9.2. Perturbations involving the low-lying electronic states of NiCI

In general, interactions between electronic states with identical Ω are weaker as compared to the analogs of NiI and NiBr .The majority of the observed bands in the SVL emission spectra can be fit within our experimental error of ± 2 cm^{-1}. Figure 3.13 shows the residuals, where the deviation between observed and predicted peak energies is plotted for each of the five electronic states. As evident in Figure 3.13 , there are no obvious signs of strong perturbations for all the five lower states at least up to v=6 of the longest progression. The largest deviation between experimental energies and predicted values occurs for v=5 of A$^2\Delta_{5/2}$ at 2297 cm^{-1} (3.26 cm^{-1} shift) but however there is no other state with omega=5/2 to possibly interact with that state under the $\Delta\Omega = 0$ selection rule. The second deviation is the v=4 of the A$^2\Delta_{3/2}$ at 3350 cm^{-1} (3.10 cm^{-1} shift), the possibility of interaction may come from v=8 of the X$^2\Pi_{3/2}$ at 3288 cm^{-1} which can be predicted by the fits but not observed in our experiment. In this instance some of the few deviations outside the error can be attributed to experimental error as they are no potential perturbation candidates under the $\Delta\Omega = 0$ selection rule.
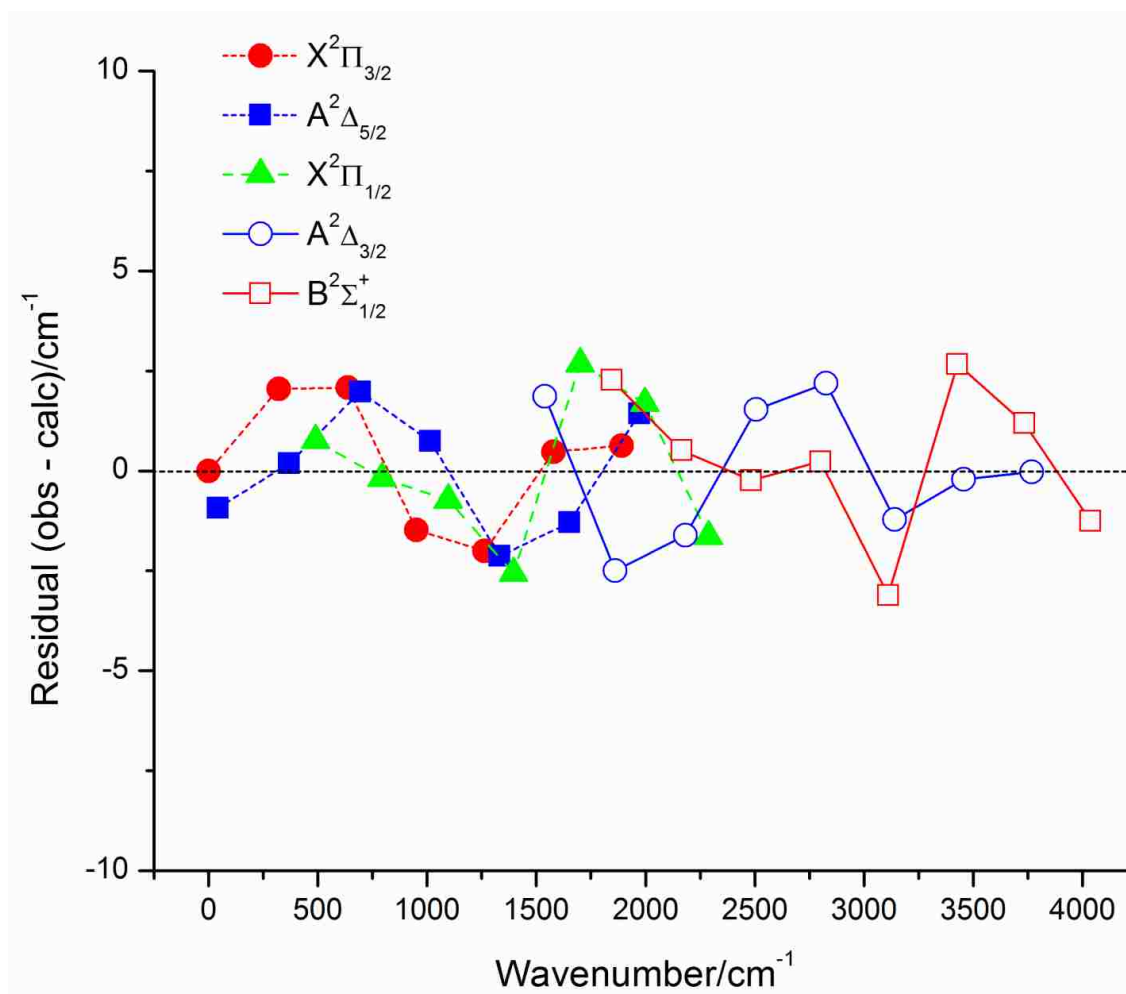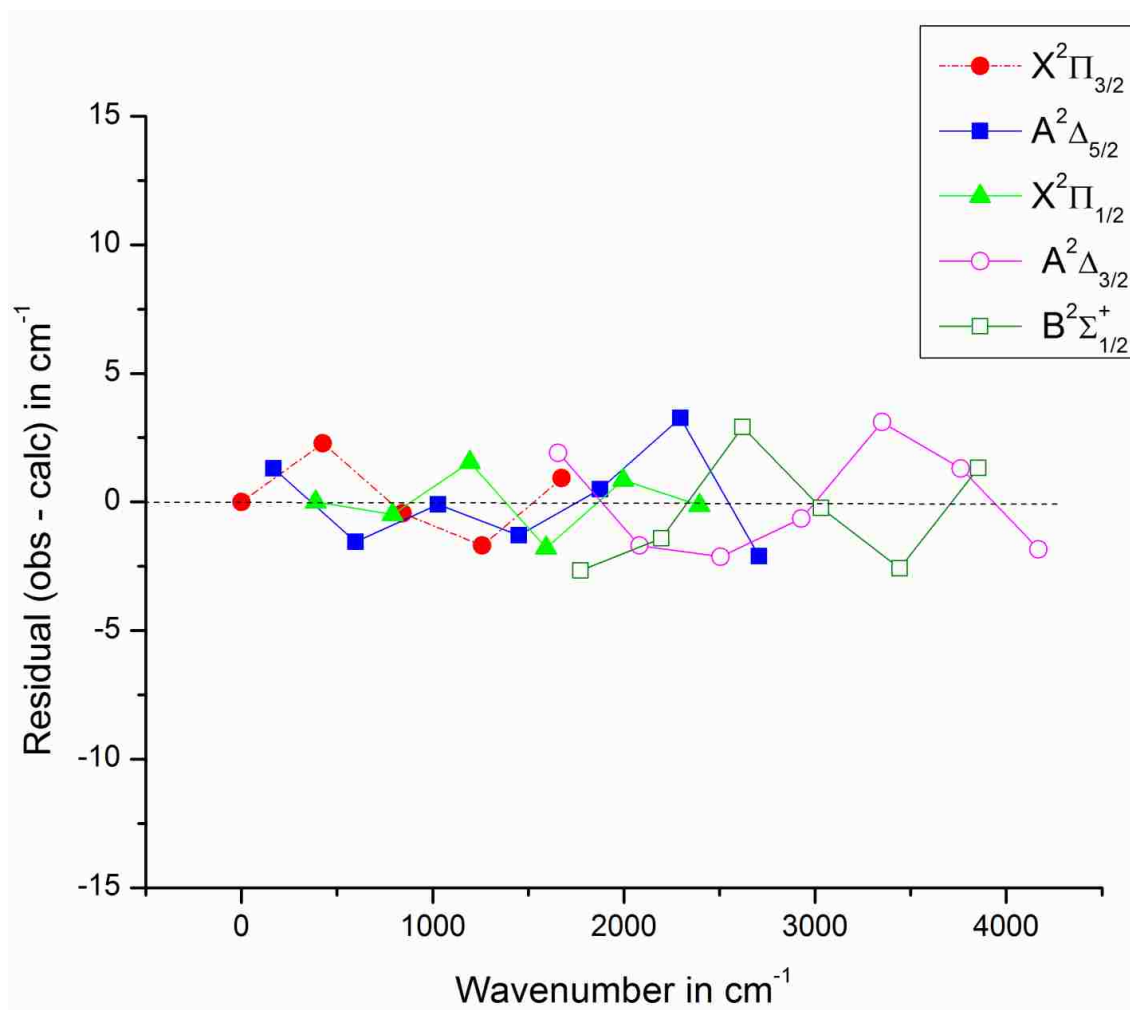
Figure 3.13: Residuals (Obs – Calc) of the vibrational levels observed in this work for the five lowest lying electronic states of NiCl. The x-axis labels the energy in cm^{-1} above the vibrationless level of the ground state. Calculated values were determined from fits, as described in the text.

Table 3.6: Term energies and assignments of the low-lying electronic states of NiCl observed in this work. The deviations (Obs –Cal) between experimental energies and those predicted by a fit of the experimental values to the Dunham expansion are also shown.

State	V	Energy/ Cm-1 Cal	Energy /Cm-1 Obs	Obs-Cal
$X^2\Pi_{3/2}$	0	0	0	0
	1	423	426	2
	2	843	843	-0
	3	1260	1258	-2
	4	1673	1674	1
$A^2\Delta_{5/2}$	0	166	168	2
	1	598	597	-1
	2	1027	1027	0
	3	1452	1451	-1
	4	1874	1875	1
	5	2293	2297	3
	6	2709	2707	-2
$X^2\Pi_{1/2}$	0	388	388	0
	1	791	790	-1
	2	1193	1194	1
	3	1594	1592	-2
	4	1995	1996	1
	5	2395	2395	0
$A^2\Delta_{3/2}$	0	1654	1656	2
	1	2083	2081	-2
	2	2508	2506	-2
	3	2930	2929	-1
	4	3347	3350	3
	5	3761	3762	1
	6	4171	4169	-2
$B^2\Sigma^+_{1/2}$	0	1776	1773	-3
	1	2198	2197	-1
	2	2617	2620	3
	3	3032	3032	0
	4	3444	3442	-2
	5	3853	3854	1

3.9.3.   Summary

We report LIF and SVL emission spectra of NiCl that probe the term energies and vibrational structure of the five low-lying electronic states ($X^2\Pi_{3/2}$, $A^2\Delta_{5/2}$, $X^2\Pi_{1/2}$, $A^2\Delta_{3/2}$ and $B^2\Sigma^+_{1/2}$) that arise from the $3d^9$ configuration of Ni^+. The excited state bands interrogated in this work were in the region 21 621 - 23 182 cm^{-1}. The experimentally derived harmonic frequencies and term energies trends derived in this work were consistent with the theoretical values of Zou and Liu[107] and experimental work of Poclet *et al*.[49,53] The derived harmonic frequencies and term energies can afford a detailed look at periodic trends across the Nickel monohalide series. In contrast to NiI but similar to NiBr, the spectra of NiCl show few vibronic perturbations, reflecting the smaller spin-orbit coupling in these systems.

3.10.   Laser induced fluorescence spectroscopy of NiI, NiBr and NiCI

Spectroscopic investigation of diatomic molecules involving transition metals yield molecular properties such as bond length and bond strength and also gives information concerning electronic structure and the occupation of molecular orbitals formed from a transition metal and a main group element.[123] Transition metal atom and main group atoms spectrum is often quite congested because of possible electronic states that are close in energy to each other and the unpaired electrons will give rise to many close-lying electronic states with high spin multiplicity.[123] Furthermore, the transition metals and main group atoms often have isotopes with appreciable abundance which leads to isotope splitting. Isotope splitting causes spectral overlap in the near vicinity.

High-resolution laser-induced fluorescence spectrum of a jet-cooled NiI molecule has been recorded in the near infrared and visible regions by Tam *et al*. The NiI molecule was produced by reacting laser-ablated nickel atom and methyl iodide (CH_3I). They identified three electronic states that include the $X\,^2\Delta_{5/2}$ and two low-lying [13.9] $^2\Pi_{3/2}$ and [14.6] $^2\Delta_{5/2}$ excited states.[102] Leung *et al* studied four electronic states of NiBr using the technique of laser vaporization/reaction with supersonic cooling and laser induced fluorescence (LIF) spectroscopy. NiBr molecules were produced by reacting laser ablated nickel atoms and ethyl bromide (C_2H_5Br). They identified the [13.2] $^2\,\Pi_{3/2}$–$X\,^2\,\Pi_{3/2}$ system, the [13.2] $^2\Pi_{3/2}$–$A\,^2\,\Delta_{5/2}$ system and the [12.6] $^2\Sigma^+$–$X\,^2\Pi_{3/2}$ system.[98] Band systems analogous to NiI and NiBr had also been recorded by Poclet *et al* [49] using high resolution Fourier transform spectroscopy. A characteristic excitation spectrum was

recorded in the spectral region of 20 000 to 25 000 cm^{-1}. This work includes the study of excited states of NiI, NiBr and NiCl using laser induced fluorescence spectroscopy in the spectral region 21 150 – 23 182 cm^{-1} under supersonic free jet expansion conditions.

3.10.1.   Experimental Details

The Nickel monohalides were produced using a pulsed electrical discharge through a mixture of an appropriate precursor seeded in ~3 bar Ar (Airgas); CD$_3$I (Sigma-Aldrich, 99.5+ %) for NiI, CH$_2$Br$_2$ for NiBr and C$_2$Cl$_4$ for NiCl. Discharge was initiated by a +1.3 kV pulse, with a width of 4 ms, later reduced to 100 ns. Timing of the laser, nozzle and discharge firing was controlled using a digital delay generator), which generated a variable width gate pulse for the high voltage pulser. A mutually orthogonal geometry of laser, molecular beam and detector was employed, with a laser system incorporating a tunable dye laser (Lambda-Physik, Scanmate 2E) pumped by the third harmonic of a Nd: YAG laser (Continuum NY-61). The laser dyes Coumarin 480, Coumarin 460 and Coumarin 440 were used, giving typical pulse energies of ~4–5 mJ. Total fluorescence was filtered via long-pass and short-pass cutoff filters (Corion or Edmund Scientific) prior to detection by a photomultiplier tube detector (Oriel) held at − 980 V. Fluorescence excitation spectra were calibrated to atomic Ar lines, using an Fe:Ar hollow cathode lamp (Photron).

3.10.2.   Spectral Analysis: NiI

3.10.2.1.   Excited state spectral analysis for NiI

Bands were observed in the energy range 21 000 – 22 400 cm^{-1}. This range includes a total of fifteen cold (transitions which comes from the v=0 of the ground state) as well as a small number of hot band (transitions which comes from vibrationally excited states (not necessarily v=0) of the ground state. The difference between the cold band transition and hot band transition can be depicted in Figure 3.21. Four progressions can be seen, originating at 21 158 cm^{-1}, 21 337 cm^{-1}, 21 852 cm^{-1} and 21 999 cm^{-1} with a spacing of ~219 cm^{-1}. The excited state symmetries in this work are assigned as [21.1]$^2\Pi_{3/2}$, [21.3]$^2\Delta_{5/2}$, [21.8]$^2\Sigma^+_{1/2}$ and [21.9]$^2\Pi_{3/2}$. A low resolution fluorescence excitation spectrum, recorded in the range 21 000 – 22 400 cm^{-1} includes all the excited state bands observed in this work is shown in Figure 3.14.
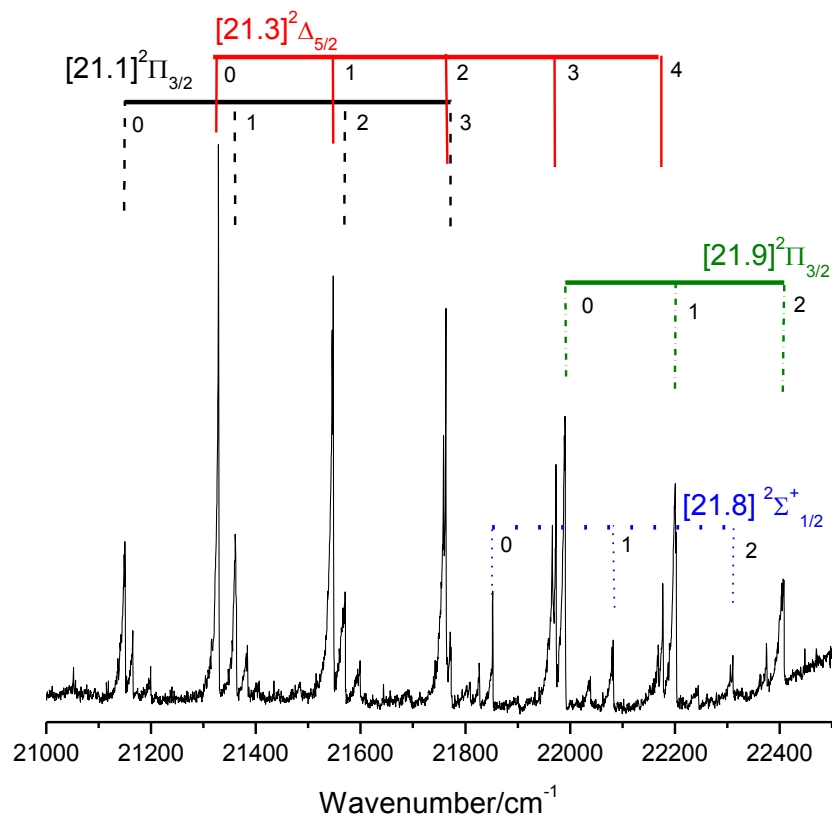
Figure 3.14 : A low resolution fluorescence excitation spectrum of NiI in the range 21 000 - 22 400 cm^{-1}.

To derive the excited state vibrational constants, each progression has been fitted to an expression of the form:

$$G(v) = T_{00} + v\omega' + v^2 x' \qquad \text{(Equation 3.1)}$$

The calibrated, R-branch band head energies of all the excited state bands are given in Table 3.8. Term energies and vibrational constants derived using the expression shown above is given in Table 3.7 . The similar spacing seen in the three progressions and the results of the SVL experiment described in chapter 3 indicate that the same species is responsible for all excited state bands observed in this region. An example of a high resolution spectrum of an excited state band for the origin (0-0) band of the $X^2\Delta_{5/2}$ to $^2\Delta_{5/2}$ transition compared to its simulated spectra is shown in Figure 3.15 . The rotational simulations were performed using the PGOPHER program[124]. The simulation is based on calculated rotational constants and rotational temperature of 50 K.
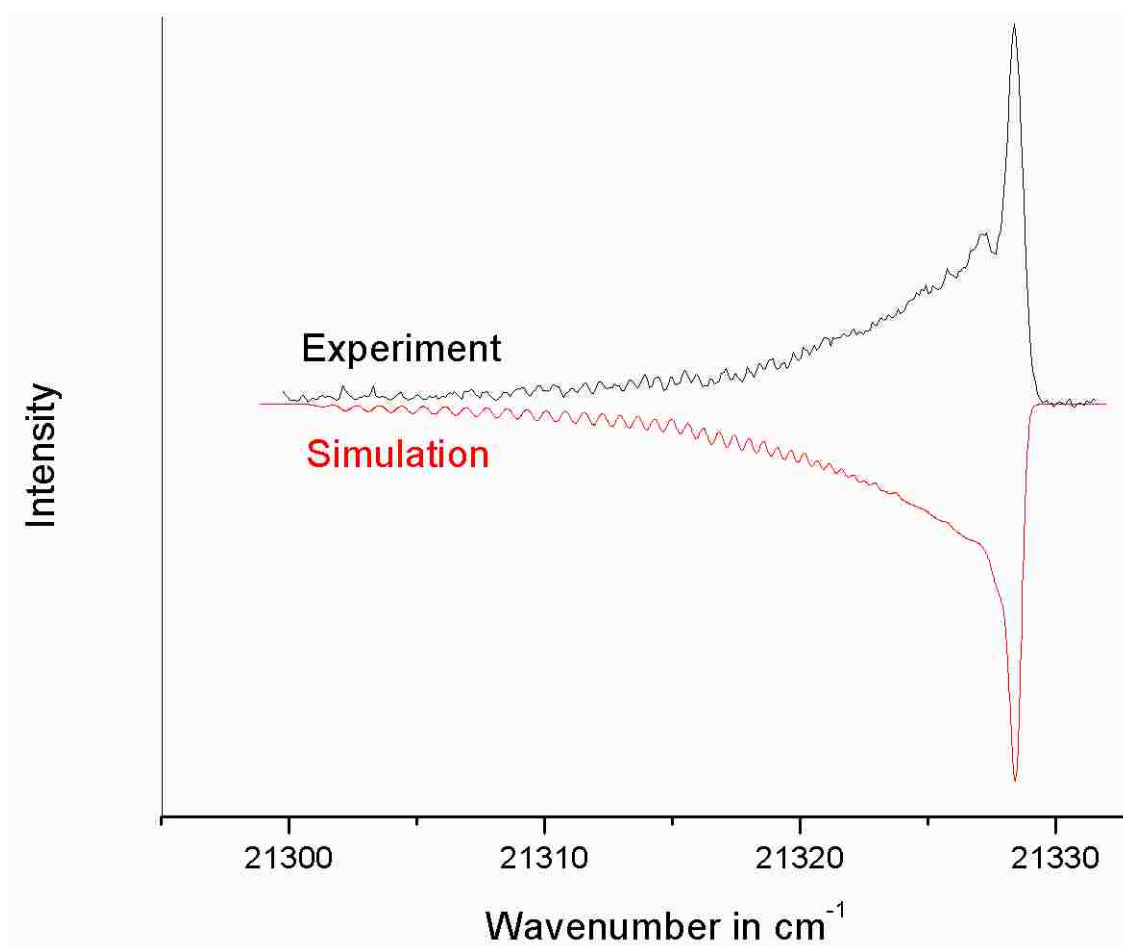
Figure 3.15 : Comparison of experimental and simulated spectra for the origin (0-0) band of the $X^2\Delta_{5/2}$ to $^2\Delta_{5/2}$ transition of NiI. The simulation is based on calculated rotational constants and rotational temperature of 50 K.

3.10.2.2.   Isotopic relation: ^{58}NiI and ^{60}NiI

The most common isotope of nickel is ^{58}Ni, which has a natural abundance of 68.1 percent. Other stable isotopes include ^{60}Ni (26.2%), ^{61}Ni (1.1%), ^{62}Ni (3.6%), and ^{64}Ni (0.9%). Molecular parameters of isotopic molecules are approximately related by different powers of the mass dependence $\rho = (\mu/\mu_i)^{1/2}$, which μ and μ_i are, respectively, the reduced mass of ^{58}NiX and ^{60}NiX.

Higher members of each progression are split; the energy difference between the high and low energy components increases linearly with the degree of vibrational excitation in the mode with $w_e = 219$ cm^{-1}. This splitting is particularly apparent in members of the most intense progression, which originates at 21 337 cm^{-1}; a high resolution LIF spectrum of the origin (0-0) and the second member (0-2) of the X$^2\Delta_{5/2}$ to $^2\Delta_{5/2}$ is shown in Figure 3.15 and Figure 3.16 respectively. Rotational simulations using the PGOPHER program[124] were performed for all excited state bands observed herein. In all cases, the most successful replication of the experimentally observed rotational contour was achieved with a rotational temperature of 50 ± 7 K. The simulations confirm the assignments of the excited state symmetries. The experimental spectra together with their corresponding simulations are also shown in Figure 3.15 and Figure 3.16 , these confirm the assignment of the $^2\Delta_{5/2}$ of the excited state for NiI. Figure 3.17 and Figure 3.18 also show the experimental spectra together with their simulated spectra, the simulations further confirm the symmetries of the two $^2\Pi_{3/2}$ states observed for NiI.

The magnitude of the isotope splitting for all relevant bands is shown in Figure 3.19. SVL spectra recorded via the high and low energy components were identical. The splitting can be accounted to by isotope splitting. The examination of the isotopic displacement from band origins of the isotopes also further confirms our vibrational quantum number assignments.
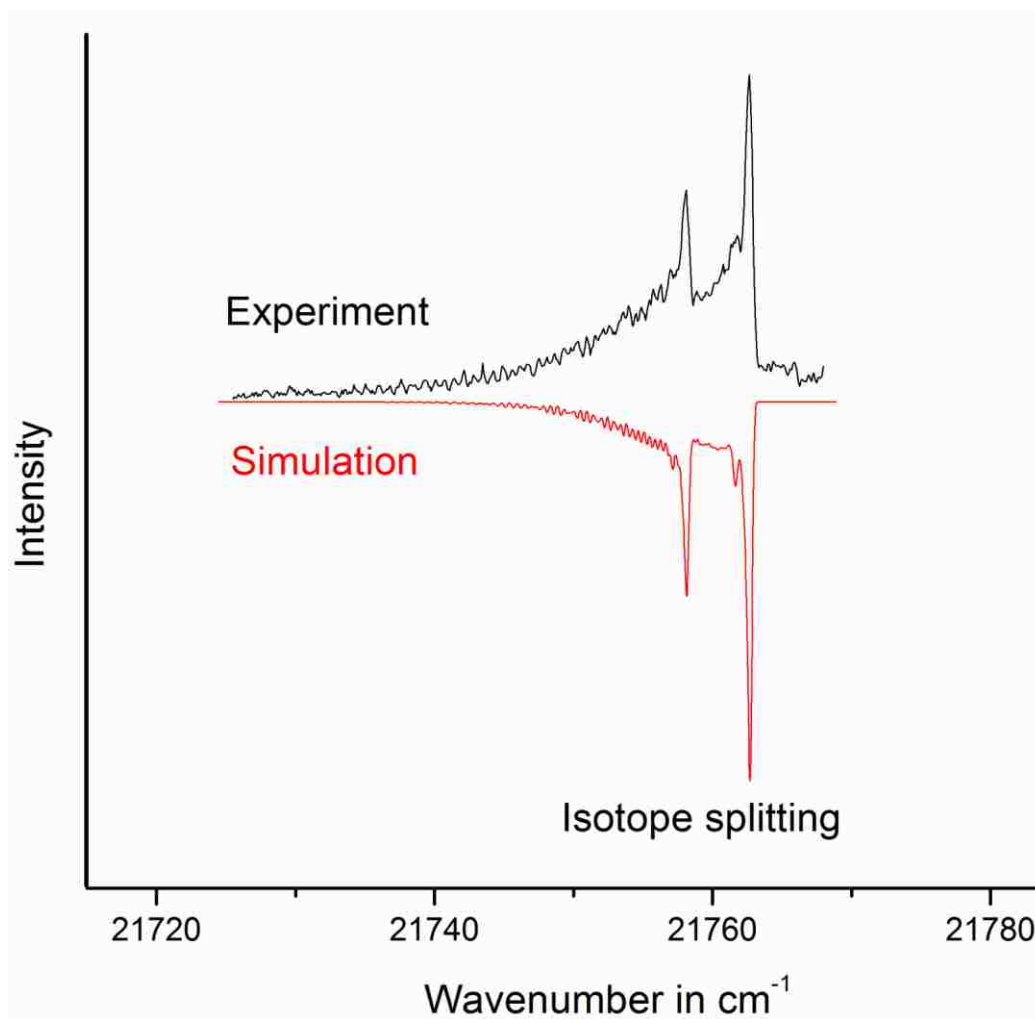
Figure 3.16 : Comparison of experimental and simulated (0-2) band of the $X^2\Delta_{5/2}$ to $^2\Delta_{5/2}$ transition of NiI. The simulation is based on calculated rotational constants and rotational temperature of 50 K.
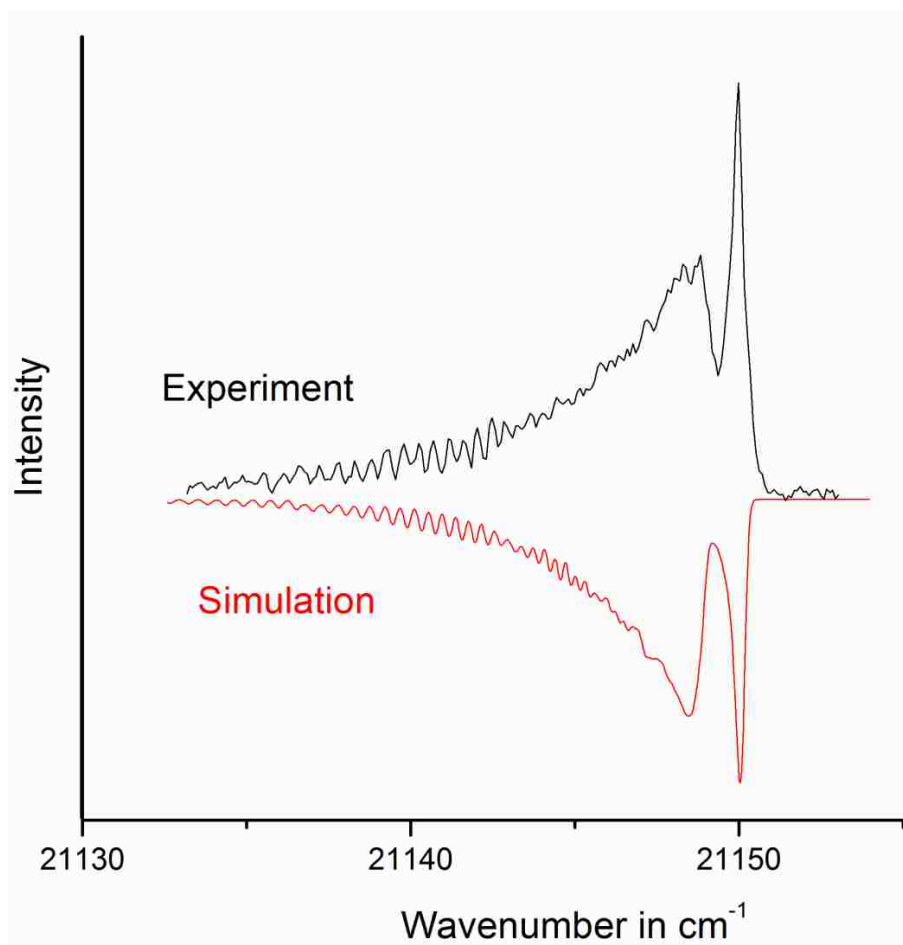
Figure 3.17 : Comparison of experimental and simulated (0-0) bands of the $X^2\Delta_{5/2}$ to [21.1] $^2\Pi_{3/2}$ transition of NiI. The simulation is based on calculated rotational constants and rotational temperature of 50 K.
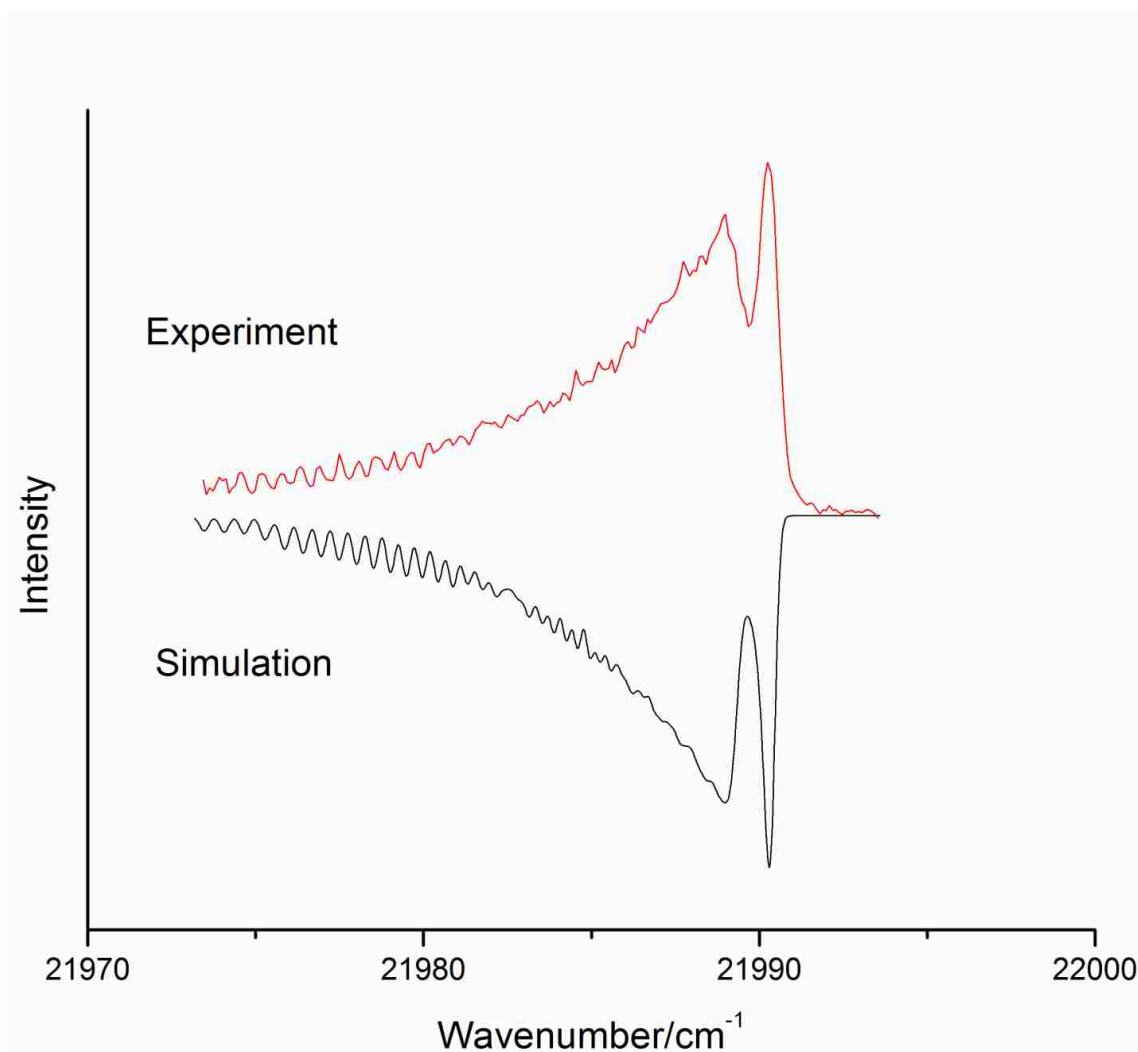
Figure 3.18 : Comparison of experimental and simulated (0-0) bands of the $X^2\Delta_{5/2}$ to the [21.9] $^2\Pi_{3/2}$ transition of NiI. The simulation is based on calculated rotational constants and rotational temperature of 50 K.

Table 3.7 : Term energies and vibrational constants of the excited states observed herein for NiI.

State	Isotope	x_e (cm^{-1})	ω_e (cm^{-1})	T_{00} (cm^{-1})
[21.1] $^2\Pi_{3/2}$				
	^{58}NiI	-2.69	215.63	21149
	^{60}NiI	-2.69	213.42	21149
[21.3] $^2\Delta_{5/2}$				
	^{58}NiI	-2.65	222.7	21327
	^{60}NiI	-2.61	220.29	21327
[21.9] $^2\Pi_{3/2}$				
	^{58}NiI	-3.23	215.42	21989
	^{60}NiI	-3.17	213.14	21989

3.10.2.3.   Rotational constants for NiI

Ground state vibrational energies have been determined from SVL spectra recorded via a total of fifteen excited state bands. The fact that we excite SVL on these states also helped us further confirms the symmetries of the excited states. From the simulations of the experimental bands using PGOPHER program, the B_0 rotational constants are 0.071 cm^{-1}, 0.0692 cm^{-1} and 0.0714 cm^{-1} for the $[21.1]^2\Pi_{3/2}$, $[21.3]^2\Delta_{5/2}$ and $[21.9]^2\Pi_{3/2}$ states, corresponding to (R_0) bond lengths of 2.43 Å, 2.46 Å and 2.42 Å respectively .

Table 3.8 : Calibrated R-branch band head energies and Rotational Constant B in cm^{-1} of all excited state bands for NiI.

State	V	Isotope	Band head energies	Rotational Constant B
[21.1] $^2\Pi_{3/2}$				
	0		21148.90	0.0720
	1	^{58}Ni	21361.65	0.7150
		^{60}Ni	21359.55	0.7150
	2	^{58}Ni	21569.50	0.7060
		^{60}Ni	21565.12	0.0706
	3	^{58}Ni	21771.50	0.7020
		^{60}Ni	21765.10	0.7020
[21.3] $^2\Delta_{5/2}$				
	0		21327.80	0.6960
	1	^{58}Ni	21546.75	0.7150
		^{60}Ni	21544.60	0.7150
	2	^{58}Ni	21761.75	0.7150
		^{60}Ni	21757.20	0.7150
	3	^{58}Ni	21971.90	0.7100
		^{60}Ni	21965.10	0.7100
	4	^{58}Ni	22176.40	0.7050
		^{60}Ni	22167.40	0.7040
	5	^{58}Ni	22374.05	0.7050
		^{60}Ni	22363.20	0.7040
[21.9] $^2\Pi_{3/2}$				
	0		21989.30	0.0715
	1	^{58}Ni	22201.50	0.0713
		^{60}Ni	22199.27	0.0713
	2	^{58}Ni	22407.25	0.0705
		^{60}Ni	22402.90	0.0705
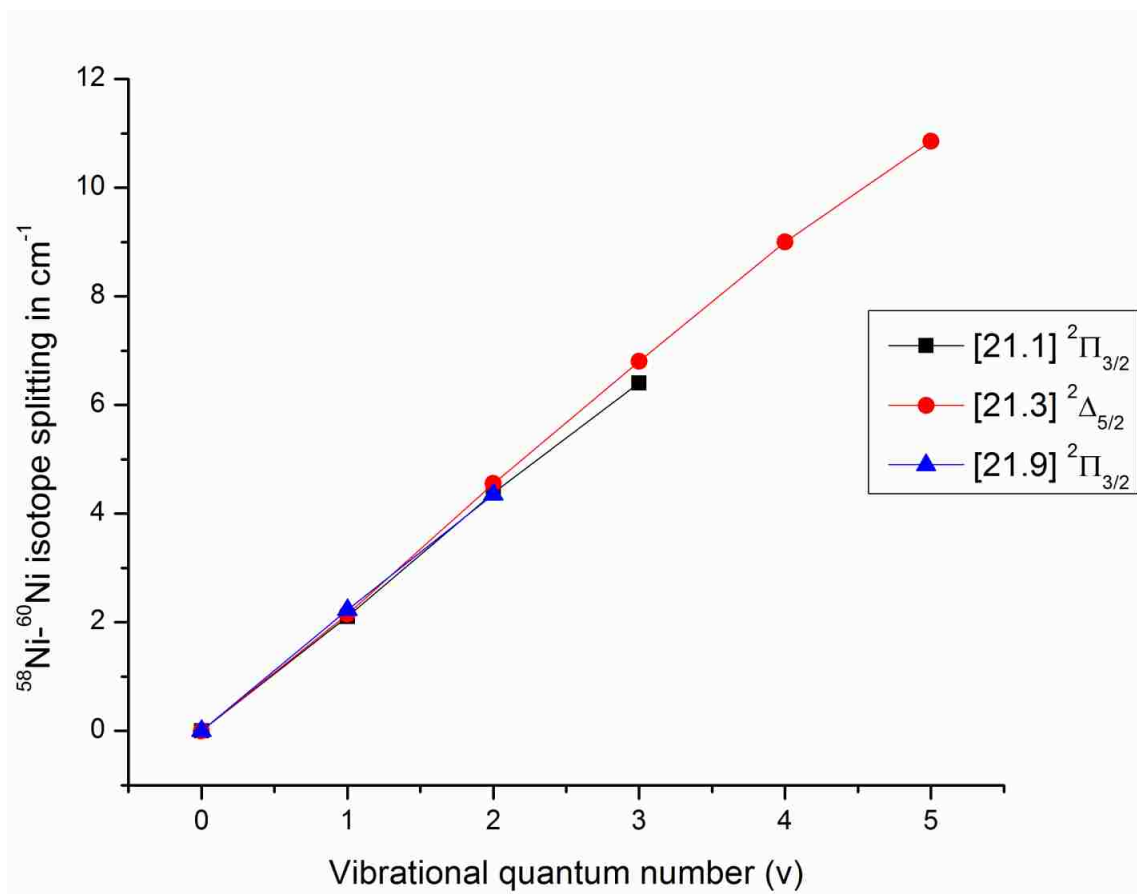
Figure 3.19 : Magnitude of the isotope splitting for all relevant bands for NiI.

3.10.3.   Spectral Analysis: NiBr

3.10.3.1.   Excited state spectral analysis for NiBr

Bands observed in the energy range 21 500 – 23 500 cm^{-1}. This range includes a total of seventeen cold bands as well as a significant number of hot bands. Four progressions can be seen, originating at [21.5] cm^{-1}, [21.7] cm^{-1} [22.3] cm^{-1} and [22.4] cm^{-1} with a spacing of ~320 cm^{-1}. A low resolution fluorescence excitation spectrum, recorded over the above range includes all the excited state bands observed is shown in Figure 3.20. To derive vibrational constants, each progression has been fit to an expression as shown in Equation 3.1 above. Term energies and vibrational constants derived using the expression shown above is tabulated in Table 3.9.

The calibrated, R-branch band head energies and rotational constants of all the excited state bands observed for NiBr are given in Table 3.10. Found for NiI, the higher members of each progression are split; the energy difference between the high and low energy components increases linearly with the degree of vibrational excitation. A high resolution LIF spectrum of the origin (0-0) of the X$^2\Pi_{3/2}$ to $^2\Pi_{3/2}$ transition and the second member (0-0) of the X$^2\Pi_{3/2}$ to $^2\Pi_{3/2}$ are shown in Figure 3.22.
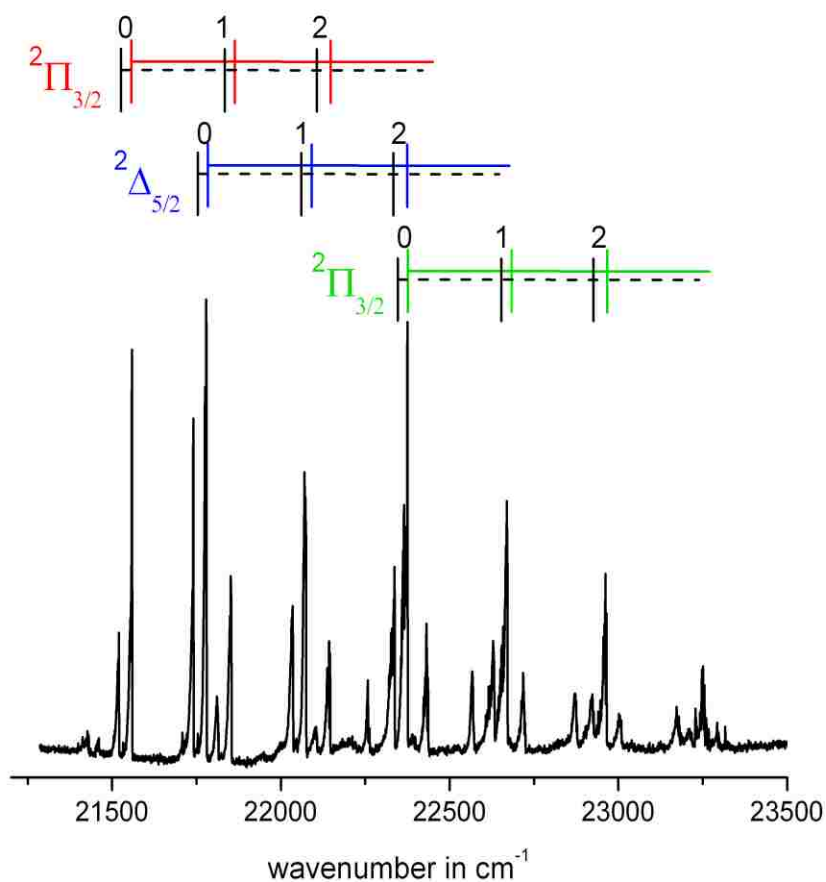
Figure 3.20 : A survey laser induced fluorescence spectrum of NiBr. The assignments of the main progression are noted. In each case, the solid lines represent transitions from the $X^2\Pi_{3/2}$ ground state, and the dotted lines represent transitions from the low lying $A^2\Delta_{5/2}$ state.

For NiI, rotational simulations were performed using the PGOPHER[124] program to simulate the excited state bands observed for NiBr. In all cases, the most successful replication of the experimentally observed rotational contour was achieved with a rotational temperature of 50 ± 7 K, same as found for NiI. The experimental spectra together with their corresponding simulations are also shown in Figure 3.22, Figure 3.23 and Figure 3.24. The simulations confirm the symmetries of the excited states observed in this work for NiBr. From the simulations of the experimental bands, the B_0 rotational constants are 0.101 cm^{-1}, 0.095 cm^{-1} and 0.098 cm^{-1} for the $[21.5]^2\Pi_{3/2}$, $[21.7]^2\Delta_{5/2}$ and $[22.3]^2\Pi_{3/2}$ states, corresponding to (R_0) bond lengths of 2.03 Å, 2.09 Å and 2.07 Å respectively .The magnitude of the isotope splitting for all relevant isotope bands for NiBr is shown in Figure 3.25.

3.10.3.2. Hot bands

Hot bands are transitions arising from vibrationally excited states in the ground state, as illustrated in Figure 3.21. There is a noticeable appearance of hot bands in the NiBr spectrum (Figure 3.20). The hot band transitions originate at 21 564 cm^{-1} and 21 785 cm^{-1}. Although not labeled; they can be clearly seen in Figure 3.20. The hot band can be confirmed by the low intensity as compared to the corresponding cold band transition and also by their appearance to the lower energy (low wavenumber) in relation to the analogous cold band. To confirm hot band transitions, SVL emission spectroscopy was carried out to measure the energy spacing between v=0 (cold) and v=1 (hot) as shown in Figure 3.21 . The hot band transitions also displayed isotope spitting which can be seen in Figure 3.25.
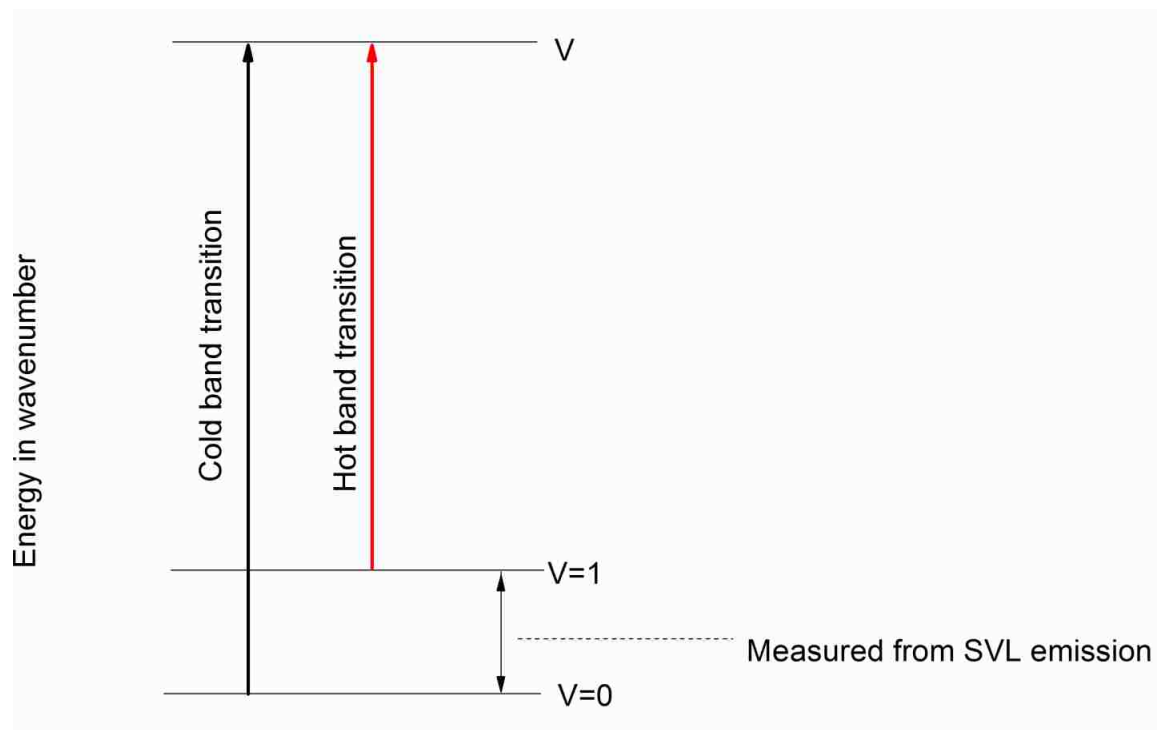
Figure 3.21 : Schematic diagram illustrating cold and hot band transitions.
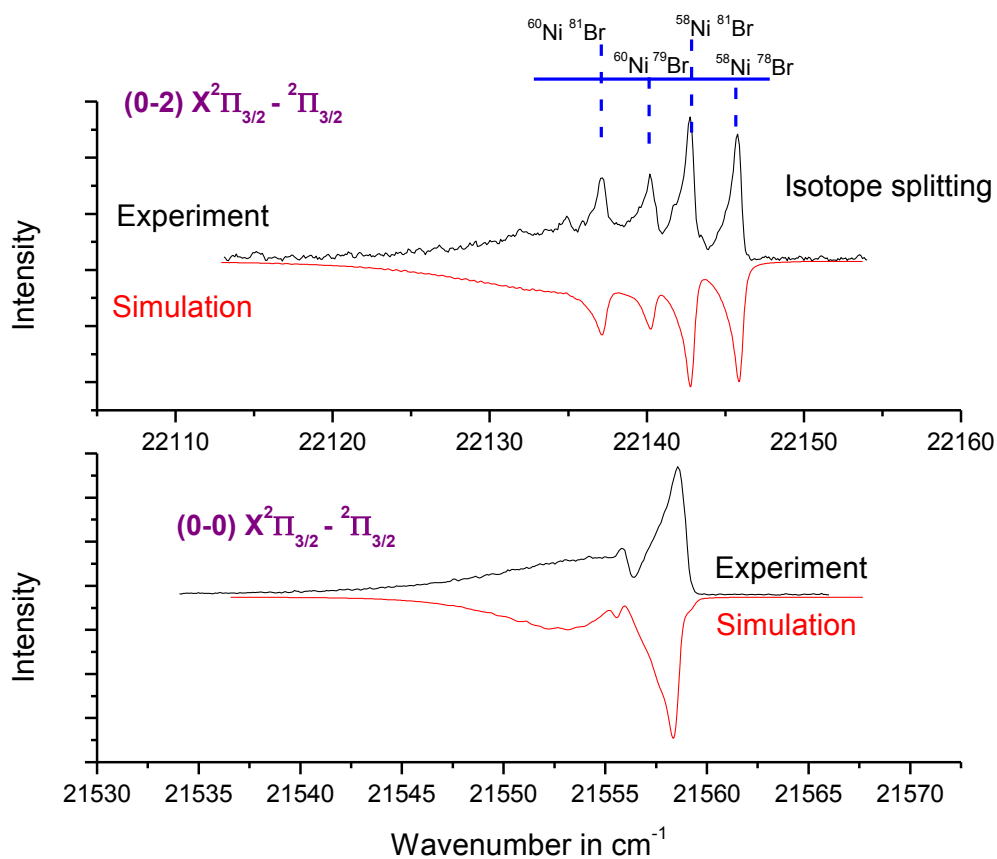
Figure 3.22 : Comparison of experimental (upper) and simulated (below) spectra for the origin (0-0) (lower trace) and (0-2) (upper trace) band for $X^2\Pi_{3/2}$ to $[21.6]\ ^2\Pi_{3/2}$ transition of NiBr. The simulation is based on calculated rotational constants and a rotational temperature of 50 K.
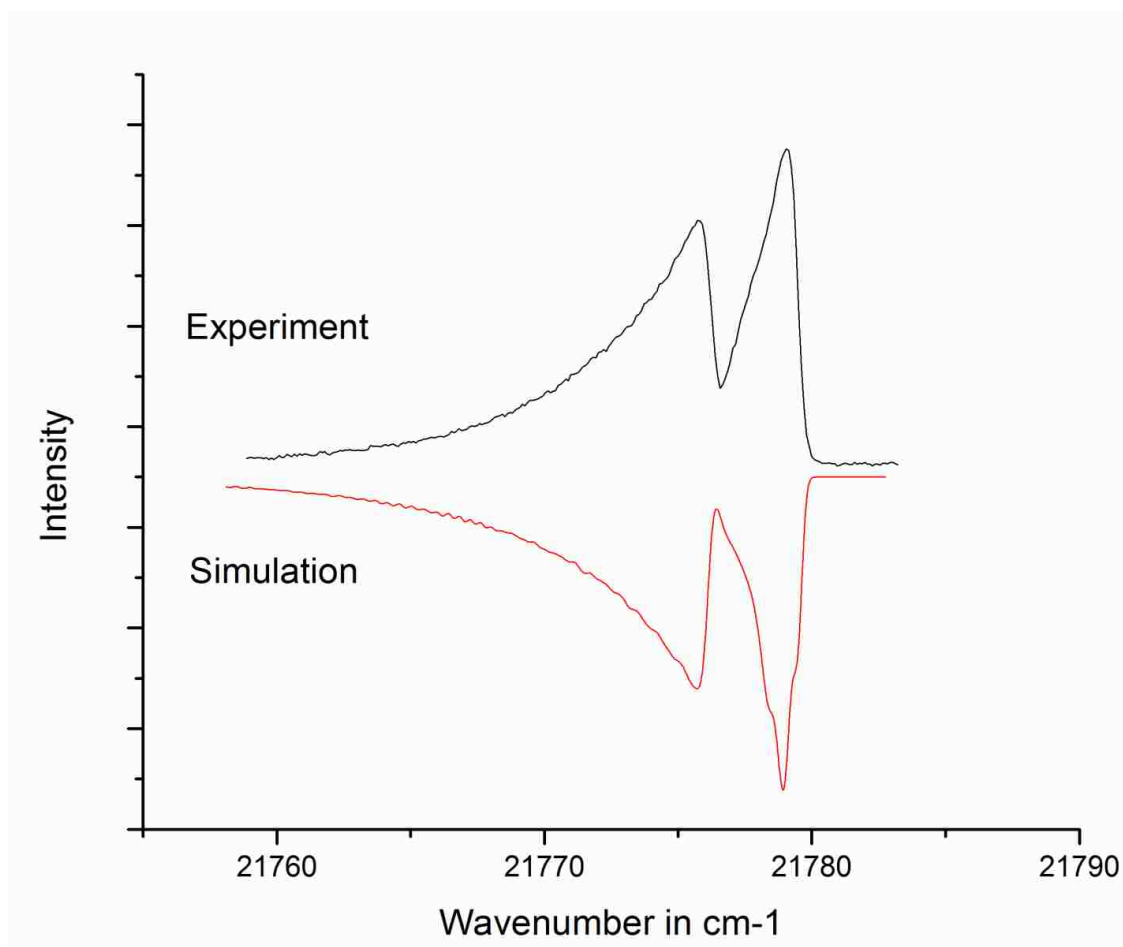
Figure 3.23 : Comparison of experimental and simulated (0-0) bands of the $X^2\Pi_{3/2}$ to $^2\Delta_{5/2}$ transition of NiBr. The simulation is based on calculated rotational constants and rotational temperature of 50 K.
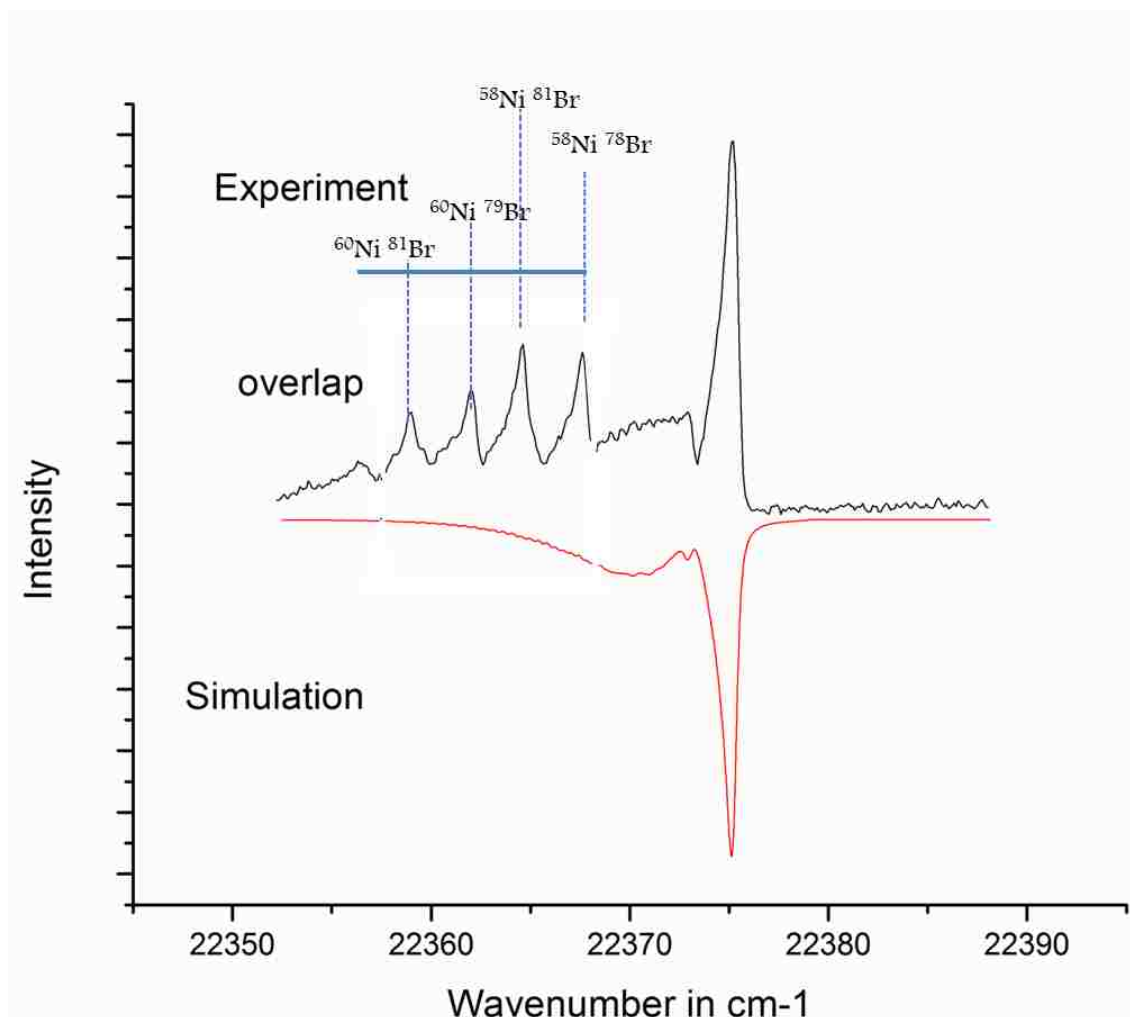
Figure 3.24 : Comparison of experimental and simulated (0-0) bands of the $X^2\Pi_{3/2}$ to the [22.4] $^2\Pi_{3/2}$ transition of NiBr. The four peaks on the left is the overlap of the (0-2) band of the $\Pi_{3/2}$ - $^2\Delta_{5/2}$. The simulation is based on calculated rotational constants and rotational temperature of 50 K.
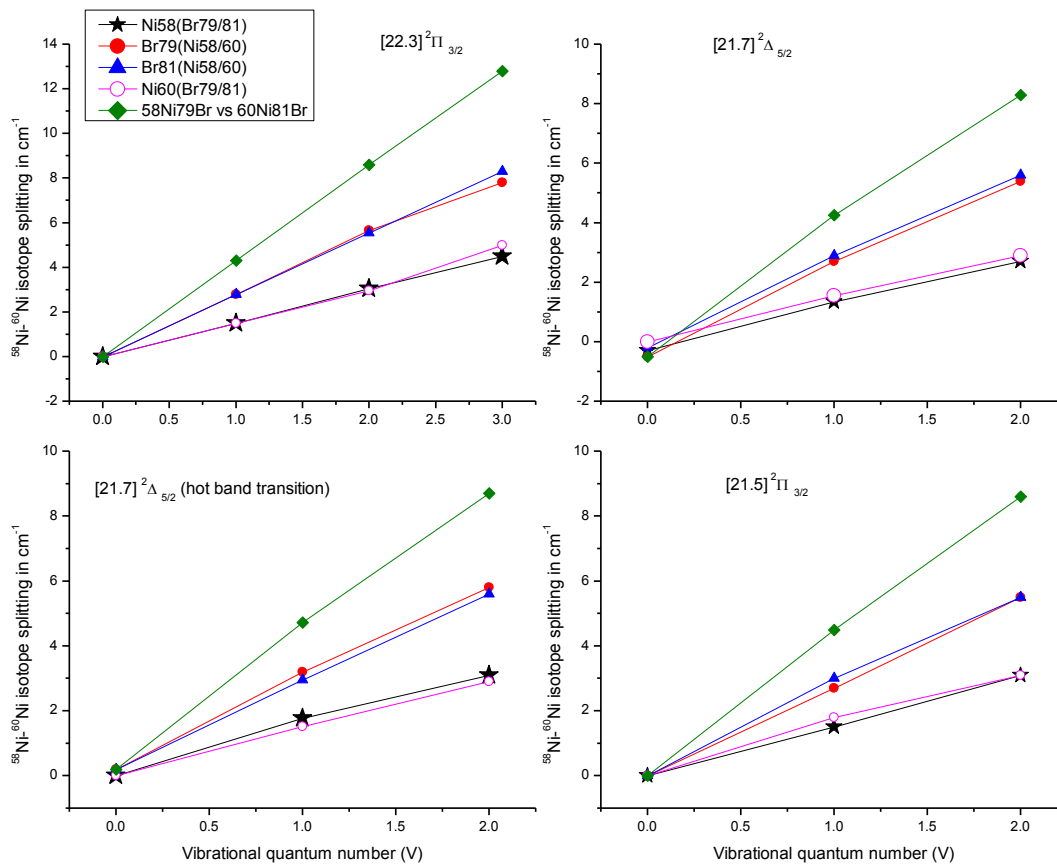
Figure 3.25 : Magnitude of the isotope splitting for all relevant bands for NiBr.

Table 3.9 : Term energies and vibrational constants of the excited states observed herein for NiBr.

State	Isotope	x_e (cm^{-1})	w_e (cm^{-1})	T_{00} (cm^{-1})
[21.5] $^2\Pi_{3/2}$				
	^{60}Ni^{81}Br	-1.15	296.16	20971
	^{60}Ni^{79}Br	-1.28	298.47	20967
	^{58}Ni^{81}Br	-1.15	298.96	20965
	^{58}Ni^{79}Br	-1.11	300.20	20963
[21.7] $^2\Delta_{5/2}$				
	^{60}Ni^{81}Br	-1.06	296.22	21191
	^{60}Ni^{79}Br	-1.06	297.72	21188
	^{58}Ni^{81}Br	-1.11	299.31	21185
	^{58}Ni^{79}Br	-1.10	300.74	21182
[22.3] $^2\Pi_{3/2}$				
	^{60}Ni^{81}Br	-1.17	297.34	21785
	^{60}Ni^{79}Br	-1.14	298.70	21782
	^{58}Ni^{81}Br	-1.20	300.31	21779
	^{58}Ni^{79}Br	-1.20	301.83	21776

Table 3.10 : Calibrated R-branch band head energies and Rotational Constant B in cm^{-1} of all excited state bands for NiBr.

State	V	parameter	^{58}Ni^{79}Br	^{58}Ni^{81}Br	^{60}Ni^{79}Br	^{60}Ni^{81}Br
[21.5] $^2\Pi_{3/2}$						
	v=0	Origin	21564.6	21564.6	21564.6	21564.6
		B	0.101	0.100	0.099	0.099
	v=1	Origin	21851.9	21850.4	21849.2	21847.4
		B	0.098	0.097	0.096	0.095
	v=2	Origin	22152.5	22149.4	22147.0	22143.9
		B	0.101	0.100	0.099	0.098
[21.7] $^2\Delta_{5/2}$						
	v=0	Origin	21776.2	21776.5	21776.7	21776.7
		B	0.101	0.100	0.099	0.097
	v=1	Origin	22082.9	22081.5	22080.2	22078.6
		B	0.097	0.096	0.095	0.094
	v=2	Origin	22366.2	22363.5	22360.8	22357.9
		B	0.099	0.098	0.097	0.096
$^2\Delta_{5/2}$ to [21.7] $^2\Delta_{5/2}$ (Hot band transition)	v=0	Origin	21785.3	21785.3	21785.1	21785.1
		B	0.101	0.100	0.099	0.097
	v=1	Origin	22082.0	22080.2	22078.8	22077.3
		B	0.098	0.097	0.096	0.095
	v=2	Origin	22365.9	22362.8	22360.1	22357.2
		B	0.098	0.097	0.096	0.095
[22.3] $^2\Pi_{3/2}$						
	v=0	Origin	22373.0	22373.0	22373.0	22373.0
		B	0.100	0.099	0.098	0.970
	v=1	Origin	22668.8	22667.3	22666.0	22664.5
		B	0.100	0.099	0.098	0.970
	v=2	Origin	22962.3	22959.2	22956.6	22953.7
		B	0.099	0.099	0.099	0.099
	v=3	Origin	23253.3	23248.8	23245.5	23240.5
		B	0.099	0.099	0.099	0.099

3.10.4.   Spectral Analysis: NiCl

3.10.4.1.   Excited state spectral analysis for NiCl

NiCI bands were observed in the energy range 21 500 – 24 000 cm^{-1}. This range includes a total of eleven cold bands as well as a small number of hot bands. Three progressions can be seen, with a spacing of ~ 420 cm^{-1}. A low resolution fluorescence excitation spectrum, recorded over the above range includes all the excited state bands observed is shown in Figure 3.26. However more work still need to be done to derive the vibrational constants for the excited states. For the purposes of analyzing the periodic trend, we had enough information from the SVL spectra.
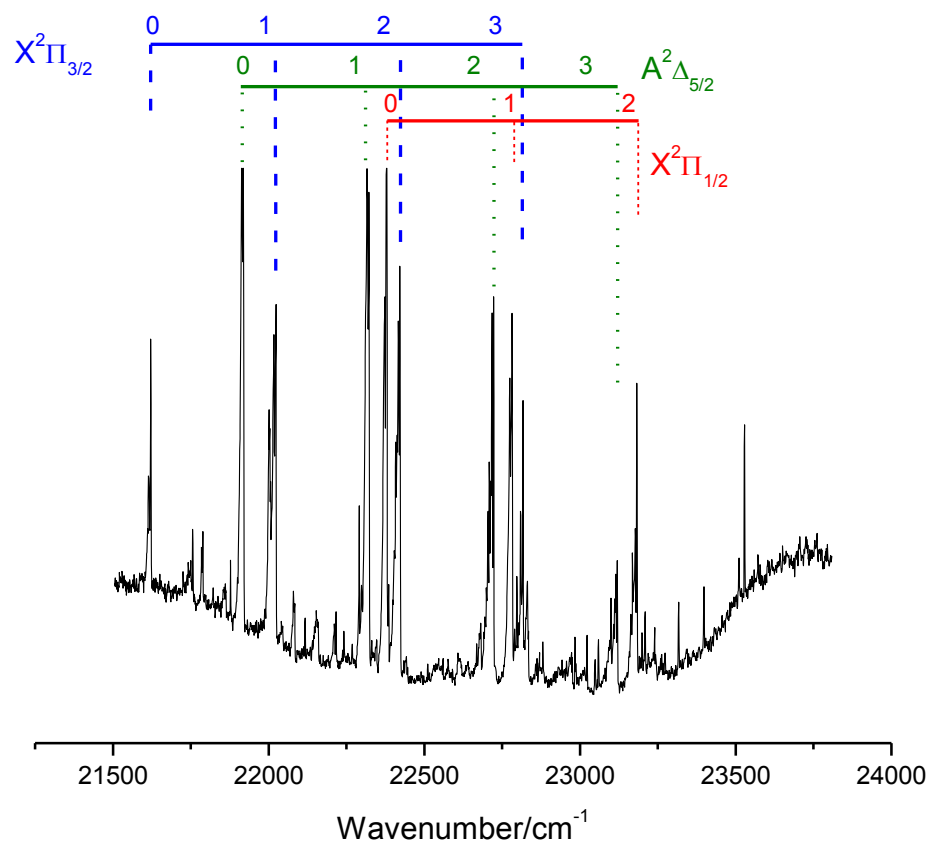
Figure 3.26 : A low resolution fluorescence excitation spectrum of NiCl in the range 21 500-24 000 cm^{-1}.

3.10.5. Summary

Excited state states of NiI, NiBr and NiCI have been identified and analyzed in this work. The nickel monohalides were probed in the energy range 21 000 – 24 000 cm^{-1}. The band structure was generally complex due to the appearance of isotope species and generally small rotational constants. Overall, the computed spectroscopic constants and simulations for all the three molecules are in good agreement with the available theoretical data. The derived harmonic frequencies and term energies form the SVL emission spectra and the analysis of the LIF for the excitation bands for NiI, NiBr and NiCl, can afford a detailed look at periodic trends across the Nickel monohalide series.

Chapter 4.   **PERIODIC TRENDS IN SPECTRAL ANALYSIS OF
NICKEL MONOHALIDES**

4.1. Introduction

Diatomic systems of 3d transition metals have been extensively studied both experimentally and theoretically for a long time but the knowledge about their electronic structure would be of great help for a better understanding of larger systems containing heavier transition metals.[106] It is expected that the electron distribution of these metal halides depends upon electron affinity of the atoms. The halogen atoms have larger electronegativity and would be able to attract electron distribution closer to it; therefore, nickel halides are basically ionic.[98]

It would be useful to examine the ground and low-lying states of NiI, NiBr, NiCl and NiF to understand the effects of the halogen as a ligand to split the d orbitals of the transition metal atom. It is also interesting to compare in detail the spectroscopic properties of various monohalides, to examine the effects of the halogens as a ligand to the transition metal d orbitals, to compare the change in the bond character and electronic structure of MX, when a hydrogen atom is substituted by a halogen atom. The bond length of the electronic states is expected to increase down the group due to the increase in the size of the atom down the group. This will also have an effect on the vibrational frequencies and force constants.

4.2. Trend in ordering of states of nickel monohalides

The data collected in this work thus far can afford a detailed look at periodic trends in the Nickel monohalide series NiX (X=F, Cl, Br, I) associated with the low-lying electronic states ($X^2\Pi_{3/2}$, $A^2\Delta_{5/2}$, $X^2\Pi_{1/2}$, $A^2\Delta_{3/2}$ and $B^2\Sigma^+_{1/2}$) that arise from the $3d^9$ configuration of Ni^+. As a starting point, we examine the trend in term energy for these levels.

Figure 4.1 compares experimental term energies with the recent theoretical predictions of Zou and Liu.[33] The values for NiCl, NiBr, and NiI are taken from our SVL emission studies, while that for NiF is taken from the literature.[135-137] Several trends are apparent. For NiF, the ground state is $^2\Pi_{3/2}$, and the A $^2\Delta_{5/2}$ state lies ~ 800 cm^{-1} above; however, in the heavier halogens, the splitting between these levels decreases, so that in NiI the ordering is switched. This trend is well reproduced by theory. At the same time, the position of the $B^2\Sigma^+_{1/2}$ increases with energy in the heavier halides, so that in NiI it is the highest lying of these levels. However this trend is not as well reproduced in the calculations.

Also informative are the trends in the spin-orbit splitting of the $^2\Pi$ and $^2\Delta$ levels, shown in more detail in Figure 4.2 . In the case of the $^2\Delta$ state, the spin-orbit splitting increases in going from the fluoride to chloride, but is relatively constant for the heavier halides at a value similar to that of atomic $Ni^+(^2D)$, 1507 cm^{-1}. In contrast, the spin-orbit splitting of the $^2\Pi$ state is much smaller and increases monotonically across the series, reaching a maximum of $\sim$600 cm^{-1}.

As discussed by Zou and Liu,[106] the spin-orbit components of the $^2\Pi$ state correspond approximately to the ligand field splitting of the different m_j components of the $Ni^+(^2D_{5/2})$ state, and the splitting is then dependent on the ligand field. They explain the increased splitting across the monohalide series as reflecting variations in the mixing of ligand np orbitals. We note that the vibrational frequencies of the two spin-orbit components of the $^2\Delta$ state are similar; however, the frequency of the upper spin-orbit component of the $^2\Pi$ state is consistently smaller that the lower component, which reflects interactions with the higher lying $B^2\Sigma^+_{1/2}$ state. This interaction remains favorable across the series, as while the energy of both states increases for the heavier halides (Figure 4.1), the energy separation remains approximately constant.

In a recent article, Hougen has developed an approximate theoretical model for the five states of the Nickel monohalides considered here, and applied this to NiF and NiCl.[138] This model includes only spin-orbit and crystal-field parameters, with an empirical correction factor (denoted β) included for one off-diagonal matrix element in order to correctly treat the interaction of the two $\Omega=1/2$ states. We applied Hougen's model to the data sets for NiCl, NiBr, and NiI obtained in our laboratory, and the results are shown in Table 4.1 . The optimized value of β is ~0.9 for NiF and NiCl, and drops to ~0.8 for NiBr and NiI.
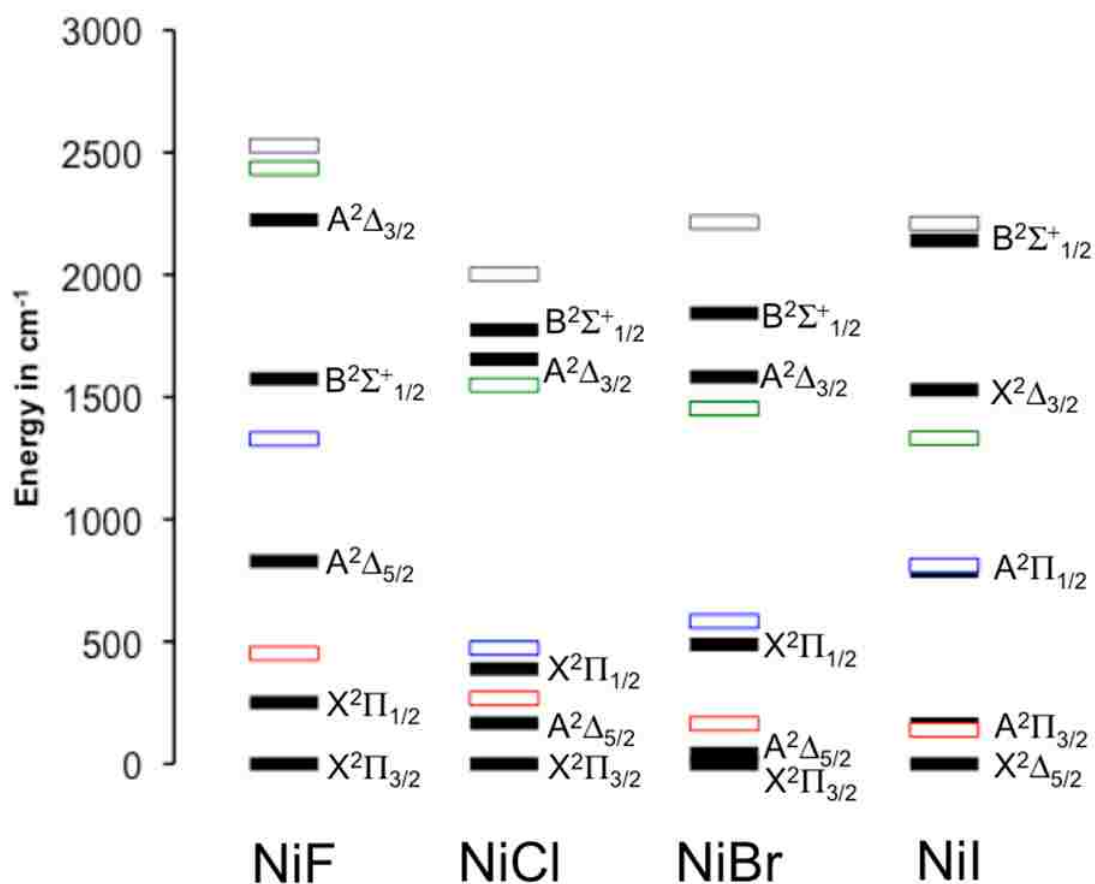
Figure 4.1 : Energy level diagram of the low-lying states of the Nickel monohalides that arise from the 3d9 configuration of Ni^+. The solid bar reflects experimental measurements from this work and references[40,91,95] .The open bars represent theoretical predictions from reference[33].
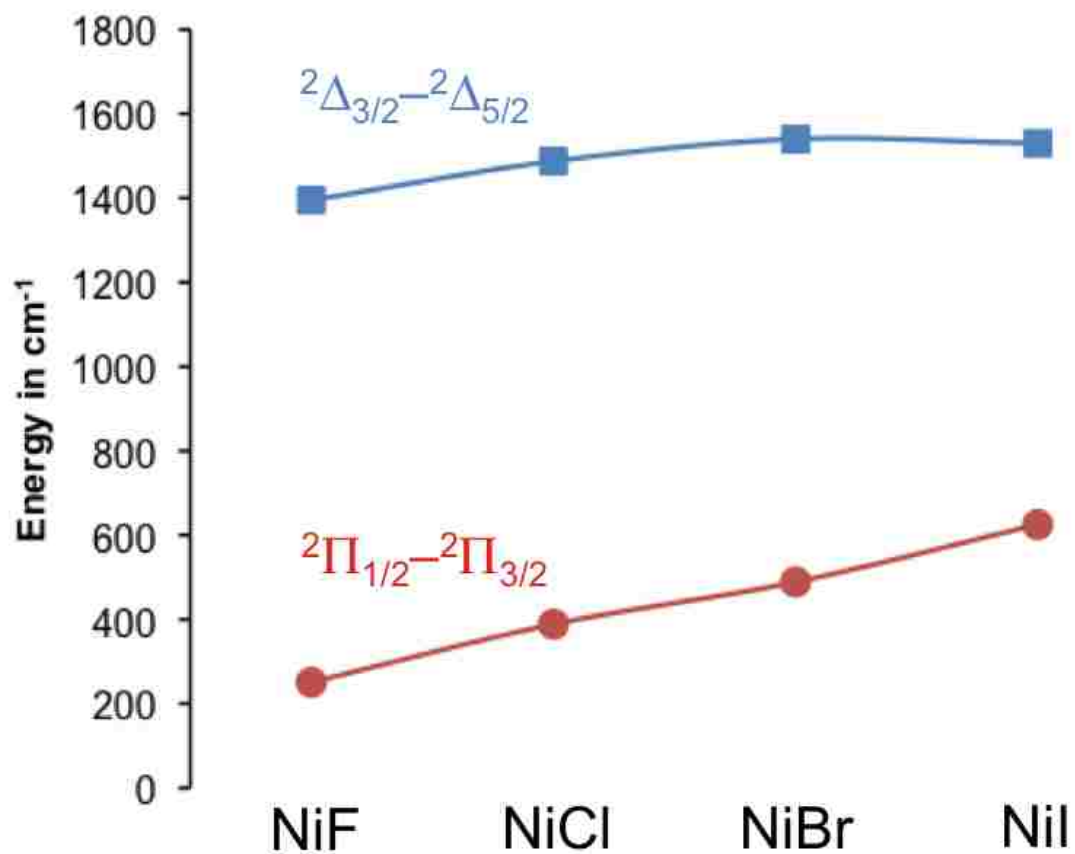
Figure 4.2: Spin-orbit splitting of the $^2\Delta$ and $^2\Pi$ states in the Nickel monohalides, from experiment. Data for NiF was taken from references[40,91,95].

Table 4.1: Fit parameters and residuals from a comparison of our experimental term energies for the low-lying Nickel monohalide spin-orbit states with the theoretical model of Hougen.[138]

NiI	State	T_0	(o-c)[a]	(o-c)[b]	(o-c)[c]	Parameters	(value)[a]	(value)[b]	(value)[c]
	$X^2\Delta_{5/2}$	0	0.5	-36.9	-11.3	A	-566.9	-602.8[d]	-602.8[d]
	$A^2\Pi_{3/2}$	162.7	82.0	65.4	-2.2	β	1.0[d]	1.0[d]	0.79
	$A^2\Pi_{1/2}$	787.8	-91.9	-120.9	-3.5	C_0	924	924	924
	$X^2\Delta_{3/2}$	1529.8	-34.0	25.2	15.9	C_2	-417	-412	-412
	$B^2\Sigma^+_{1/2}$	2140.2	43.4	67.3	1.1	C_4	243	214	317
NiBr	State	T_0	(o-c)[a]	(o-c)[b]	(o-c)[c]	Parameters	(value)[a]	(value)[b]	(value)[c]
	$X^2\Pi_{3/2}$	0	57.6	50.5	-17.3	A	-576.5	-602.8[d]	-602.8[d]
	$A^2\Delta_{5/2}$	43.3	17.7	-13.7	2.9	β	1.0[d]	1.0[d]	0.80
	$X^2\Pi_{1/2}$	488.9	-83.4	-104.6	22.4	C_0	783	783	783
	$A^2\Delta_{3/2}$	1537.7	-36.4	4.2	0.3	C_2	-209	-207	-213
	$B^2\Sigma^+_{1/2}$	1843.1	44.5	63.6	-8.4	C_4	254	228	319
NiCl	State	T_0	(o-c)[a]	(o-c)[b]	(o-c)[c]	Parameters	(value)[a]	(value)[b]	(value)[c]
	$X^2\Pi_{3/2}$	0	35.9	33.6	0.4	A	-587.3	-602.8[d]	-602.8[d]
	$A^2\Delta_{5/2}$	166.9	20.8	1.8	8.5	β	1.0[d]	1.0[d]	0.89
	$X^2\Pi_{1/2}$	388.52	-61.6	-75.0	2.8	C_0	797	797	797
	$A^2\Delta_{3/2}$	1654.37	-32.0	-9.0	-10.2	C_2	-85	-84	-88
	$B^2\Sigma^+_{1/2}$	1776.56	36.8	48.6	-1.4	C_4	250	233	276

[a] Model 1, where β was fixed at 1.0. [b] Model 2, where A was fixed to its value in the free Ni^+ ion and β was fixed at 1.0. [c] Model 3, where A was fixed to its value in the free Ni^+ ion and β was floated in the fit. [d] Fixed in the fit.

4.3. Variation of vibrational constants with halogen

The vibrational constant of nickel monohalides decreases down the periodic group. This is evident in Table 4.2 which shows the trend in experimental vibrational frequencies obtained in this work. Since the vibrational frequency (ω) is proportional to the square root of force constant over reduced mass (see Equation 7.1).

$$\omega = \sqrt{k/\mu} \qquad k = \text{force constant and } \mu = \text{reduced mass} \quad \text{(Equation 7.1)}$$

We see that the vibrational frequency decrease as we move down the periodic group (Fluorine to Iodine) due to increase in reduced mass. The fact that the vibrational frequencies decrease down the group indicates that the chemical bonding between the transition metal and the halogen weakens from Fluorine to Iodine. Indeed this is what is expected since $F^- > Cl^- > Br^- > I^-$ in the spectrochemical series.

The same trend can be seen in excited states vibrational frequencies were for NiI is ~ 215 cm^{-1} and NiBr ~ 296 cm^{-1}, the trend is expected to continue for NiCl and NiF as the vibrational frequencies increase up the periodic group as the bond lengths becomes shorter and stronger. The increase in bond length as we move down the periodic group can be seen in Table 4.3 for NiI and NiBr. With the observation of NiI, NiBr and NiCI, it is reasonable to expect that the vibrational frequency of NiF would be the largest for the members of the halides. This can be confirmed from theoretical and experimental results done on NiF [96,97,104,107,139,140] by other groups.

Table 4.2 : Ground state experimental vibrational constants in wavenumber (cm^{-1}) of the low-lying states of NiX.

NiI	ω_e	NiBr	ω_e	NiCl	ω_e
$B^2\Sigma^+_{1/2}$	268	$B^2\Sigma^+_{1/2}$	324	$B^2\Sigma^+_{1/2}$	425
$X^2\Delta_{3/2}$	277	$A^2\Delta_{3/2}$	326	$A^2\Delta_{3/2}$	433
$A^2\Pi_{1/2}$	260	$X^2\Pi_{1/2}$	307	$X^2\Pi_{1/2}$	404
$A^2\Pi_{3/2}$	273	$A^2\Delta_{5/2}$	326	$A^2\Delta_{5/2}$	435
$X^2\Delta_{5/2}$	278	$X^2\Pi_{3/2}$	320	$X^2\Pi_{3/2}$	427

4.4. Periodic variation in Bond lengths

From the simulations of the experimental bands, the B_0 rotational constants are 0.071 cm^{-1}, 0.069 cm^{-1} and 0.071 cm^{-1} for the $[21.1]^2\Pi_{3/2}$, $[21.3]^2\Delta_{5/2}$ and $[21.9]^2\Pi_{3/2}$ states, corresponding to (R_0) bond lengths of 2.43 Å, 2.46 Å and 2.42 Å respectively for NiI and the B_0 rotational constants are 0.101 cm^{-1}, 0.095 cm^{-1} and 0.098 cm^{-1} for the $[21.5]^2\Pi_{3/2}$, $[21.7]^2\Delta_{5/2}$ and $[22.3]^2\Pi_{3/2}$ states, corresponding to (R_0) bond lengths of 2.03 Å, 2.09 Å and 2.07 Å respectively for NiBr. The values can be summarized in Table 4.3 . The general trend is that the bond length increases from NiBr to NiI this can also be confirmed by the increase in the vibrational frequency as the bond length becomes shorter and stronger as we move up the period (Iodine to Fluorine). The same trend in the decrease in bond length is also expected for NiCl and NiF.

Table 4.3 : Experimentally derived rotational constants and calculated bond length for NiI and NiBr. Rotational constants were obtained from PGOPHER simulations.

NiI		NiBr	
B in cm^{-1}	Bond length in Å	B in cm^{-1}	Bond length in Å
0.071	2.432	0.101	2.039
0.0692	2.464	0.0959	2.093
0.0714	2.424	0.098	2.07

4.5. Perturbations in low–lying states of nickel monohalides

Recall from chapter 3, the interactions observed was between vibrational levels between electronic states of different symmetry, which is the interaction between the spin and the orbital angular momenta of the electron (spin-orbit homogeneous interaction). In general, interactions between electronic states with identical omega ($\Delta\Omega=0$) (if present) are weak in NiBr and NiCl as compared to NiI. This is due to the weakening of the spin-orbit interaction as we move from heavy atom (Iodine) to light atoms (bromine and chlorine) in the periodic table. The heavier the mass of the atom the greater the spin orbit interaction and the greater the spin-orbit perturbations.

4.6. Summary

Laser induced fluorescence and single vibronic level emission spectroscopy has been used to probe five low-lying electronic states ($X^2\Pi_{3/2}$, $A^2\Delta_{5/2}$, $X^2\Pi_{1/2}$, $A^2\Delta_{3/2}$ and $B^2\Sigma^+_{1/2}$) of NiI, NiBr and NiCl that arise from the $3d^9$ configuration of Ni^+. From the periodic trend analysis, several trends are apparent. From NiF-NiI, the splitting between the $^2\Pi_{3/2}$, and the $^2\Delta_{5/2}$ state decreases in the heavier halogens, with the ordering of states in NiI totally switched. In the case of the $^2\Delta$ state, the spin-orbit splitting increases in going from the fluoride to chloride, but is relatively constant for the heavier halides at a value.

In contrast, the spin-orbit splitting of the $^2\Pi$ state is much smaller and increases monotonically across the series. In contrast to NiI, the spectra of NiBr and NiCl show few vibronic perturbations, reflecting the smaller spin-orbit coupling in these systems as the halogen becomes lighter.

4.7. Future work

It would also be interesting to compare the trends for other series with other transition metals, i.e. we substitute different transition metals and keep the halogens fixed example CuX(X=Cl, Br, I). It would also be interesting to look into the polyatomic series of the transition metals for example NiOH, NiCN and so on.

Chapter 5.   THE RENNER-TELLER EFFECT IN CCN RADICAL: PULSED DISCHARGE-JET SINGLE VIBRONIC LEVEL EMISSION STUDIES

5.1. Introduction: Spectroscopy of CCN radical

The thin gaseous envelope that surrounds our planet is integral to the maintenance of life on earth. The composition of the atmosphere is predominately determined by biological processes acting in concert with physical and chemical change. Though the concentrations of the major atmospheric constituent's oxygen and nitrogen remain the same, the concentration of trace species which are key to many atmospheric processes are changing. It is becoming apparent that man's activities are beginning to change the composition of the atmosphere over a range of scales, leading to, for example increased acid deposition, local and regional ozone episodes, stratospheric ozone loss and potentially climate change. As a result it is very important to study species which has potential importance in our interstellar medium.

The CCN radical has attracted special interest in astrophysics and is important because a large number of linear carbon chain molecules have been observed in the interstellar medium.[141,142] For the nitrogen-bearing series, the CN_3, C_3N, and C_5N_4 radicals have been detected in interstellar clouds and in stellar envelopes, but CCN itself has not been observed to date.

The CN[143,144], C_2H[145-148] and some larger cyano radicals with an odd number of carbon atoms have also previously been detected in the interstellar medium.[149] The CCN radical should play an important role in reactions in the interstellar medium. As a proposed intermediate in the formation of larger cyano radicals, this molecule may provide important insights into the development of interstellar clouds and other areas of extraterrestrial interest, such as star-forming regions. Chemical interest in CCN is not limited to the interstellar medium, but CCN is also thought to be involved in combustion processes in fuel-rich natural gas flames.[150]

The CCN radical is one of the prototypical examples for triatomic molecules exhibiting the Renner-Teller (RT) effect, which originates from coupling between the vibrational and electronic angular momenta, and has been subject to extensive theoretical consideration.[151-157] The CCN radical was first observed in absorption by the flash photolysis of diazoacetonitrile, $HC(N_2)CN$, by Merer and Travis[158] in 1965. In this study the $A^2\Delta - X^2\Pi$, $B^2\Sigma^- - X^2\Pi$ and $C^2\Sigma^+ - X^2\Pi$ electronic transitions of this linear free radical were analyzed.[159-164] Using dye laser techniques, Kakimoto and Kasuya[165] obtained improved constants for the origin band of the $A^2\Delta - X^2\Pi$ system.

Microwave optical double resonances were observed in the excited $A^2\Delta$ state of CCN by Suzuki *et al.*[166] They were unable to observe ground-state microwave resonances because the dipole moment of the $X^2\Pi$ state is small.[167] Ground-state vibrational frequencies were obtained for the first time by Bondybey and English[168] in a matrix isolation experiment. More accurate values were determined by dispersing the $A^2\Delta - X^2\Pi$ laser-induced fluorescence with a small monochromator.[159,160]

More recently, this laser-induced fluorescence was studied at Doppler-limited resolution[162] with a Fourier transform spectrometer. Brazier *et al.*[162] obtained improved estimates for the Renner-Teller parameters and the ground-state vibrational frequencies. Several spectroscopic investigations have been carried out on CCN refining the spectroscopic constants of the electronic Π^2 ground state,[162-164,169-175] but limited hyperfine structure has been observed. Green[176] computed the molecular structure, hyperfine coupling constants and dipole moment of CCN in the ground electronic state.[176]

Recently in our lab, we have been interested in cyanomethylidyne (CCN). Its structures and spectra have been the subject of extensive attention both experimentally and theoretically.[169,170,176-185] The main motive of these studies is its potential importance in astrophysics, although the relevance of CCN in combustion processes had been suggested in 1989,[150] its chemical reactivity has been little studied until recently.[186,187] A theoretical investigation[187] also indicated that the CCN shows negligible barriers towards CH_4, featuring the carbene-insertion mechanism as CH does.[188] This result is of particular interest because usually non-atomic, non-hydrogenated radicals reacting with stable methane are subject to give noticeable barriers. This suggests that CCN may be a very reactive radical, and may play an important role in various fields such as combustion and interstellar chemistry. In particular, the formation of chemically homologous cyanopolyynes and their radicals have been studied comprehensively in the last years, theoretically and experimentally in astrochemical models.[189-202]

In this recent chapter we examined the spectroscopy of CCN radical using single vibronic level (SVL) emission and laser induced fluorescence (LIF) spectroscopy, following observation of band systems in the visible region. Vibrational parameters were determined for all levels observed. The harmonic frequencies derived from the SVL spectra was compared to the ab initio values.[184]

5.2. Experimental details

The apparatus, pulsed discharge nozzle and data acquisition procedures have been described in chapter 2 and our previous work.[22,23,42,54,62-64], and the experimental procedure is similar to that used in our recent work on NiI, NiBr and NiCl.[63,131] CCN was produced using a pulsed discharge source, using nickel alloy electrodes (Nickel alloy 625). For this study, CCN radical was generated by pulsed electric discharge through a mixture of CH_3CN (Sigma-Aldrich, 99+%) seeded in ~4 bar Ar (Airgas). The precursor was kept in a temperature controlled stainless steel bubbler, through which pure Ar gas was passed at a pressure of 2-4 bars. Discharge was initiated by a -1.0 kV pulse through a current limiting 42 kΩ ballast resistor. A pulse width of 200 μs was used initially, and was subsequently reduced to 50 μs to reduce interference from the discharge glow. The timing of laser, nozzle and discharge firing was controlled via an 8-channel pulse/digital delay generator (Berkeley Nucleonics).

Typical rotational temperature were ~ 50-90 K, as determined from simulations of the fluorescence excitation spectra, consistent with our previous study of NiX(X=I, Br, Cl)[62,63] and CuOH[55] using a similar source. Laser-induced fluorescence spectra were recorded in the 440-480 nm region using a Nd: YAG pumped tunable dye laser system (Continuum NY-61/Lambda Physik Scanmate 2E). The laser dyes Coumarin 480, Coumarin 460 and Coumarin 440 were used, giving typical pulse energies of ~4–5 mJ. Total fluorescence was filtered via long-pass and short-pass cutoff filters (Corion or Edmund Scientific) prior to detection by a photomultiplier tube detector (Oriel) held at − 980 V.

SVL emission spectra were obtained using a 0.3 m spectrograph (Action SR303i with ISTAR CCD) in photon counting mode. The typical slit width was 100-160 μm, and spectra were typically integrated over 15,000-20,000 laser shots. Spectral calibration was achieved using a neon hollow cathode lamp (Photron). The majority of the spectra recorded were collected using a lower resolution (600 l/mm) grating; however, some spectra were also collected with a higher resolution (1800 l/mm) grating in order to separate closely spaced transitions. Bands in the emission spectra were fit to a Gaussian line shape function using a nonlinear least squares fitting routine in Origin 7.5 software; the uncertainty in the derived band positions is ± 2 cm^{-1}.

5.3. Spectral analysis of CCN radical

5.3.1. LIF and SVL spectroscopy of the CCN radical

Our group reported laser induced fluorescence spectrum of the CCN radical in the region near 20 800 – 22 700 cm^{-1}. The lower trace of Figure 5.1 shows a low resolution fluorescence excitation spectrum for CCN, recorded in the range 20 800 – 21 600 cm^{-1} which includes emission from all the excited state bands observed in this work. Also shown in upper trace of Figure 5.1 is the high resolution LIF spectrum of the excited vibronic transition. The rotational components were fully resolved with two sets of P, Q and R braches observed in the spectrum. Each branch reveals a doublet structure with a separation of about 40 cm^{-1}, which corresponds to the spin-orbit splitting of the $X^2\Pi$ state.[158,161,170]

Rotational simulations using the PGOPHER program[124] were performed for the most intense features for the excited state bands observed herein. In all cases, the most successful replication of the experimentally observed rotational contour was achieved with a rotational temperature of 50-90 K consistent with our previous study of NiX(X=I, Br, Cl)[62,63] and CuOH[55] using a similar source. Figure 5.2 displays a representative of the experimental (top half) and simulated (bottom half) high resolution LIF spectrum of the origin of the $X^2\Pi_{1/2}$ - $A^2\Pi_{1/2}$ transition. The simulations also further confirm the assignments of the excited state symmetries.
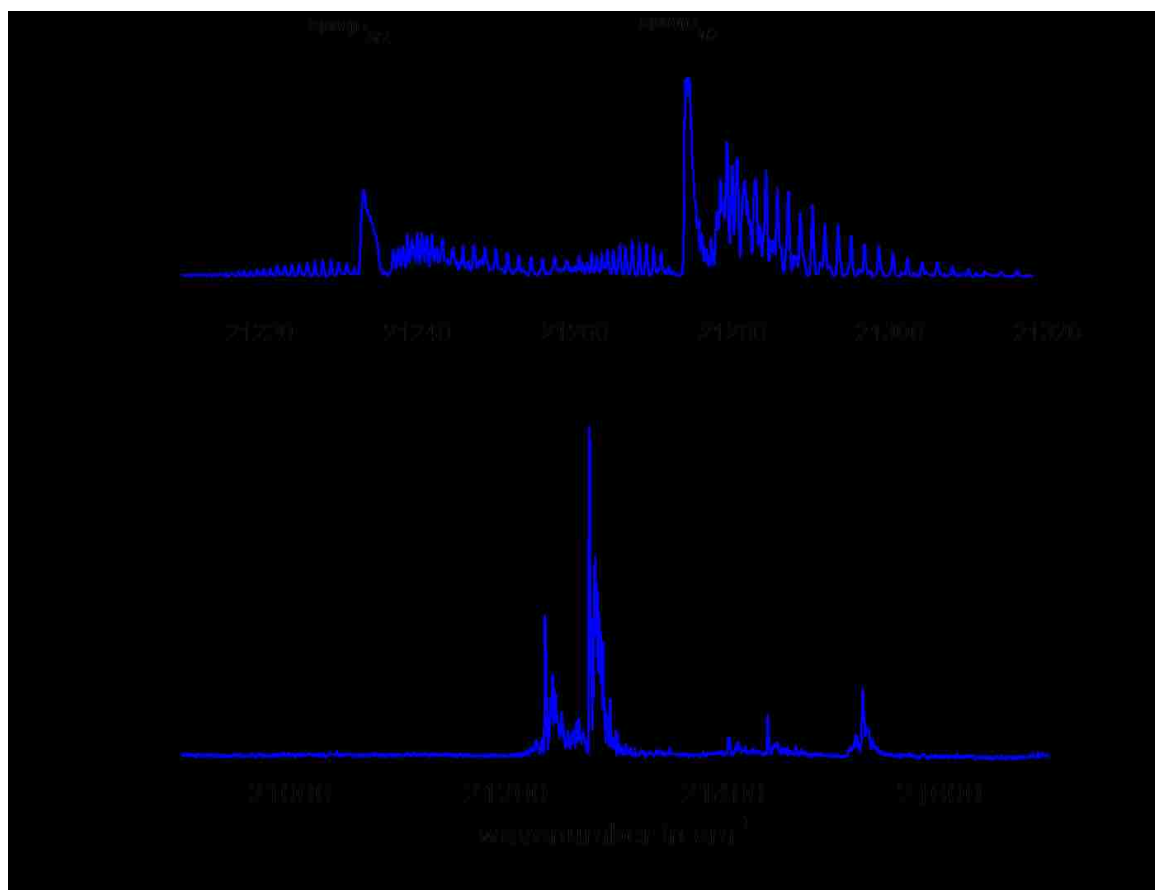
Figure 5.1: Laser induced fluorescence (LIF) spectrum of CCN using low resolution (0.01 nm step size) (lower trace) and high resolution (0.002 nm step size) (upper trace).
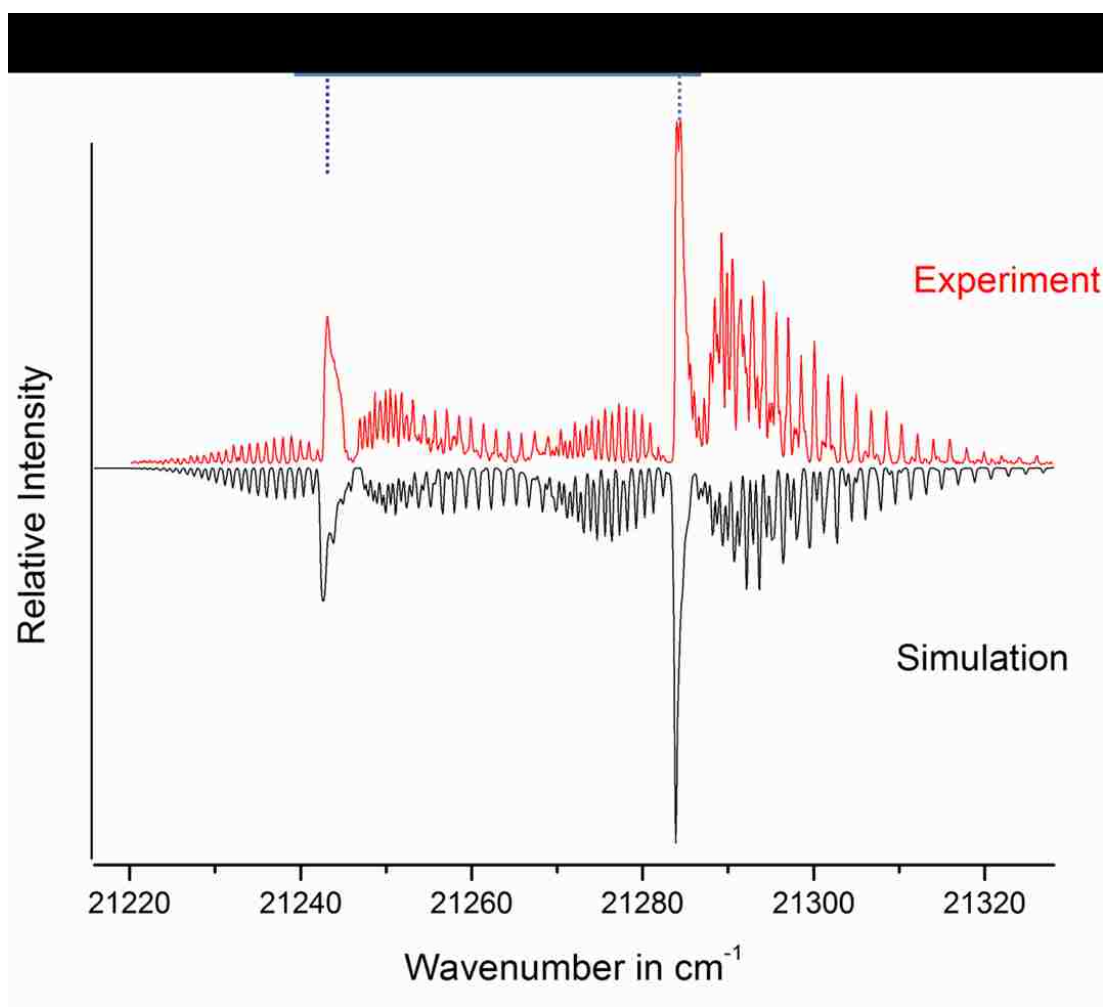
Figure 5.2: Comparison of the experimental (upper trace) and simulated (lower trace) for the origin band of CCN. Rotational temperature is approximately 50K.

Following our observation of the bands in this system, we obtained a series of SVL emission spectra. The SVL emission spectra were recorded via several bands observed in the LIF spectrum. An example SVL emission spectrum obtained with our low resolution (600 l/mm) grating and following excitation of the $^2\Pi$ band at 21 284 cm^{-1} is shown in Figure 5.3 . Due to the very small splitting of the $X^2\Pi$ states, resolving these features in the emission spectrum required the use of a higher resolution (1800 l/mm) grating, and a spectrum obtained under higher resolution is shown in the upper panel of Figure 5.4 . The emission spectra was found to contain the (0,0,0) –(0,0,n) and (0,0,0) – (1,0,n) vibronic bands (Figure 5.4) of the $^2\Pi$ –X $^2\Pi$ transition of CCN. Additional features could be assigned to the Swan band system of C_2 and numerous high vibrational excited bands of CN.[203,204] The line positions were assigned with the help of the Renner-Teller program RT3 and the line positions agree within experimental error. Transitions involving n quanta (see Figure 5.4) were observed and from this ω_1 = 1047.2 and x_{11} = -2.04 may be derived in Table 5.1.
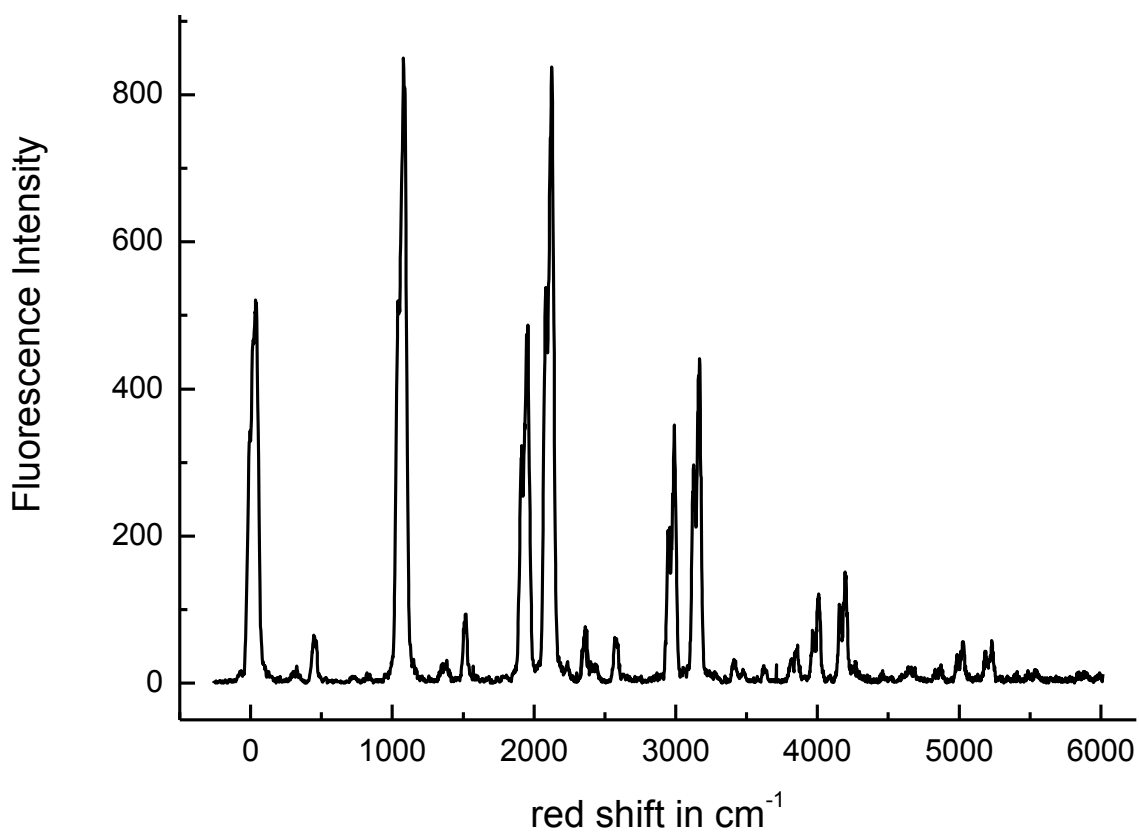
Figure 5.3: SVL spectrum of CCN recorded via the X(0,0,0) $\Pi_{1/2}$ at 21 284 cm^{-1} using a 600 l/mm grating. Assignments are shown in the high resolution spectra in Figure 5.4.
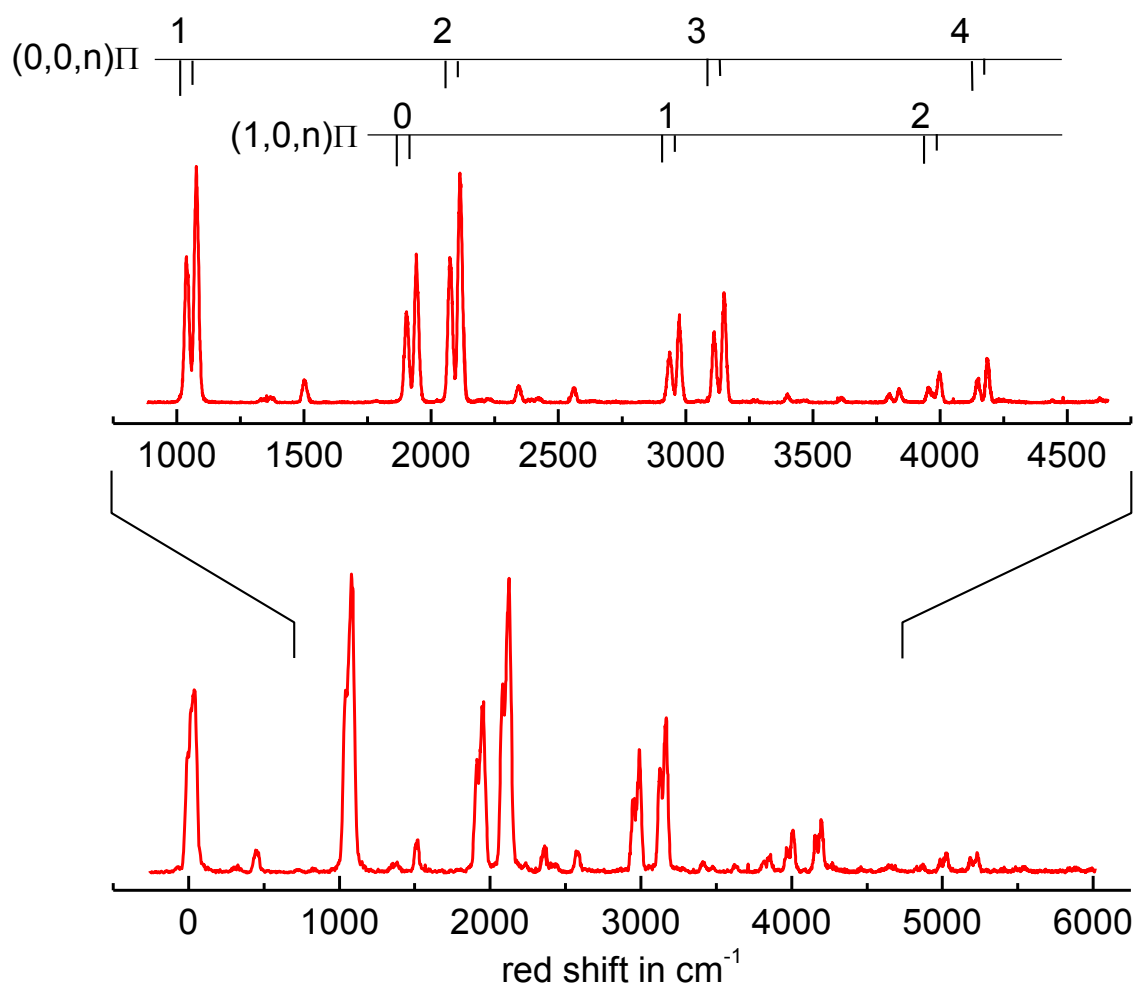
Figure 5.4: SVL spectrum of CCN recorded via the X(0,0,0) $\Pi_{1/2}$ at 21 284 cm^{-1} using a 600 l/mm grating (lower trace) and an 1800 l/mm grating (upper trace).

The calibrated SVL emission spectra peak energies were fit using the RT3 program and the observed vibronic transitions was used to derive vibrational and Renner-Teller parameters for CCN radical. The derived molecular constants are given in Table 5.1 . Note that the observed vibrational frequencies and constants are consistent with those of previous experimental studies[162,163,170] and recent theoretical study by Hill et al[184] ; however the difference being in that work only transitions to 2578 cm^{-1} could be identified.

The vibronic assignments for all the levels observed in this work are given in Table 5.2 . These assignments are based on the subsequent high-resolution analysis by the RT3 program. Included also in Table 5.2 are the term energies and fit residuals (in cm^{-1}) for the states assigned for CCN radical. Note that our work observes additional levels up to 5885 cm^{-1} as compared to previous work. Table 5.3 shows the comparison of our experimentally derived parameters (term energies, fit residuals and calculated Mean Square Difference (MSD) to the calculated theoretical parameters of Hill *et al*[184]. Overall there is a good agreement; however there is a significant improvement in our experimentally derived Mean Square Difference of 3.18 cm^{-1} as compared to calculated 14.58 cm^{-1}. The LIF and SVL of the CCN radical has revealed the vibronic energy levels of the ground and excited state $^2\Pi$ and has yielded the vibrational and the vibronic parameters.

Table 5.1: Summary of vibrational, Renner-Teller, and spin-orbit parameters (in cm^{-1}) for $X^2\Pi$ state of CCN radical observed in the present work.

Constant	Value in cm^{-1}	Error
ω_1	1047.29	1.55
ω_2	301.18	2.70
ω_3	1925.17	3.16
EW	135.49	0.66
GK	2.60	1.98
A	-42.72	1.81
G4	0.56	0.31
x_{11}	-2.04	0.39
x_{12}	4.66	0.47
x_{13}	-16.06	1.03
x_{23}	-4.14	0.90
x_{33}	-8.97	1.51

Table 5.2: Term energies and fit residuals (in cm^{-1}) for the states assigned for CCN radical.

Vibronic state	Obs	Cal	Obs-Cal (cm^{-1})
κ(0,0,0)Π	38.6	40.2	-1.6
μ(0,1,0)Σ	179.6	183.6	-4.3
κ (0,1,0) Σ	467.5	461.0	6.5
κ (0,2,0) Φ	573.8	573.2	0.6
μ (1,0,0) Π	1051.4	1045.5	5.9
κ (1,0,0) Π	1089	1085.8	3.2
κ (0,3,0) Σ	1238.6	1234.9	3.7
μ (1,1,0) Σ	1238.6	1233.8	4.8
κ (1,1,0) Σ	1514.3	1511.1	3.2
μ (1,3,0) Σ	1746.3	1754.0	-7.7
μ (0,0,1) Π	1915.3	1916.0	-0.7
κ (0,0,1) Π	1954.2	1956.1	-1.9
μ (2,0,0) Π	2086.6	2086.9	-0.3
μ (0,1,1) Σ	2098.9	2095.4	3.5
κ (2,0,0) Π	2125.7	2127.3	-1.6
κ (1,3,0) Σ	2295.5	2293.9	1.6
κ (0,1,1) Σ	2375	2372.9	2.1
κ (2,1,0) Σ	2556.8	2557.1	-0.3

Continuation Table 8.2			
Vibronic state	Obs	Cal	Obs-Cal (cm^{-1})
μ (2,3,0) Σ	2810.2	2808.8	1.4
μ (1,0,1) Π	2949.1	2945.4	3.7
κ (1,0,1) Π	2987.1	2985.7	1.4
μ (3,0,0) Π	3124.2	3124.3	-0.1
κ (0,3,1) Σ	3144.3	3138.8	5.5
κ (3,0,0) Π	3163.2	3164.7	-1.5
κ (2,3,0) Σ	3342.2	3348.9	-6.7
κ (1,1,1) Σ	3411.3	3406.9	4.4
κ (3,1,0) Σ	3595.8	3599.0	-3.2
μ (1,3,1) Σ	3636.5	3642.0	-5.5
μ (0,0,2) Π	3811.8	3814.0	-2.2
κ (0,0,2) Π	3851.3	3854.0	-2.7
μ (3,3,0) Σ	3869.1	3859.6	9.5
μ (2,0,1) Π	3970.2	3970.8	-0.6
μ (0,1,2) Σ	3989.2	3989.2	0.0
κ (2,0,1) Π	4009.8	4011.1	-1.3
μ (4,0,0) Π	4159.9	4157.5	2.4

Continuation Table 8.2			
Vibronic state	Obs	Cal	Obs-Cal (cm^{-1})
κ (1,3,1) Σ	4177.9	4181.8	-3.9
κ (4,0,0) Π	4198.7	4198.1	0.6
κ (0,1,2) Σ	4262.9	4266.8	-3.9
κ (2,1,1) Σ	4437.1	4436.9	0.3
κ (4,1,0) Σ	4631.8	4636.8	-5.0
μ (1,0,2) Π	4829.7	4827.4	2.3
κ (1,0,2) Π	4870.1	4867.5	2.6
μ (3,0,1) Π	4985	4992.1	-7.1
κ (3,0,1) Π	5025.3	5032.5	-7.2
κ (0,3,2) Σ	5026.2	5024.8	1.4
μ (5,0,0) Π	5188.9	5186.7	2.2
κ (5,0,0) Π	5231	5227.3	3.7
μ (2,0,2) Π	5838.1	5836.7	1.4
κ (2,0,2) Π	5885.4	5877.0	8.4

Table 5.3: Term energies and fit residuals (in cm^{-1}) for the states assigned for CCN radical in this work compared to the work of Hill *et al* [184]. Included also are the respective calculated Mean Square Difference (MSD).

Vibronic state	Obs (This work)	Cal (RT3)	Obs-Cal	Cal (Hill *et al*)[184]	Obs-Cal
κ(0,0,0)Π	38.6	40.2	-1.6	38.90	-0.3
μ(0,1,0)Σ	179.6	183.6	-4.3	201.00	-21.4
κ (0,1,0) Σ	467.5	461.0	6.5	478.80	-11.3
κ (0,2,0) Φ	573.8	573.2	0.6	580.30	-6.50
μ (1,0,0) Π	1051.4	1045.5	5.9	1052.00	-0.6
κ (1,0,0) Π	1089	1085.8	3.2	1090.92	-1.92
κ (0,3,0) Σ	1238.6	1234.9	3.7	1236.63	1.97
μ (1,1,0) Σ	1238.6	1233.8	4.8	1263.58	-24.98
κ (1,1,0) Σ	1514.3	1511.1	3.2	1583.30	-69
μ (1,3,0) Σ	1746.3	1754.0	-7.7	1767.10	-20.8
μ (0,0,1) Π	1915.3	1916.0	-0.7	1924.90	-9.6
κ (0,0,1) Π	1954.2	1956.1	-1.9	1963.60	-9.4
μ (2,0,0) Π	2086.6	2086.9	-0.3	2097.44	-10.84
μ (0,1,1) Σ	2098.9	2095.4	3.5	2117.50	-18.6
κ (2,0,0) Π	2125.7	2127.3	-1.6	2136.03	-10.33
κ (1,3,0) Σ	2295.5	2293.9	1.6	2298.70	-3.2
κ (0,1,1) Σ	2375	2372.9	2.1	2395.32	-20.32
κ (2,1,0) Σ	2556.8	2557.1	-0.3	2578.10	-21.3
.	.	.	.		
.	.	.	.		
κ (2,0,2) Π	5885.4	5877.0	8.4		
*MSD			**3.18**		**14.58**

*Mean Square Difference (MSD)

5.4. Summary

Building upon previous studies of CCN radical, we report further high resolution LIF and SVL emission spectra of CCN radical. The derived harmonic frequencies, term energies and Renner Teller constants are in good agreement with previous experimental and theoretical work. New additional levels for CCN radical were observed in our recent work and they provide an improved fit using the RT3 program. The fit levels results in an improved Mean Square Difference of $\sim 3.1 \text{cm}^{-1}$. CCN excited state bands for the origin of $X^2\Pi_{1/2}$ - $A^2\Pi_{1/2}$ transition were successfully assigned and simulated using the PGOPHER program.

Chapter 6.   **RESONANT TWO-PHOTON IONIZATION STUDIES OF CHLOROBENZENE CLUSTERS**

6.1. Introduction to Non Covalent Interactions

6.1.1. Halogen bonding

Although halogens are involved in other types of bonding (e.g. covalent), halogen bonding specifically refers to when the halogen acts as an electrophilic (electron loving) species. In halogen bonding, a halogen atom is the electron acceptor. Halogens participating in halogen bonding include: iodine (I), bromine (Br), chlorine (Cl), following the general trend: $F < Cl < Br < I$, with iodine normally forming the strongest interactions.[205] The interactions can be understood in terms of electrostatics/polarization and dispersion; they involve a region of positive electrostatic potential on a covalently bonded halogen and a negative site, such as the lone pair of a Lewis base.

The positive potential, labeled a σ hole, is on the extension of the covalent bond to the halogen, which accounts for the characteristic near-linearity of halogen bonding.[206,207] Different types of halogen bonding interactions relevant to this study are illustrated in Figure 6.2 . Halogen bonds are strong, specific, and directional interactions that give rise to well-defined structures.

6.1.2.   π-π Interactions (stacking)

π-stacking (also called π-π stacking/aromatic-aromatic interactions) refers to attractive, noncovalent interactions between aromatic rings.[208] This class of interaction involves direct attraction between the arene rings. The main energetic contribution to these interactions are Van Der Waals dispersion and electrostatics but there is considerable debate about which is dominant.[208-211] These interactions are important in nucleobase stacking within DNA and RNA molecules (see Figure 6.1), protein folding, template-directed synthesis, materials science, and molecular recognition;[209,212-215] although new research suggests that π-stacking may not be operative in some of these applications. Despite intense experimental and theoretical interest, there is no unified description of the factors that contribute to π-stacking interactions. Although the importance of $\pi - \pi$ interactions is widely recognized, a detailed understanding of their origins, strength, and orientation dependence is not fully understood.[208]
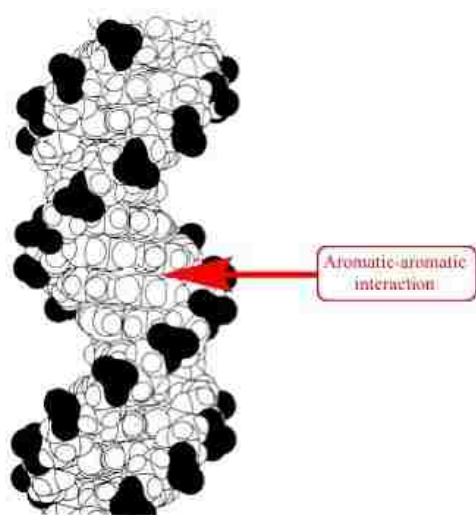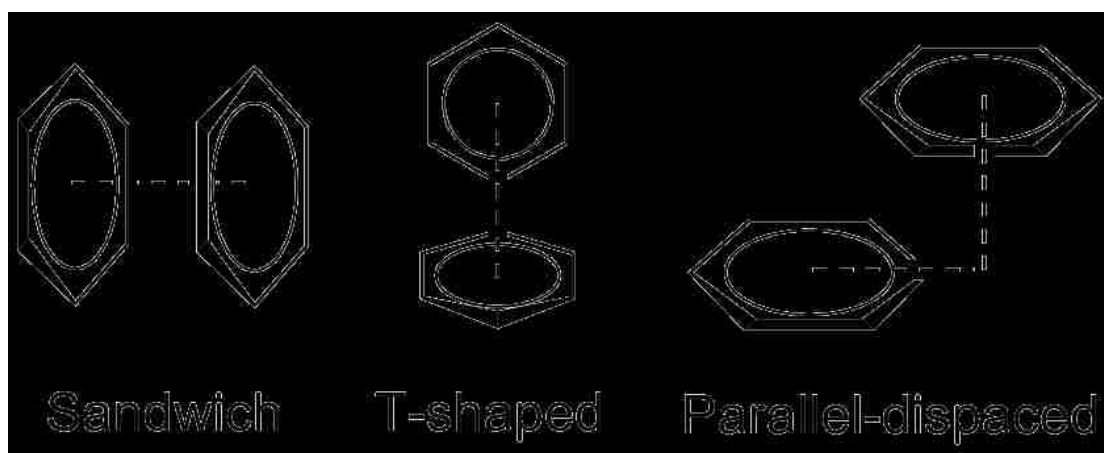
Figure 6.1: Schematic representation of different noncovalent interactions which can occur between aromatic rings. Taken from reference [208] Lower figure is shows example of aromatic-aromatic interactions in DNA. Lower trace picture taken from Wikipedia.

6.1.3. CH/π interactions

The CH/π interaction is one of the weakest of the so-called weak molecular interactions.[216,217] The term "CH/π interaction" which has recently gained attention in the consideration of a variety of molecular phenomena is the weakest among the hydrogen bonds, but has been found in a variety of substances to play important roles in their physical, chemical and biological properties.[218] The term CH/π interaction has been accepted because of its usefulness in describing the interaction between CH groups and π-systems, which is considerably stronger than expected from a mere dispersion mechanism. Attractive interactions operating between CH/π in such cases could be understood as a combined effect of known interaction forces, (Coulombic, charge transfer, dispersion, so-called "hydrophobic", etc.), and may most appropriately be termed as CH/π interaction.[218]. The schematic of different types of non-covalent interactions, including the CH/π interaction, is shown in Figure 6.2 .
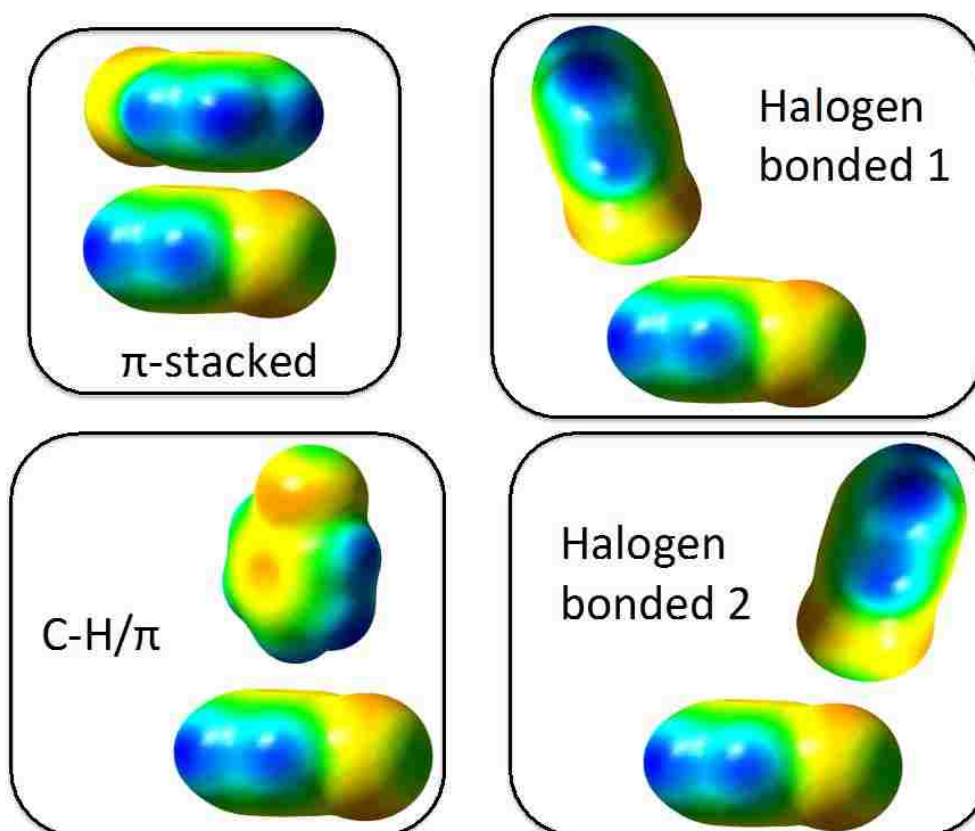
Figure 6.2: Schematic of possible non-covalent interactions in halobenzene dimers. The electrostatic potential surface of chlorobenzene calculated at the M06-2x/aug-cc-pVDZ level is shown.

6.2. The Duschinsky Effect

When a molecule undergoes an electronic transition, the change in electronic state is usually accompanied by a change in the normal modes of vibration. This phenomenon was first considered in 1937 by Duschinsky,[219] and is therefore given the name the Duschinsky effect. The result is that normal modes of one state are no longer orthogonal to the normal modes of the other state. A result is that the overlap integrals of the vibrational wave functions, or Franck-Condon factors (FCF), are no longer separable into products of one-dimensional FCF calculations, and one must use multidimensional FCF. Sando *et al* [220]showed that the additional complexity of multidimensional FCF can lead to large effects on electron-transfer rates. Therefore, a treatment of the Duschinsky effect is required that demonstrates how to compute the Duschinsky effect for complex molecules.

6.3. Introduction: Chlorobenzene Clusters

Noncovalent interactions of various types, such as hydrogen bonding, π-π stacking, CH/π interactions, and halogen bonding play a key role in influencing chemical reactivity and molecular structure,[221-230] in molecular recognition and binding,[231-236] and in the structure, stability and dynamic properties of biomolecules.[237-242] Noncovalent forces are critical in determining the secondary, tertiary or quaternary structure of large molecules, and thus their macromolecular function.[212,239,240,242-244] Understanding the relative magnitude of these various types of interactions is important, particularly as they may exist in cooperation or competition,[243,245-248] and this has been the target of intense experimental and theoretical effort.[209,211,214,237,249-258] In this regard, mono-substituted halobenzene clusters are prototypical systems in which different noncovalent interactions may be operative, including π-π stacking,[209,214,257,259-266] CH/π,[238,257,267] and halogen bonding interactions, illustrated in Figure 6.2.[223,235,267-274]

Simple aromatic dimers involving benzene and toluene have long been proposed as model systems for understanding π-π stacking interactions in proteins,[212,275] and are also prototypes for exploring the relative importance of π-π stacking and CH/π interactions.[241] The story of the benzene dimer, in particular, is one of controversy and intense debate, with respect to the relative energies of parallel (π–stacked) and T-shaped (CH/π) structures. [43,44]

State-of-the-art single reference [CCSD(T)/CBS] calculations by Sherrill and co-workers show that parallel displaced and T-shaped structures are nearly isoenergetic, with the symmetric sandwich structure lying 1 kcal/mol higher in energy.[211]

Experimental studies of aromatic homo- and heteroclusters have exploited a range of techniques, with mass-selected resonance ionization methods at the forefront. Thus, Bernstein and co-workers and Musgrave reported the first Resonant Two-photon Ionization (R2PI) spectra for toluene dimer through the S_1 state, which showed two features that were significantly broadened with respect to the monomer absorption.[249,250,276] These two features were attributed to different isomers, and the presence of at least two different isomers was confirmed in subsequent two-color hole-burning spectra.[277] Similar studies using R2PI and Zero-Kinetic Energy (ZEKE) spectroscopy have been reported on the substituted benzene dimers, including dimers of fluorobenzene,[215,278-284] chlorobenzene,[274,285] phenol, aniline[286-289] and others.[211,290] In addition, complexes of benzene derivatives and noble gas atoms have extensively studied both experimentally and theoretically.[291-297]

Building upon the seminal studies of Bernstein and others, Wright and co-workers recently reported R2PI spectra of mass-selected toluene homoclusters $(\text{Tol})_n$ up to $n=8$.[276] The striking result of this work was that the spectra of the higher order clusters were very similar to that of the dimer. While this might be explained by the cracking of higher order clusters, the authors proposed a model by which the favored (π–stacked) binding motif of the dimer formed the core of higher order clusters, leading to a "dimer chromophore" that was responsible for the electronic spectrum of higher order clusters. This explanation was apparently supported by subsequent measurements of the ionization

potential of mass-selected toluene clusters in a molecular beam.[275] Here a reduction in the ionization potential of the dimer relative to the monomer was found, consistent with the participation of a π–stacked dimer where the cationic charge could be delocalized over both rings. Relative to the dimer, the ionization potential of the trimer and tetramer did not change, which was taken as evidence against the existence of fully π–stacked clusters in the beam.

The S_0–S_1 spectroscopy and dissociation of halobenzenes has been extensively studied by R2PI and related methods;[298-303] however, relatively few R2PI spectroscopic studies of clusters of mono-substituted benzenes have been reported.[215,278-285] Chlorinated aromatic compounds are important pollutants,[304] however, the nature of intermolecular interactions in chlorobenzene clusters are still unclear.[274] Lu and coworkers conducted a study of chlorobenzene and chlorobenzene-benzene complexes by R2PI in a reflectron time–of–flight (TOF) mass spectrometer.[285] For the chlorobenzene dimer, in the region of the S_0 –S_1 ($\pi\pi^*$) origin two distinct and, in comparison to the monomer absorptions, very broad features were observed; one blue-shifted relative to the monomer absorption and the other red-shifted. The red-shifted absorption was assigned to a T-shaped dimer, and the blue-shifted absorption to a parallel-displaced (π-stacked) dimer. Support for the assignment of these absorptions to distinct species was provided in the carrier gas and backing pressure dependence of the relative intensities. In particular, it was found that the blue–shifted absorption increased in intensity when using Ar rather than He as the carrier gas, and at higher backing pressures. The binding energy of the chlorobenzene dimer was determined to be 14.4 ± 1.0 kJ/mol.[285]

The chlorobenzene clusters $(Clbz)_n$ with $n=2$-4 have recently been studied using ultrafast spectroscopy in a supersonic beam.[274] Following excitation of the $S_1(\pi\text{-}\pi^*)$ states at 267 nm, the decay dynamics of the clusters was found to exhibit multiple timescales, reflecting in part cracking of higher order clusters into the measured channel. However, an intrinsic exponential decay was found for all clusters. The fast (~170 fs) component was found to decrease with cluster size, and was attributed to internal conversion to the S_0 state. In contrast, the slow component (~ 1 ns), which was attributed to dissociation of the hot S_0 molecules, increased with cluster size, which was explained from a density of states argument.

This chapter highlights the study of competitive non-covalent forces in chlorobenzene clusters, using R2PI spectroscopy in concert with electronic structure calculations using Density Functional Theory (DFT) and post-Hartree Fock (MP2) methods in concert with correlation consistent basis sets. Motivating this work is the desire to understand the nature of the competitive non-covalent interactions in the monohalobenzenes, which in comparison to benzene or toluene includes also the potential for halogen bonding interactions between the σ-hole of a halogen on one fragment and the halogen or π-system on the other (see Figure 6.2).

6.4. Generation and detection of halobenzene ions using R2PI and R2C2PI technique

Ionization was initiated by a Resonance Two Photon Ionization (R2PI) scheme, with laser light near 267 nm generated from frequency doubling in a BBO crystal the output of a dye laser (Lambda-Physik, Scanmate 2E), and pumped by the third harmonic of an Nd: YAG laser (Continuum NY-61). The laser was operated on a C540A dye, giving typical output pulse energies of ~ 0.5 mJ in the doubled beam, which was loosely focused with a 1.0 m plano-convex lens into the chamber. In some experiments, Resonant Two-Color Two-Photon Ionization (R2C2PI) was employed, with the 266 nm output of a second Nd: YAG system (Continuum Minilite II) introduced as the ionization laser. In these experiments, the focusing lens in the doubled dye beam path was removed to reduce the contribution from R2PI signal, and the ionization laser was loosely focused with a 0.5 m lens. The delay between the lasers and molecular beam was controlled by an eight–channel digital delay generator (BNC 565).

Ions were extracted and accelerated using a conventional three-plate stack, with the repeller plate typically held at 2100 V, the extractor plate at 1950 V, and the third plate at ground potential. The ions traversed a path of 1 m prior to striking a dual chevron Microchannel Plate (MCP) detector. The detector signal was amplified (x 25) using a fast preamplifier (Stanford Research SRS445A), and integrated using a boxcar system (Stanford Research SRS250) interfaced to a personal computer.

An in-house LABVIEW program controlled data acquisition and stepped the laser wavelength; typically, the signal from twenty laser shots was averaged at each step in wavelength.

6.5. Computational Details for Chlorobenzene clusters work.

To support our experimental findings, electronic structure calculations were performed using the GAUSSIAN 09 software package on the MU Pere cluster.[305] Full geometry optimizations were carried out using DFT (M06-2x)[74] and post-Hartree Fock (MP2) methods using an aug-cc-pVDZ basis set. Our choice of method was dictated in part by the extensive computational studies, notably those of Sherrill and co-workers, on related systems,[211,237,252] where the performance of DFT methods in combination with various correlation consistent basis sets has been extensively benchmarked against high level post–Hartree Fock *ab initio* single reference methods.

It was shown that the Minnesota meta-GGA (Generalized Gradient Approximation) hybrid functional M06–2x, among other methods, provides a good cost to performance ratio,[252] and the aug-cc-pVDZ basis set performs well in calculating the counterpoise correction.[252] Zhao and Truhlar have shown that M06-2x performs well in describing the energies of π-stacking interactions.[74] In this work, our calculated binding energies were corrected for zero point energy (ZPE), and the counterpoise method was employed to correct for basis set superposition error (BSSE).

Time-dependent DFT (TDDFT) methods are quite popular for modeling electronically excited states, and it is well appreciated that local exchange functionals perform poorly for states involving significant charge transfer.[306] Thus, in this work we employed TDDFT methods using range-separated hybrid and meta-GGA hybrid functionals to calculate the electronic spectra of the clusters and the optimized geometry of the S_1 states. Methods employed included the range-separated hybrid functional ωB97X-D,[307] the meta-GGA hybrid functionals M06 and M06-2x,[74] and CAM-B3LYP,[308,309] all with an aug-cc-pVDZ basis set. The performance of the ωB97X-D and M06-2x methods for electronic excitations, including Rydberg and Charge Transfer excitations, have recently been benchmarked by Head-Gordon and co-workers.[310]

Spectral Analysis:

6.6. R2PI Spectral Analysis for Chlorobenzene clusters

Representative R2PI spectra of the chlorobenzene monomer and chlorobenzene clusters (Clbz)$_n$ with $n=2$–4 in the region of the origin band of the monomer S_0 –S_1 ($\pi\pi^*$) transition are displayed in Figure 6.3 . The electronic spectroscopy of the chlorobenzene monomer is well known and has been extensively studied previously by other groups using both R2PI and Laser Induced Fluorescence (LIF) spectroscopy.[285,304,311-317]

Note also that the size range of clusters that we observe is similar to that found in the prior ultrafast experiments, where a similar source was used.[274] From Figure 6.3, it is apparent that the clusters uniformly exhibit much broader absorption features than the monomer, yet the spectra of different clusters in the range $n=2$–4 are similar. The spectra for the clusters show a maximum absorption at lower energy (i.e., are red-shifted) with respect to the monomer peak. As noted in the introduction, the broad absorption features that we observe here for the clusters of chlorobenzene have previously been observed for related systems, including toluene dimer, fluorobenzene dimer and mixed halobenzene–benzene dimers.[249,250,285,290]
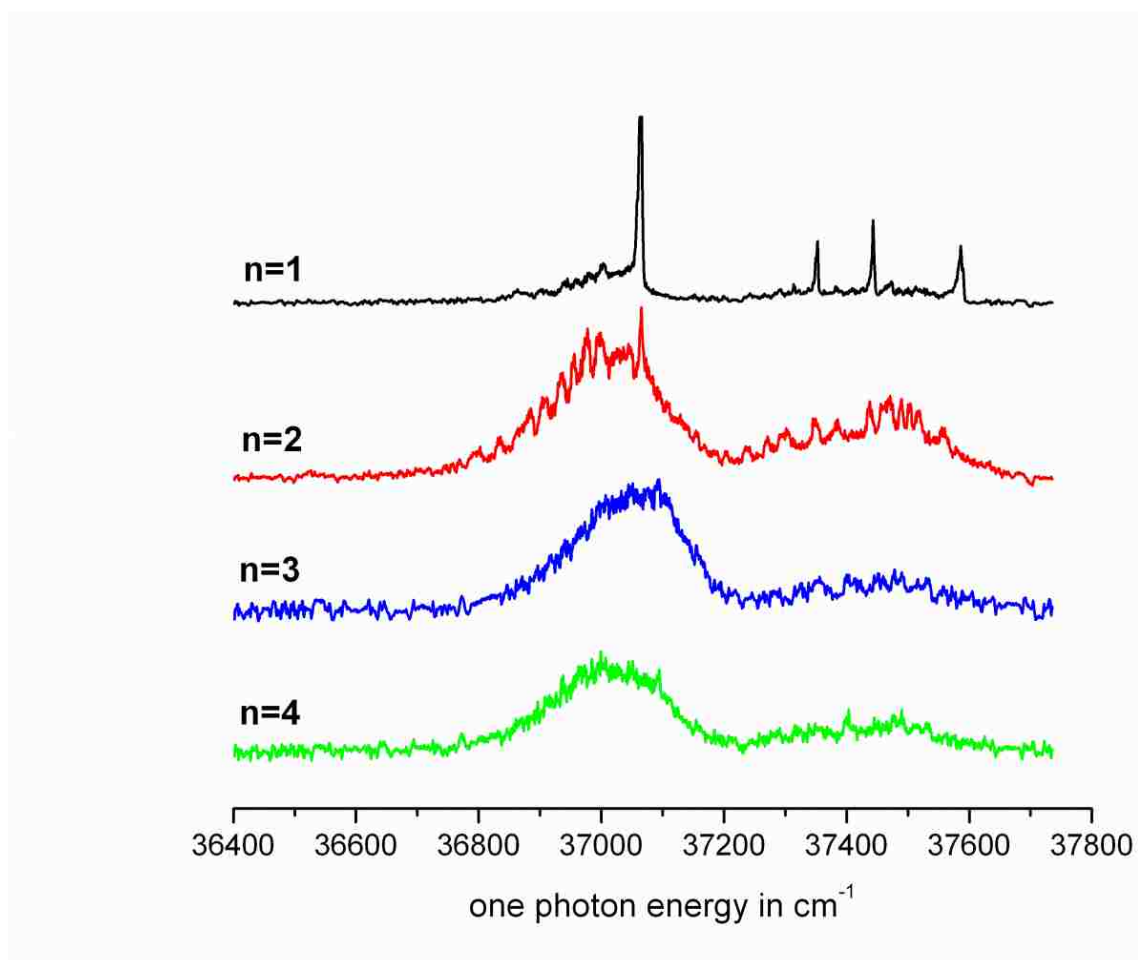
Figure 6.3 : Resonant Two-Photon Ionization (R2PI) spectra of mass-selected chlorobenzene monomer and clusters (Clbz)$_n$ with n=2-4.

We consider several explanations for the source of this broadening. An obvious explanation for the similarity of the cluster spectra is cracking of larger clusters, giving rise to signals in the mass channels of smaller clusters. Indeed, some cracking is clearly apparent in the monomer spectrum shown in Figure 6.3, as a weak broad background underlying the strong sharp features of the monomer. Expanding this spectrum and overlaying with the dimer spectrum shows strong similarities (Figure 6.4), indicating that some of the monomer signal arises from cracking of the dimer into the monomer mass channel. In order to test for the contribution of cracking to the observed dimer spectrum, we lowered the concentration of chlorobenzene in mixture below 1% by cooling the sample bath, which effectively reduced the concentration of higher order clusters. At a point at which the trimer signal can barely be observed, the dimer spectrum is unchanged, still retaining its very broad appearance (Figure 6.5).

A second explanation for the broadness in the cluster spectra is the presence of different isomers, which might absorb at different wavelengths. Indeed, a motivating aspect of this study was the exploration of the relative importance of different non-covalent interactions in these clusters. This was examined using calculations at the M062x and MP2 levels with an aug-cc-pVDZ basis set, with geometry optimizations initiated from a variety of starting geometries that loosely corresponded to π-stacked, C-H/π, and halogen–bonded structures (Figure 6.2).
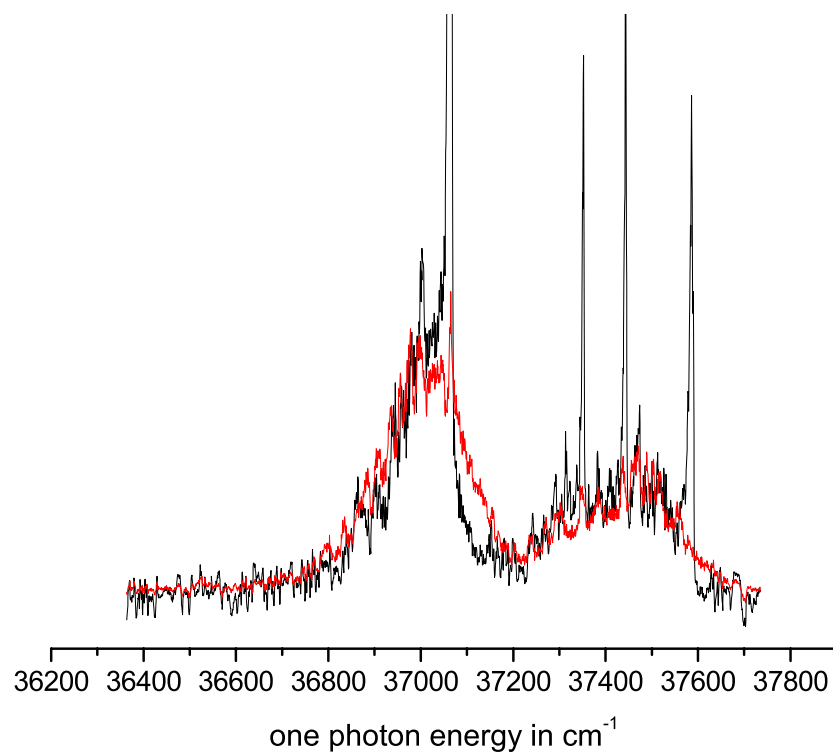
Figure 6.4: Comparison of R2PI spectrum measured in the dimer (red) and monomer (black) mass channels. The monomer spectrum has been scaled by a factor of 5.
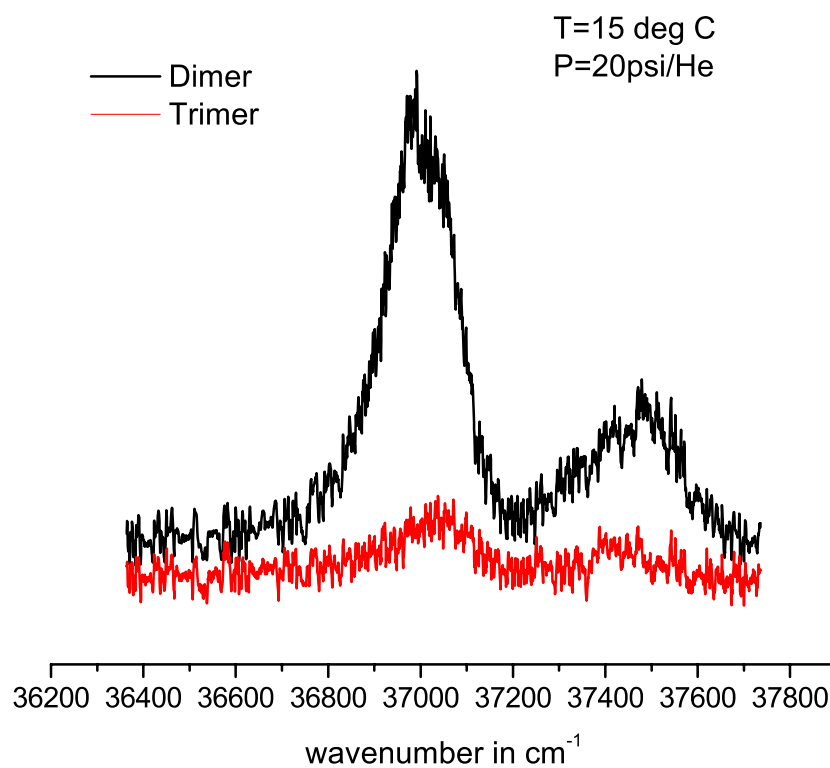
Figure 6.5: R2PI spectra of the chlorobenzene dimer (black) and trimer (red) with a bath temperature of 15°C. At this temperature, the trimer signal is barely visible, but the dimer spectrum is unchanged.

In all, five minimum energy structures (D1-D5) were found for the chlorobenzene dimer, and the optimized (M06-2x/aug-cc-pVDZ) structures are shown in Figure 6.6, together with the calculated binding energies, which were counterpoise and ZPE corrected. Dimers D1-D4 were found to be π-stacked with a parallel–displaced structure, consistent with previous findings for related systems.[214,237,252,258] In these structures the planes of the two monomers are separated by ~ 3.3 Å, so that the two Cl atoms are not in close van der Waals contact. This gives rise to four different π-stacked isomers, differing in the relative orientation of the Cl atoms (Figure 6.6), which are nearly isoenergetic, with calculated binding energies between ~ 17 and ~ 20 kJ/mol. In addition to the π-stacked isomers, a T-shaped isomer (D5) was also found, with a calculated binding energy roughly one-half that of the π-stacked isomers. No minima corresponding to halogen–bonded structures were located.

Comparing the M06-2x/aug-cc-pVDZ results with other calculations, we find that the calculated MP2/aug-cc-pVDZ binding energy of dimer 1 (D1) is ~ 27 kJ/mol. This difference is not surprising, as it is well known that the MP2 method tends to overbind complexes that are dominated by dispersion interactions.[318,319] In comparison, a counterpoise corrected CCSD(T)//M06-2x/aug-cc-pVDZ calculation using ZPE corrections at the M06-2x/aug-cc-pVDZ level yields a binding energy of 13.8 kJ/mol, which suggests that the M06-2x results are also overestimates. The coupled cluster prediction is in excellent agreement with the experimentally determined binding energy of the dimer (14.4 ± 1.0 kJ/mol), which is discussed in more detail below.
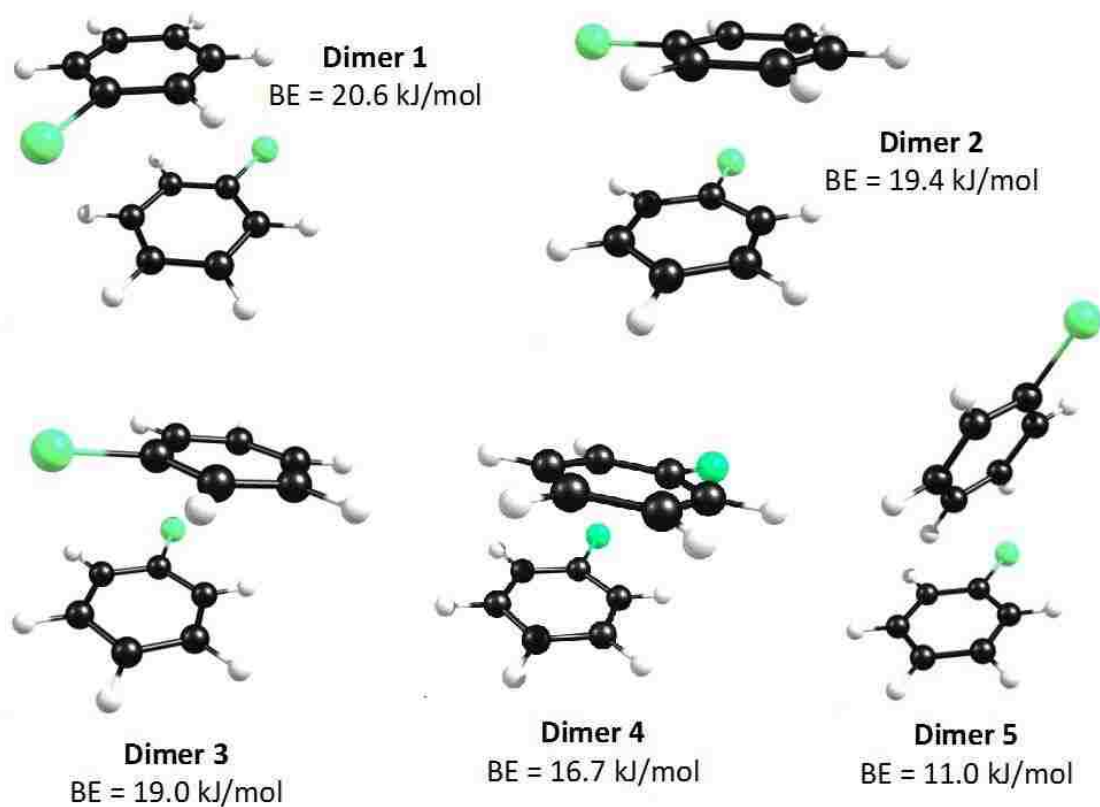
Figure 6.6: Optimized structures (D1-D5) for the chlorobenzene dimer, calculated at the M06-2x/aug-cc-pVDZ level of theory. Binding energies are counterpoise and ZPE corrected.

Figure 6.7 shows the calculated TDDFT (TDM06-2x/aug-cc-pVDZ) spectra of the chlorobenzene dimers D1-D5 and the monomer, referenced to the numbering scheme given in Figure 6.6 and shown as stick spectra. Quantitatively, the TDDFT calculations overestimate the position of the S_1 state of the monomer; however, we expect that trends in these calculations should be valid, and this is addressed further below. The calculated spectra of the dimers show two absorptions, as expected, which correspond to the shifted monomer absorptions. In all the dimers, these are uniformly shifted to lower energy (red-shifted) compared to the monomer absorption, and the absorption lying closest to the monomer transition is that for the "free" chlorobenzene in the T-shaped dimer. For the π-stacked dimers, there are few obvious trends in the calculated spectra; however, it appears that the red-shift increases with decreasing separation of the Cl atoms. The calculated spectra of the various isomers occur over a range that, when scaled to reflect the overestimation of the transition energy, is of an order similar (i.e., ~ 200 cm^{-1}) to that observed experimentally.

In order to assess the dependence of these results on the method used, we carried out additional calculations on the chlorobenzene monomer and dimer 1, used as a representative example. These employed a wider range of functionals, including ωB97X-D,[307] M06,[74] and CAM-B3LYP,[308,309] and the results are shown in Figure 6.8 . The trends observed in these calculations are consistent, with the transitions of the dimer lying to the red (lower energy) of the monomer transition. There is some variation in the magnitude of the calculated red-shift, with the ωB97X-D and CAM-B3LYP results displaying smaller shifts as compared with M06 and M06-2x.
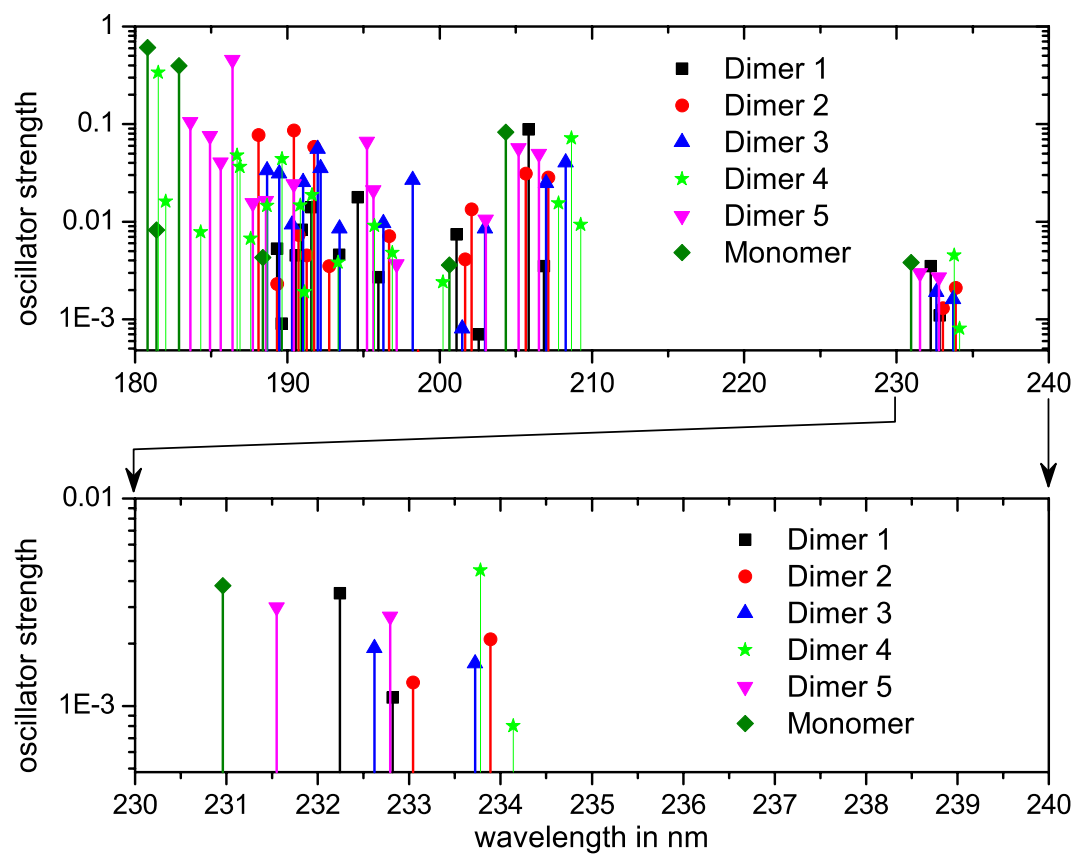
Figure 6.7: Calculated TDDFT (TDM06-2x/aug-cc-pVDZ) spectra of the chlorobenzene dimers shown in Figure 6.6 .
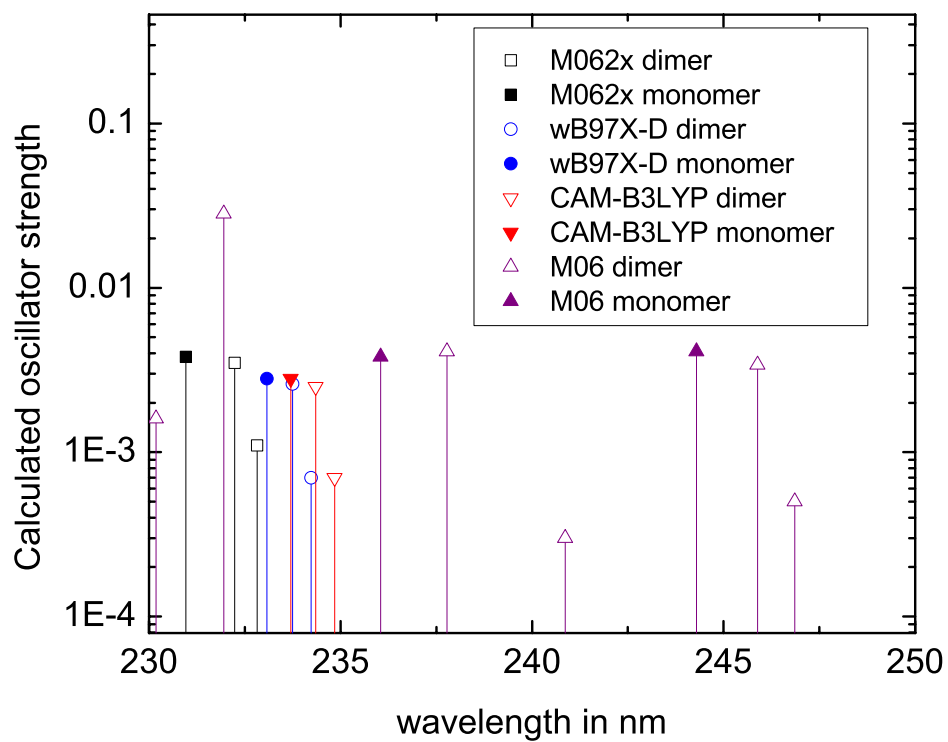
Figure 6.8: Calculated TDDFT spectra of the chlorobenzene monomer and dimer 1 using the variety of functionals shown, with an aug-cc-pVDZ basis set.

In addition to inhomogeneous broadening arising from the different isomers in the beam, additional features are expected for each isomer arising from vibrational structure based upon the Franck-Condon (FC) activity in the electronic transition. To model this, we optimized the structure of the lowest lying excited electronic state of dimer 1 (Figure 6.6) at the TDM06-2x/aug-cc-pVDZ level. The optimized structures of the ground and excited states of this dimer are shown in Figure 6.9; interestingly, the calculations predict a transition from a parallel–displaced structure in the ground state to a sandwich structure in the excited state, with the distance between the monomers decreasing from 3.3 to 3.0 Å. A sandwich structure was predicted for the equilibrium geometry of the lowest excited valence state of the benzene dimer.[320,321] As a result of this geometry change, significant FC activity is expected in low frequency torsional modes that involve displacement of the two monomer subunits; the vibrational displacements associated with the lowest frequency such mode ($\omega \sim 26$ cm^{-1}) in the ground state are shown in Figure 6.9. To simulate the vibronic spectrum, we incorporated the calculated vibrational frequency and mass-weighted cartesian displacements (i.e., l–matrices) of this mode in the ground and excited electronic states into a FC simulation that accounted for the effects of Dushinsky mixing. These calculations were performed using a routine in the PGOPHER program suite.[322] The calculated spectrum (Figure 6.9), shows significant FC activity in this mode. While this simulation is illustrative, in the sense that it is not meant to completely capture the vibrational structure in the spectrum and is based on a harmonic approximation which may be a poor description of these low frequency intermolecular modes,[281,282] it does suggest that additional features will arise from FC activity in the spectrum, which will further contribute to the observed broadening.
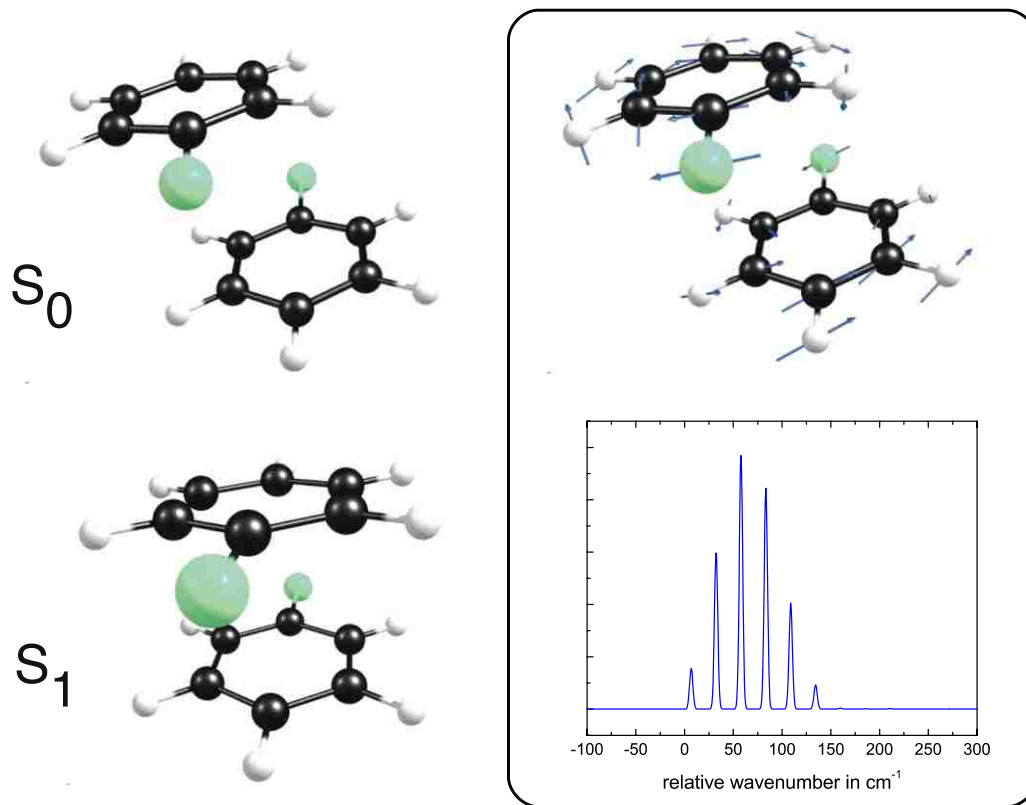
Figure 6.9 : At left: Optimized structures of the ground and lowest energy excited electronic state of chlorobenzene dimer 1. At right: Ground state displacements for the lowest energy torsional mode, and simulated spectrum showing the FC activity in this mode in the S_0–S_1 transition of the dimer, as described in the text.

Indeed, the vestiges of this structure appear in the measured dimer spectrum (Figure 6.3), which we did not attempt to model quantitatively due to the presence of multiple isomers. Given the low frequency of this and other intermolecular modes, hot-band structure may also be present.

Thus far we have neglected contributions from homogeneous broadening. In a related study of the complexes of 2-pyridone with substituted fluorobenzenes, Leutwyler and co-workers found that the complexes of partially fluorinated benzenes exhibited sharp spectra indicative of a hydrogen-bonded complex.[281,282] In contrast, the π-stacked complex with hexafluorobenzene exhibited a number of very broad features, which were explained in terms of vibronic structure in the low frequency intermolecular modes. Hole-burning experiments revealed the presence of two isomers, and indicated that the primary broadening mechanism in the spectra was homogeneous broadening.[276] Indeed, the ultrafast experiments on chlorobenzene clusters reveal a bi-exponential decay with a short lifetime component on the order of ~200 fs. Thus, while our analysis of the chlorobenzene dimer spectrum shows that the general features can be adequately explained by the presence of multiple isomers and vibrational activity in low frequency intermolecular motions, homogeneous broadening must also be a contributing factor. Hole-burning experiments will be needed to assess the relative contributions of homogeneous and inhomogeneous broadening to the spectrum.

6.7. Higher Order Clusters for Chlorobenzene: n>2

Moving to the higher clusters, an important question is: *Why is the spectrum of the trimer and tetramer so similar to that of the dimer?* To answer this question, we calculated representative structures of the trimer at the M06-2x/aug-cc-pVTZ level. A total of six minimum energy trimer structures were found, (T1-T6), shown in Figure 6.10 , which exhibit the same noncovalent interactions (π-π stacking, CH/π) found to be important in the dimer. The binding energies (BE) of these trimers were counterpoise and ZPE corrected and are referenced to the energy of three monomers. As Sherrill and co-workers have previously shown,[323] aromatic clusters do not exhibit significant non-additive effects in their binding, and thus the binding energies (~ 40 kJ/mol) of the fully π-stacked trimers (T3 and T4) are roughly twice the energy of the π-stacked dimer. The remaining trimer configurations (T1, T2, T5, and T6) typically have a stacked dimer core, with the third monomer interacting with this core through CH/π interactions. These display a BE of 30-39 kJ/mol. It is important to note that many additional minimum energy structures for the trimer can be envisaged; however, the calculated structures shown in Figure 6.10 are considered to be representative. It is reasonable to expect that all of these isomers are present, to a varying degree, in our beam.
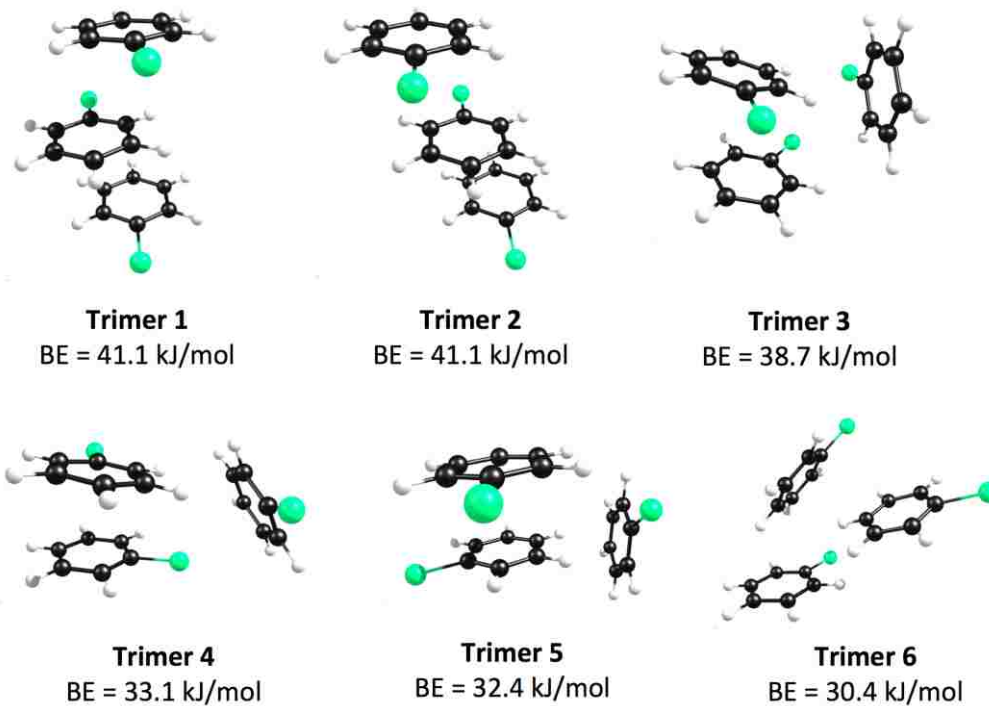
Figure 6.10 : Optimized structures (T1-T6) for the chlorobenzene trimer, calculated at the M06-2x/aug-cc-pVDZ level of theory. Binding energies are counterpoise and ZPE corrected, and are referenced to the energy of three separated monomers.

Figure 6.11 displays the calculated (TDM06-2x/aug-cc-pVDZ) spectra of trimers T1-T6. These spectra show three transitions per trimer; typically one of these is weak. As found for the dimers, the calculated transitions are red–shifted with respect to the monomer absorption, without an obvious pattern. Importantly, the range over which these absorptions occur is very similar to that observed for the dimers. Thus, the similarity of the dimer and trimer spectra is in part explained by the presence of multiple isomers, whose electronic spectra span a similar range.

As discussed in the introduction to this chapter, to explain the similarity of R2PI spectra for toluene clusters of different size Wright and co-workers proposed that the favored (π–stacked) binding motif of the dimer formed the core of higher order clusters, leading to a dimer–based "chromophore".[324] While it is certainly true that in our system as well a π–stacked dimer is found in the majority of trimer structures (Figure 6.10), we view it as simply the fact that noncovalent interactions in the dimer and trimer (and presumably larger clusters as well) are similar, leading to shifts in the electronic absorptions that occur over a similar range (Figure 6.7 and Figure 6.11), which gives rise to the similarity of spectra for different clusters.

This dimer-based model of stacking in toluene clusters has also been invoked to explain the dependence of ionization potential on cluster size.[275] As noted above, a reduction in the ionization potential of the toluene dimer relative to the monomer was found, consistent with the participation of a π–stacked dimer where the charge is delocalized over both rings.[275] This suggests the importance of π–stacking in the dimer, and is consistent with our finding that 80% of optimized (calculated) chlorobenzene dimer structures contain this motif.
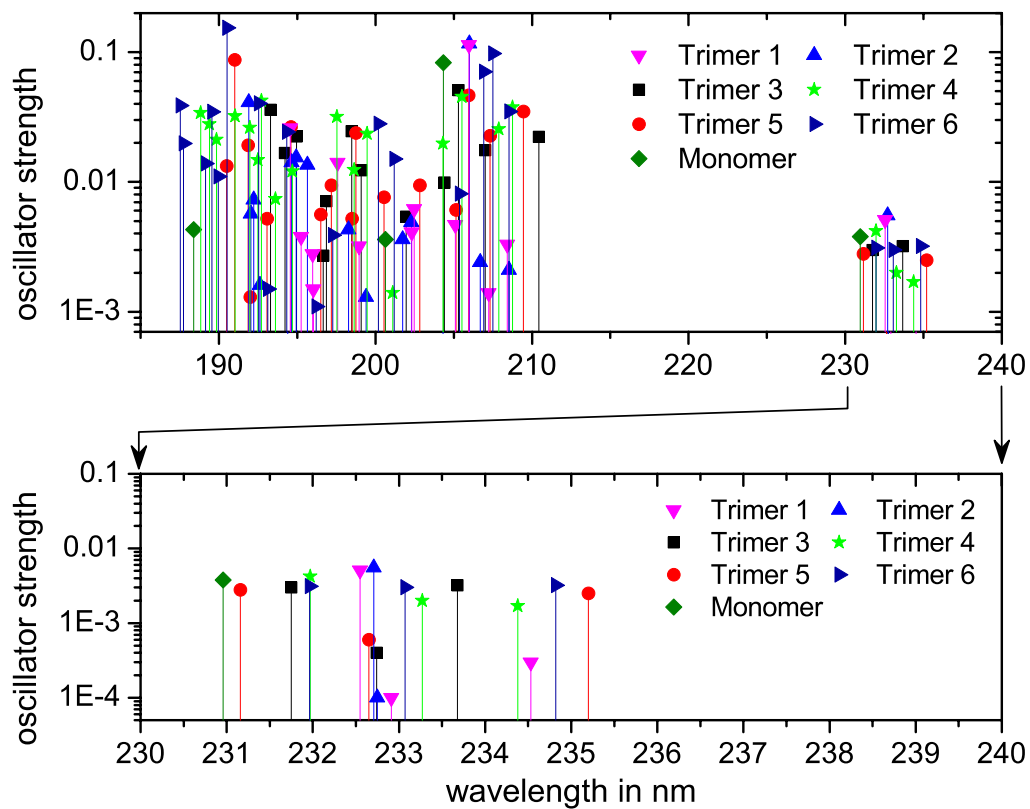
Figure 6.11: Calculated TDDFT (TDM06-2x/aug-cc-pVDZ) spectra of the chlorobenzene trimers shown in Figure 6.10 .

In contrast, the ionization potential of the trimer and tetramer of toluene was found to be similar to the dimer, which was taken as evidence against the existence of the (lower energy) fully π–stacked clusters in the beam, and it was argued that the lack of relaxation in the beam favored formation of higher energy structures. Given the range of possible isomers, each present to an unknown degree and displaying an ionization potential dependent upon the degree of π–stacking, it is clear that the interpretation of ionization potential measurements made from single photon VUV excitation should be made with care.

Moving to the chlorobenzene tetramer, we obtained an R2PI spectrum (Figure 6.3), which again was broad and red shifted compared to the monomer absorption, and similar to the spectrum of the dimer and trimer. Due to the computational resources required in characterizing even a representative set of the large number of potential isomeric structures, we made no effort to run electronic structure calculations for the tetramer. However, one can reasonably predict that the interactions observed in the dimer and trimer will also be important in the tetramer, and it is also reasonable to assume, based upon the analysis presented here, that the similarity of the tetramer spectrum to that of the dimer and trimer can be explained by the presence of multiple isomers.

Comparing our results with previous R2PI studies of the chlorobenzene dimer by Lu and co-workers,[285] we note that a feature observed to higher energy of the monomer origin was assigned in that work to the π-stacked dimer. We observe a shoulder on the dimer spectrum (see Figure 6.3) at this position.

However, our calculations predict that the highest energy dimer absorption is that for the T-shaped (not parallel displaced) isomer, and thus the blue shifted feature most probably reflects vibrational structure associated with the absorption of this isomer.

Lu and co-workers found that the intensity of the blue-shifted feature greatly increased when using Ar (rather than He) as backing gas, and further increased with an increase in backing pressure. It is possible that the different expansion conditions may favor formation of the higher energy T-shaped isomer, through an unknown mechanism. In this work we did not carry out experiments with Ar backing gas, to avoid contributions from van der Waals complexes of Ar and chlorobenzene. For their binding energy measurements, Lu and co-workers used He backing gas at a relatively low backing pressure, which would favor the red-shifted (π-stacked) component. This is consistent with the very good agreement between the experimentally measured binding energy (14.4 $\pm$ 1.0 kJ/mol) and the calculated CCSD(T)//M06-2x/aug-cc-pVDZ binding energy of dimer D1 (13.8 kJ/mol).

In this work no evidence of halogen–bonded structures was found, either experimentally or computationally. Apparently, the lack of electron withdrawing substituents on the phenyl moiety minimizes the magnitude of the σ-hole, rendering the halogen bonding interactions weaker than π–stacking and CH/π interactions. From that point of view, fluorine substitution should increase the magnitude of the former. However, we note that a recent experimental study of C_6F_5X (X=Cl,Br,I) complexation in C_6D_6 solution using NMR spectroscopy found evidence for halogen bonding only in the case of X =I.[243]

In an effort to probe the excited state lifetime of the chlorobenzene clusters, we carried out R2C2PI experiments using the 266 nm output of a second Nd:YAG laser to ionize from the S_1 state. As mentioned above, ultrafast experiments have found a bi-exponential decay from the intermediate state, with a fast component on the order of 150-200 fs that was assigned to internal conversion to S_0 and a much slower (ns) component that was assigned to dissociation from highly excited vibrational levels of S_0. For the long lifetime component, there is an increase in lifetime with increasing cluster size, with the measured tetramer lifetime ~ 3.7 ns. Given the 5-8 ns pulse width of our lasers, we were unable to detect a difference in lifetime for the clusters as compared to the monomer. We did confirm the short lifetime of the intermediate state, as R2C2PI signal could only be observed when the laser pulses were overlapped both temporally and spatially.

Finally, we note that the results found here are likely to be of general validity in understanding the similarly broad R2PI spectra that have been previously reported for other related systems, including not only toluene but other halobenzenes[278] and mixed halobenzene/benzene clusters.[285] Our results suggest that this broadening arises in large part from inhomogeneous sources, including the presence of multiple isomers and Franck-Condon activity associated with geometrical changes induced by electronic excitation, which is particularly important for the π–stacked clusters that display very low frequency intermolecular vibrations.

6.8. Summary

Motivated by a desire to examine competitive non–covalent interactions in a prototypical system, we have examined the chlorobenzene monomer and clusters (Clbz)$_n$ with n=2-4 using R2PI spectroscopy in concert with electronic structure calculations. The R2PI spectra of the clusters, obtained in the origin region of the $S_0 - S_1$ ($\pi\pi^*$) state of the monomer, show a broad spectrum whose center is red–shifted from the monomer absorption, and which is similar for all cluster sizes examined. These observations are explained with the aid of electronic structure calculations. For the dimer, calculations find five minimum energy structures, four π-stacked and one T-shaped structure bound through CH/π interaction. The calculated TDDFT spectra show that these isomers absorb over a broad range, and, in agreement with experiment, the calculated absorptions are red–shifted with respect to the monomer transition. Due to the significant geometry change in the two electronic states, where electronic excitation induces a transition from a parallel displaced to sandwich structure with a reduced separation of the two monomers, significant FC activity is predicted in low frequency intermolecular modes of the complex.

For the trimer, six representative structures were found, displaying a combination of π-stacking and CH/π interactions. The calculated TDDFT spectra of these trimers are similar to those obtained for the dimers, consistent with the similarity of the experimental spectra for these clusters.

Overall, our results show that the spectral broadening arises in large part from inhomogeneous sources, including the presence of multiple isomers and Franck-Condon activity associated with geometrical changes induced by electronic excitation. The latter is particularly important for the π-stacked structures, due to the presence of low frequency intermolecular modes.

Building upon these studies, a variety of additional experiments would aid in understanding the properties of the chlorobenzene clusters. Hole-burning experiments would help identify the spectral features associated with different ground state structures, while higher resolution mass-analyzed threshold ionization (MATI) or zero-kinetic energy electron (ZEKE) spectroscopic methods are also attractive for application to this system. Finally, R2C2PI experiments with two tunable sources are attractive for probing the isomer dependence of the ionization potential, and unraveling contributions in the spectra from different isomers.

REFERENCES

(1) IUPAC **1994**, p 1126.

(2) Turecek, F. *Modern Mass Spectrometry* **2003**, *225*, 77-129.

(3) Fabris, D. *Mass Spectrometry Reviews* **2005**, *24*, 30-54.

(4) Santos, L. S. *European Journal of Organic Chemistry* **2008**, 235-253.

(5) Jacox, M. E. *Abstracts of Papers of the American Chemical Society* **1985**, *190*, 8-Phs.

(6) Jacox, M. E. *Journal of Physical and Chemical Reference Data* **1990**, *19*, 1387-1546.

(7) Jacox, M. E. *Journal of Physical and Chemical Reference Data* **1994**, 1-461.

(8) Jacox, M. E. *Journal of Physical and Chemical Reference Data* **1998**, *27*, 115-393.

(9) Jacox, M. E. *Chemical Society Reviews* **2002**, *31*, 108-115.

(10) Jacox, M. E. *Journal of Physical and Chemical Reference Data* **2003**, *32*, 1-441.

(11) Jacox, M. E. *Accounts of Chemical Research* **2004**, *37*, 727-734.

(12) Zavoisky, E. *J. Phys* **1945**, *9*.

(13) *Introduction to Free Radical Chemistry* 1st ed.; Pryor, W. A., Ed.; Prentice-Hall: NJ, **1996**.

(14) Weisshaar, J. C. *Accounts of Chemical Research* **1993**, *26*, 213-219.

(15) *Perspectives in the Selective Activation of C-H and C-C Bonds in Saturated Hydrocarbons*; 1st ed.; Meunier, B.; Chaudret, B., Eds.; Scientific Affairs Division-NATO Brussels, **1988**.

(16) *Organo Transition Metal Compounds As Intermediates In Homogeneous Catalytic Reactions*; 1st ed.; Gunther, W., Ed.; Pergamon press Ltd: Great Britain **1978**; Vol. 50.

(17) *Carbene Chemistry* 1st ed.; Kirmse, W., Ed.; Academic: New York, **1971**.

(18) *Advanced Organic Chemistry, part 3*; Carey, F. A.; Sundberg, R. J., Eds.; Plenum press: New York, **1990**.

(19) *In Gas Phase Reactions in Organic Synthesis*; Weirsum, U. E.; Jenneskens, L. W., Eds.; Gordon and Breach: Amsterdam **1997**.

(20) *Carbenes,Vol. I-II in Reactive Intermediates in Organic Chemistry Series*; Moss, R. A., Jones Jr,M., Ed.; Wiley-Interscience: New York **1975**; Vol. I-II.

(21) *In Handbook of Organic Photochemistry*; Sciano, J. C., Ed.; CRC Press: Boca Raton, Fl, **1989**; Vol. II.

(22) Mukarakate, C.; Mishchenko, Y.; Brusse, D.; Tao, C.; Reid, S. A. *Physical Chemistry Chemical Physics* **2006**, *8*, 4320-4326.

(23) Tao, C.; Deselnicu, M.; Fan, H. Y.; Mukarakate, C.; Ionescu, L.; Reid, S. A. *Physical Chemistry Chemical Physics* **2006**, *8*, 707-713.

(24) Tao, C.; Mukarakate, C.; Brusse, D.; Mishchenko, Y.; Reid, S. A. *Journal of Molecular Spectroscopy* **2007**, *241*, 180-185.

(25) Tao, C.; Mukarakate, C.; Reid, S. A. *Journal of Molecular Spectroscopy* **2007**, *246*, 113-117.

(26) Tao, C.; Mukarakate, C.; Reid, S. A. *Journal of Molecular Spectroscopy* **2007**, *241*, 136-142.

(27) Mukarakate, C.; Tao, C.; Jordan, C. D.; Polik, W. F.; Reid, S. A. *Journal of Physical Chemistry A* **2008**, *112*, 466-471.

(28) Richmond, C.; Tao, C.; Mukarakate, C.; Fan, H.; Nauta, K.; Schmidt, T. W.; Kable, S. H.; Reid, S. A. *Journal of Physical Chemistry A* **2008**, *112*, 11355-11362.

(29) Tao, C.; Ebben, C.; Ko, H. T.; Reid, S. A. *Physical Chemistry Chemical Physics* **2008**, *10*, 6090-6092.

(30) Tao, C.; Mukarakate, C.; Judge, R. H.; Reid, S. A. *Journal of Chemical Physics* **2008**, *128*, -.

(31) Tao, C.; Mukarakate, C.; Terranova, Z.; Ebben, C.; Judge, R. H.; Reid, S. A. *Journal of Chemical Physics* **2008**, *129*, -.

(32) Tao, C.; Ebben, C.; Reid, S. A. *Journal of Physical Chemistry A* **2009**, *113*, 13407-13412.

(33) Zou, W. L.; Liu, W. J. *J. Chem. Phys.* **2006**, *124*, 154312.

(34) Hay, P. J.; Wadt, W. R. *Journal of Chemical Physics* **1985**, *82*, 270-283.

(35) Langhoff, S. R.; Bauschlicher, C. W. *Annual Review of Physical Chemistry* **1988**, *39*, 181-212.

(36) Langhoff, S. R.; Bauschlicher, C. W. **1988**, *39*.

(37) Newby, J. J.; Stearns, J. A.; Liu, C. P.; Zwier, T. S. *Journal of Physical Chemistry A* **2007**, *111*, 10914-10927.

(38) Collier, J. L.; Goddard, B. J.; Goode, D. C.; Marka, S.; Telle, H. H. *Measurement Science & Technology* **1996**, *7*, 1204-1211.

(39) Ayles, V. L.; Muzangwa, L. G.; Reid, S. A. *Chemical Physics Letters* **2010**.

(40) Bouddou, A.; Dufour, C.; Pinchemel, B. *Journal of Molecular Spectroscopy* **1994**, *168*, 477-482.

(41) Carette, P.; Hocquet, A.; Douay, M.; Pinchemel, B. *Journal of Molecular Spectroscopy* **1987**, *124*, 243-271.

(42) Deselnicu, M.; Tao, C.; Mukarakate, C.; Reid, S. A. *Journal of Chemical Physics* **2006**, *124*.

(43) Douay, M.; Pinchemel, B.; Dufour, C. *Canadian Journal of Physics* **1985**, *63*, 1380-1388.

(44) Fan, H.; Ionescu, I.; Annesley, C.; Cummins, J.; Bowers, M.; Reid, S. A. *Journal of Molecular Spectroscopy* **2004**, *225*, 43-47.

(45) Fan, H. Y.; Mukarakate, C.; Deselnicu, M.; Tao, C.; Reid, S. A. *Journal of Chemical Physics* **2005**, *123*.

(46) Focsa, C.; Pinchemel, B. *Chemical Physics* **1999**, *247*, 395-405.

(47) Hirao, T.; Dufour, C.; Pinchemel, B.; Bernath, P. F. *Journal of Molecular Spectroscopy* **2000**, *202*, 53-58.

(48) Kadavathu, S. A.; Scullman, R.; Field, R. W.; Gray, J. A.; Li, M. *Journal of Molecular Spectroscopy* **1991**, *147*, 448-470.

(49) Krouti, Y.; Poclet, A.; Hirao, T.; Pinchemel, B.; Bernath, P. F. *Journal of Molecular Spectroscopy* **2001**, *210*, 41-50.

(50) Lefebvre, Y.; Pinchemel, B.; Delaval, J. M.; Schamps, J. *Physica Scripta* **1982**, *25*, 329-332.

(51) Minton, T. K.; Kim, H. L.; Reid, S. A.; Mcdonald, J. D. *Journal of Chemical Physics* **1988**, *89*, 6550-6552.

(52) Petrongolo, C.; Fan, H. Y.; Ionescu, I.; Kuffel, D.; Reid, S. A. *Journal of Chemical Physics* **2003**, *119*, 2614-2617.

(53) Poclet, A.; Krouti, Y.; Hirao, T.; Pinchemel, B.; Bernath, P. F. *Journal of Molecular Spectroscopy* **2000**, *204*, 125-132.

(54) Tao, C.; Mukarakate, C.; Reid, S. A. *Journal of Chemical Physics* **2006**, *124*.

(55) Tao, C.; Mukarakate, C.; Reid, S. A. *Chemical Physics Letters* **2007**, *449*, 282-285.

(56) Xin, J.; Fan, H. Y.; Ionescu, I.; Annesley, C.; Reid, S. A. *Journal of Molecular Spectroscopy* **2003**, *219*, 37-44.

(57) NIST, *V.30:(http://physics.nist.gov/physRefData/ASD)*.

(58) *Mass Spectrometry :Techniques and Applications*; 1st ed.; Milne, G. W. A., Ed.; Wiley-Interscience **1971**.

(59) *Introduction Mass Spectrometry*; 1st ed.; Stephen, S., Ed.; Analytical and Consulting Laboratories: Boston **1971**.

(60) Fan, H. Y.; Ho, W.; Reid, S. A. *International Journal of Mass Spectrometry* **2003**, *230*, 11-17.

(61) Eiding, J.; Schneider, R.; Domcke, W.; Koppel, H.; Vonniessen, W. *Chemical Physics Letters* **1991**, *177*, 345-351.

(62) Ayles, V. L.; Muzangwa, L. G.; Reid, S. A. *Chemical Physics Letters* **2010**, *497*, 168-171.

(63) Muzangwa, L. G.; Ayles, V. L.; Nyambo, S.; Reid, S. A. *Journal of Molecular Spectroscopy* **2011**, *269*, 36-40.

(64) Tao, C.; Mukarakate, C.; Mishchenko, Y.; Brusse, D.; Reid, S. A. *Journal of Physical Chemistry A* **2007**, *111*, 10562-10566.

(65) Born, M.; Oppenheimer, R. *Ann. Phys* **1927**, *84*, 457.

(66) *Exploring Chemistry with Electronic Structure Methods*; Foresman, J., B. and Frisch AEleen Ed.; Gaussian Inc: Pittsburg, **1993**.

(67) Ramachandran, K. I., Deepa,G., Namboori,K. *Computational Chemistry and Molecular Modeling: Principles and applications*; Springer: Berlin **2008**.

(68) *Molecular Modelling :Principle and Applications*; Leach, A., R., Ed.; Prentice Hall: Essex England **2001**.

(69) *Essentials of Computational Chemistry: Theories and Models*; Cramer, C. J., Ed.; John Wiley and sons,: West Sussex, **2004**.

(70) *Quantum Chemical Methods In Main-Group Chemistry*; 1st ed.; Klapotke, T. M.; Schulz, A., Eds.; John Wiley and Sons: New York **1998**.

(71) Hohenberg, P.; Kohn, W. *Phys Rev* **1964**, *136*.

(72) Kohn, W.; Sham, L. J. *Phys Rev* **1965**, *A1133*.

(73) Bryantsev, V. S.; Diallo, M. S.; van Duin, A. C. T.; Goddard, W. A. *Journal of Chemical Theory and Computation* **2009**, *5*, 1016-1026.

(74) Zhao, Y.; Truhlar, D. G. *Theoretical Chemistry Accounts* **2008**, *120*, 215-241.

(75) Zhao, Y.; Truhlar, D. G. *Journal of Chemical Physics* **2006**, *125*.

(76) Gross, E. K. U., and Kohn, W. *Adv. Quantum Chem* **1990**, *21*.

(77) *Constants of Diatomic Molecules*; Huber, K. P.; Herzberg, G., Eds.; Van Nostrand: New York, **1979**.

(78) Bauschlicher, C. W.; Walch, S. P.; Langhoff, S. R.; Veillard, A., Ed.; NATO ASI **1986**.

(79) Langhoff, S. R. a. B., C.W. *Annual Review of Physical Chemistry* **1988**, *39*.

(80) Hirota, E. *Annual report progress physical chemistry*, **2000**.

(81) Bernath, P. F. *Annual report progress physical chemistry*, **2000**.

(82) Langhoff, S. R.; Bauschlicher, C. W. *J. Chem. Phys.* **1988**, *88*, 329-336.

(83) Tsuji, J.; John Wiley and sons,: **2000**.

(84) Rao, C. N. **1989**, *40*.

(85) Grunze, M.; king, D. A. a. W., D.P., Ed.; Elsevier: New York, **1982**; Vol. 4.

(86) Cotton, F. A.; Wilkinson, G.; 5th ed.; Wiley, Ed. New York, **1988**.

(87) Wojuechowsba, M., Habu,J.,Lomnicki,S. and Stoch,J. *J.Mol.catal. A:chem* **1999**, *141*.

(88) Davis, D. N. *Astrophys.journal* **1949**, *106*.

(89) Spinard, H.; *et al. Annual Review of Astron.Astrophys* **1969**, *7*.

(90) Pinchemel, B. *Journal of Physics B-Atomic Molecular and Optical Physics* **1981**, *14*, 2569.

(91) Dufour, C.; Carette, P.; Pinchemel, B. *Journal of Molecular Spectroscopy* **1991**, *148*, 303-309.

(92) Carette, P.; Dufour, C.; Pinchemel, B. *Journal of Molecular Spectroscopy* **1993**, *161*, 323-335.

(93) Dufour, C.; Hikmet, I.; Pinchemel, B. *Journal of Molecular Spectroscopy* **1993**, *158*, 392-398.

(94) Dufour, C.; Hikmet, I.; Pinchemel, B. *Journal of Molecular Spectroscopy* **1994**, *165*, 398-405.

(95) Dufour, C.; Pinchemel, B. *Journal of Molecular Spectroscopy* **1995**, *173*, 70-78.

(96)   Focsa, C.; Dufour, C.; Pinchemel, B. *Journal of Molecular Spectroscopy* **1997**, *182*, 65-71.

(97)   Krouti, Y.; Hirao, T.; Dufour, C.; Boulezhar, A.; Pinchemel, B.; Bernath, P. F. *Journal of Molecular Spectroscopy* **2002**, *214*, 152-174.

(98)   Leung, J. W. H.; Wang, X. H.; Cheung, A. S. C. *J. Chem. Phys.* **2002**, *117*, 3694-3700.

(99)   O'Brien, J. J.; Miller, J. S.; O'Brien, L. C. *Journal of Molecular Spectroscopy* **2002**, *211*, 248-253.

(100) O'Brien, L. C.; Homann, K. M.; Kellerman, T. L.; O'Brien, J. J. *Journal of Molecular Spectroscopy* **2002**, *211*, 93-98.

(101) Pinchemel, B.; Hirao, T.; Bernath, P. F. *Journal of Molecular Spectroscopy* **2002**, *215*, 262-268.

(102) Tam, W. S.; Leung, J. W. H.; Hu, S. M.; Cheung, A. S. C. *J. Chem. Phys.* **2003**, *119*, 12245-12250.

(103) Yamazaki, E.; Okabayashi, T.; Tanimoto, M. *J. Chem. Phys.* **2004**, *121*, 162-168.

(104) Benomier, M.; van Groenendael, A.; Pinchemel, B.; Hirao, T.; Bernath, P. F. *Journal of Molecular Spectroscopy* **2005**, *233*, 244-255.

(105) Miyazawa, T.; Okabayashi, E. Y.; Koto, F.; Tanimoto, M.; Okabayashi, T. *J. Chem. Phys.* **2006**, *124*.

(106) Zou, W.; Liu, W. *J. Chem. Phys.* **2006**, *124*, 154312/1-154312/16.

(107) Zou, W. L.; Liu, W. J. *J. Chem. Phys.* **2006**, *124*.

(108) Bauschlicher, C. W.; Walch, S. P.; Langhoff, S. R.; Taylor, P. R.; Jaffe, R. L. *J. Chem. Phys.* **1988**, *88*, 1743-1751.

(109) Langhoff, S. R.; Bauschlicher, C. W. *J. Chem. Phys.* **1988**, *89*, 2160-2169.

(110) Langhoff, S. R.; Bauschlicher, C. W.; Partridge, H. *J. Chem. Phys.* **1988**, *89*, 396-407.

(111) Langhoff, S. R.; Bauschlicher, C. W.; Pettersson, L. G. M. *J. Chem. Phys.* **1988**, *89*, 7354-7362.

(112) Langhoff, S. R.; Bauschlicher, C. W.; Taylor, P. R. *J. Chem. Phys.* **1988**, *88*, 5715-5725.

(113) Partridge, H.; Langhoff, S. R.; Bauschlicher, C. W. *J. Chem. Phys.* **1988**, *88*, 6431-6437.

(114) Partridge, H.; Langhoff, S. R.; Bauschlicher, C. W.; Schwenke, D. W. *J. Chem. Phys.* **1988**, *88*, 3174-3186.

(115) Zou, W.; Liu, W. *J. Comput. Chem.* **2007**, *28*, 2286-2298.

(116) Dawes, R.; Jasper, A. W.; Tao, C.; Richmond, C.; Mukarakate, C.; Kable, S. H.; Reid, S. A. *Journal of Physical Chemistry Letters* **2010**, *1*, 641-646.

(117) Gray, J. A.; Li, M. G.; Nelis, T.; Field, R. W. *J. Chem. Phys.* **1991**, *95*, 7164-7178.

(118) Tam, W. S.; Ye, J.; Cheung, A. S. C. *J. Chem. Phys.* **2004**, *121*, 9430-9435.

(119) Ye, J. J.; Leung, J. W. H.; Cheung, A. S. C. *J. Chem. Phys.* **2006**, *125*.

(120) Mesnage, P. *Ann.phys.* **1939**, *125*.

(121) krishnamurty, V. G. *Indian Journal of Pure & Applied Physics* **1952**, *26*.

(122) Reddy, S. P.; Rao, P. T. *proc.phys.soc* **1960**, *75*.

(123) Ye, J. J.; Leung, J. W. H.; Cheung, A. S. C. *J. Chem. Phys.* **2006**, *125*, -.

(124) PGOPHER *http://pgopher.chm.bris.ac.uk*.

(125) Lefebvre-Brion, H.; Field, R. W.; Academic Press, Ed. New York, **1986**.

(126) Yang, C. L.; Gao, F.; Zhang, X. Y.; Han, K. L. *J. Chem. Phys.* **2005**, *123*.

(127) Tam, W. S.; Ye, J. J.; Cheung, A. S. C. *J. Chem. Phys.* **2004**, *121*, 9430-9435.

(128) Mchale, J., L.; edition, F., Ed. NJ, **1999**.

(129) *Molecular spectra;Molecular structure 3.Elelectronic spectra of polyatomic molecules.*; 1st ed.; Herzberg, G., Ed.; Van Nostr: New York, **1966**; Vol. I.

(130) Leung, J. W. H.; Wang, X.; Cheung, A. S. C. *J. Chem. Phys.* **2002**, *117*, 3694-3700.

(131) Ayles, V. L.; Muzangwa, L. G.; Reid, S. A. *Chem. Phys. Lett.* **2010**, *497*, 168-171.

(132) Hirao, T.; Dufour, C.; Pinchemel, B.; Bernath, P. F. *J. Mol. Spectrosc.* **2000**, *202*, 53-59.

(133) Poclet, A.; Krouti, Y.; Hirao, T.; Pinchemel, B.; Bernath, P. F. *J. Mol. Spectrosc.* **2000**, *204*, 125-132.

(134) Krouti, Y.; Poclet, A.; Hirao, T.; Pinchemel, B.; Bernath, P. F. *J. Mol. Spectrosc.* **2001**, *210*, 41-50.

(135) Dufour, C.; Carette, P.; Pinchemel, B. *J. Mol. Spectrosc.* **1991**, *148*, 303-9.

(136) Bouddou, A.; Dufour, C.; Pinchemel, B. *J. Mol. Spectrosc.* **1994**, *168*, 477-82.

(137) Dufour, C.; Pinchemel, B. *J. Mol. Spectrosc.* **1995**, *173*, 70-8.

(138) Hougen, J. T. *Journal of Molecular Spectroscopy* **2011**, *267*, 23-35.

(139) Rothschopf, G. K.; Morse, M. D. *Journal of Physical Chemistry A* **2005**, *109*, 11358-11364.

(140) Jin, J.; Chen, Y.; Yang, X. L.; Ran, Q.; Chen, C. X. *Journal of Molecular Spectroscopy* **2001**, *208*, 18-24.

(141) Millar, T. J.; Herbst, E. *Astronomy and Astrophysics* **1994**, *288*, 561-571.

(142) Thaddeus, P.; McCarthy, M. C.; Travers, M. J.; Gottlieb, C. A.; Chen, W. *Faraday Discussions* **1998**, *109*, 121-135.

(143) Atkinson, R.; Baulch, D. L.; Cox, R. A.; Hampson, R. F.; Kerr, J. A.; Troe, J. *Planetary and Space Science* **1989**, *37*, 1605-1620.

(144) Copeland, L. R.; Mohammad, F.; Zahedi, M.; Volman, D. H.; Jackson, W. M. *Journal of Chemical Physics* **1992**, *96*, 5817-5826.

(145) Lander, D. R.; Unfried, K. G.; Glass, G. P.; Curl, R. F. *Journal of Physical Chemistry* **1990**, *94*, 7759-7763.

(146) Hoobler, R. J.; Leone, S. R. *Journal of Geophysical Research-Planets* **1997**, *102*, 28717-28723.

(147) Hoobler, R. J.; Opansky, B. J.; Leone, S. R. *Journal of Physical Chemistry A* **1997**, *101*, 1338-1342.

(148) Mebel, A. M.; Halasz, G. J.; Vibok, A.; Alijah, A.; Baer, M. *Journal of Chemical Physics* **2002**, *117*, 991-1000.

(149) Dickman, R. L.; Somerville, W. B.; Whittet, D. C. B.; Mcnally, D.; Blades, J. C. *Astrophysical Journal Supplement Series* **1983**, *53*, 55-72.

(150) Miller, J. A.; Bowman, C. T. *Progress in Energy and Combustion Science* **1989**, *15*, 287-338.

(151) Pople, A. a. L.-H., H.C. *Jornal of molecular physics* **1958**, *1*.

(152) Hougen, J. T. *Jornal of chemical physics* **1962**, *36*.

(153) Carrington, A., Fabris,A.R.,Howard,B.J.,and Lucus,N.J. *Molecular Physics* **1971**, *20*.

(154) Brown, J. M. *jornal of molecular spectroscopy* **1977**, *68*.

(155) Aarts, J. F. M. *Molecular Physics* **1978**, *35*.

(156) Jungen, C.; Merer, A. J. *Molecular Physics* **1980**, *40*, 1-23.

(157) Brown, J. M.; Jorgensen, F. *Molecular Physics* **1982**, *47*, 1065-1086.

(158) Merer, A. J. a. T., D.N. *Can.J.phys* **1965**, *43*, 1795.

(159) Hakuta, K.; Uehara, H. *Journal of Chemical Physics* **1983**, *78*, 6484-6489.

(160) Hakuta, K.; Uehara, H.; Kawaguchi, K.; Suzuki, T.; Kasuya, T. *Journal of Chemical Physics* **1983**, *79*, 1094-1095.

(161) Kakimoto, M.; Kasuya, T. *Journal of Molecular Spectroscopy* **1982**, *94*, 380-392.

(162) Brazier, C. R.; Obrien, L. C.; Bernath, P. F. *Journal of Chemical Physics* **1987**, *86*, 3078-3081.

(163) Oliphant, N.; Lee, A.; Bernath, P. F.; Brazier, C. R. *Journal of Chemical Physics* **1990**, *92*, 2244-2247.

(164) Kawaguchi, K.; Suzuki, T.; Saito, S.; Hirota, E.; Kasuya, T. *Journal of Molecular Spectroscopy* **1984**, *106*, 320-329.

(165) Kakimoto, M. a. K., T. *Jornal of molecular spectroscopy* **1980**, *94*, 380.

(166) Suzuki, T.; Saito, S.; Hirota, E. *Journal of Chemical Physics* **1985**, *83*, 6154-6157.

(167) Yamashita, K.; Morokuma, K. *Chemical Physics Letters* **1987**, *140*, 345-348.

(168) Bondybey, V. E.; English, J. H. *Jornal of Molecular Spectroscopy* **1978**, *70*.

(169) Ohshima, Y.; Endo, Y. *Journal of Molecular Spectroscopy* **1995**, *172*, 225-232.

(170) Kohguchi, H.; Ohshima, Y.; Endo, Y. *Journal of Chemical Physics* **1997**, *106*, 5429-5438.

(171) Feher, M.; Salud, C.; Maier, J. P. *Journal of Molecular Spectroscopy* **1991**, *145*, 246-250.

(172) Feher, M.; Salud, C.; Maier, J. P.; Merer, A. J. *Journal of Molecular Spectroscopy* **1991**, *150*, 280-281.

(173) Allen, M. D.; Evenson, K. M.; Gillett, D. A.; Brown, J. M. *Journal of Molecular Spectroscopy* **2000**, *201*, 18-29.

(174) Beaton, S. A.; Gillett, D. A.; Brown, J. M.; Feher, M.; Rohrbacher, A. *Journal of Molecular Spectroscopy* **2001**, *209*, 60-65.

(175) Gillett, D. A.; Brown, J. M. *Canadian Journal of Physics* **1994**, *72*, 1001-1006.

(176) Green, S. *Astrophysical Journal* **1980**, *240*, 962-967.

(177) Pd, R.; Chandra, P. *Journal of Chemical Physics* **2001**, *114*, 1589-1600.

(178) Mebel, A. M.; Kaiser, R. I. *Astrophysical Journal* **2002**, *564*, 787-791.

(179) Belbruno, J. J.; Tang, Z. C.; Smith, R.; Hobday, S. *Molecular Physics* **2001**, *99*, 957-967.

(180) Jin, L.; Ding, Y. H.; Wang, J.; Sun, C. C. *Journal of Computational Chemistry* **2006**, *27*, 883-893.

(181) Martin, J. M. L.; Taylor, P. R.; Francois, J. P.; Gijbels, R. *Chemical Physics Letters* **1994**, *226*, 475-483.

(182) Ehara, M.; Gour, J. R.; Piecuch, P. *Molecular Physics* **2009**, *107*, 871-880.

(183) Gabriel, W.; Reinsch, E. A.; Rosmus, P. *Chemical Physics Letters* **1994**, *231*, 13-17.

(184) Hill, J. G.; Mitrushchenkov, A.; Yousaf, K. E.; Peterson, K. A. *Journal of Chemical Physics* **2011**, *135*.

(185) Garand, E.; Yacovitch, T. I.; Neumark, D. M. *Journal of Chemical Physics* **2009**, *130*.

(186) Zhu, Z. Q.; Zhang, Z. Q.; Huang, C. S.; Pei, L. S.; Chen, C. X.; Chen, Y. *Journal of Physical Chemistry A* **2003**, *107*, 10288-10291.

(187) Wang, J.; Ding, Y. H.; Sun, C. C. *Chemphyschem* **2005**, *6*, 431-433.

(188) Ding, Y. Q.; Fang, D. C.; Liu, R. Z. *Molecular Physics* **2005**, *103*, 767-774.

(189) Bettens, R. P. A.; Herbst, E. *Astrophysical Journal* **1997**, *478*, 585-593.

(190) Cernicharo, J.; Guelin, M.; Kahane, C. *Astronomy & Astrophysics Supplement Series* **2000**, *142*, 181-215.

(191) Broten, N. W.; Macleod, J. M.; Avery, L. W.; Irvine, W. M.; Hoglund, B.; Friberg, P.; Hjalmarson, A. *Astrophysical Journal* **1984**, *276*, L25-L29.

(192) Bell, M. B.; Feldman, P. A.; Travers, M. J.; McCarthy, M. C.; Gottlieb, C. A.; Thaddeus, P. *Astrophysical Journal* **1997**, *483*, L61-L64.

(193) Bell, M. B.; Watson, J. K. G.; Feldman, P. A.; Travers, M. J. *Astrophysical Journal* **1998**, *508*, 286-290.

(194) Ohishi, M.; Kaifu, N. *Faraday Discussions* **1998**, *109*, 205-216.

(195) Guelin, M.; Neininger, N.; Cernicharo, J. *Astronomy and Astrophysics* **1998**, *335*, L1-L4.

(196) Cherchneff, I.; Glassgold, A. E.; Mamon, G. A. *Astrophysical Journal* **1993**, *410*, 188-201.

(197) Doty, S. D.; Leung, C. M. *Astrophysical Journal* **1998**, *502*, 898-908.

(198) Kaiser, R. I.; Ochsenfeld, C.; Head-Gordon, M.; Lee, Y. T. *Science* **1998**, *279*, 1181-1184.

(199) Balucani, N.; Asvany, O.; Huang, L. C. L.; Lee, Y. T.; Kaiser, R. I.; Osamura, Y.; Bettinger, H. F. *Astrophysical Journal* **2000**, *545*, 892-906.

(200) Balucani, N.; Asvany, O.; Chang, A. H. H.; Lin, S. H.; Lee, Y. T.; Kaiser, R. I.; Osamura, Y. *Journal of Chemical Physics* **2000**, *113*, 8643-8655.

(201) Balucani, N.; Alagia, M.; Cartechini, L.; Casavecchia, P.; Volpi, G. G.; Sato, K.; Takayanagi, T.; Kurosaki, Y. *Journal of the American Chemical Society* **2000**, *122*, 4443-4450.

(202) Fuchs, G. W.; Fuchs, U.; Giesen, T. F.; Wyrowski, F. *Astronomy & Astrophysics* **2004**, *426*, 517-521.

(203) *The Identification of Molecular Spectra*; 4th ed.; Pearse, W. B.; Gaydon, A. G., Eds.; Chapman Hall London, **1976**.

(204) LeBlanc, F. J. *Journal Of Chemical Physics* **1968**, *48*.

(205) Politzer, P.; Lane, P.; Concha, M. C.; Ma, Y. G.; Murray, J. S. *Journal of Molecular Modeling* **2007**, *13*, 305-311.

(206) Petty, C. C.; Jayakumar, R. J.; Makowski, M. A.; Holcomb, C. T.; Humphreys, D. A.; La Haye, R. J.; Luce, T. C.; Politzer, P. A.; Prater, R.; Wade, M. R.; Welander, A. S. *Nuclear Fusion* **2012**, *52*.

(207) Politzer, P.; Murray, J. S. *Theoretical Chemistry Accounts* **2012**, *131*.

(208) Sinnokrot, M. O.; Valeev, E. F.; Sherrill, C. D. *Journal of the American Chemical Society* **2002**, *124*, 10887-10893.

(209) Hunter, C. A.; Sanders, J. K. M. *Journal of the American Chemical Society* **1990**, *112*, 5525-5534.

(210) Hunter, C. A.; Meah, M. N.; Sanders, J. K. M. *Journal of the American Chemical Society* **1990**, *112*, 5773-5780.

(211) Sinnokrot, M. O.; Sherrill, C. D. *Journal of Physical Chemistry A* **2004**, *108*, 10200-10207.

(212) Chipot, C.; Jaffe, R.; Maigret, B.; Pearlman, D. A.; Kollman, P. A. *Journal of the American Chemical Society* **1996**, *118*, 11217-11224.

(213) Ringer, A. L.; Sinnokrot, M. O.; Lively, R. P.; Sherrill, C. D. *Chemistry-a European Journal* **2006**, *12*, 3821-3828.

(214) Sinnokrot, M. O.; Sherrill, C. D. *Journal of Physical Chemistry A* **2006**, *110*, 10656-10668.

(215) Smith, T.; Slipchenko, L. V.; Gordon, M. S. *Journal of Physical Chemistry A* **2008**, *112*, 5286-5294.

(216) *Weak Intermolecular Interactions in Chemistry and biology*; Hobza, P.; Zahradnik, R., Eds.; Elsevier: Amsterdam **1980**.

(217) *Intermolecular Forces and their Evaluation by perturbation Theory*; 1st ed.; Arrighini, P., Ed.; Verlag Berlin, **1981**.

(218) *The CH/ π Interaction: Evidence, Nature , and Concequences* Second ed.; Motohiro, N.; Minoru, H.; Yoji, U., Eds.; Wiley-VCH: USA, **1998**.

(219) Duschinsky, F. *Acta physicochim URSS* **1937**, *7*, 551.

(220) Sando, G. S.; Spears, K. G.; Hupp, J. T. *J. Phys Chem A* **2001**, *105*, 5317.

(221) Yamakawa, M.; Yamada, I.; Noyori, R. *Angewandte Chemie-International Edition* **2001**, *40*, 2818-2821.

(222) Nishio, M. *Tetrahedron* **2005**, *61*, 6923-6950.

(223) Bertani, R.; Sgarbossa, P.; Venzo, A.; Lelj, F.; Amati, M.; Resnati, G.; Pilati, T.; Metrangolo, P.; Terraneo, G. *Coordination Chemistry Reviews* **2010**, *254*, 677-695.

(224) Nishio, M. *Journal of Molecular Structure* **2012**, *1018*, 2-7.

(225) Grabowski, S. J. *Chemical Reviews* **2011**, *111*, 2597-2625.

(226) Legon, A. C.; Millen, D. J. *Chemical Society Reviews* **1992**, *21*, 71-78.

(227) Del Bene, J. E.; Jordan, M. J. T. *International Reviews in Physical Chemistry* **1999**, *18*, 119-162.

(228) Pimentel, G. C.; McClellan, A. L. *The hydrogen bond*; W.H. Freeman; trade distributor: Reinhold Pub. Corp., New York: San Francisco,**1960**.

(229) Schuster, P.; Zundel, G.; Sandorfy, C. *The hydrogen bond : recent developments in theory and experiments*; North-Holland Publishing Company: Amsterdam ; New York, **1976**.

(230) American Chemical Society. Meeting (206th : 1993 : Chicago Ill.); Smith, D. A.; American Chemical Society. Division of Computers in Chemistry. *Modeling the hydrogen bond*; American Chemical Society: Washington, DC, **1994**.

(231) Muraki, M. *Protein and Peptide Letters* **2002**, *9*, 195-209.

(232) Nakagawa, Y.; Irie, K.; Yanagita, R. C.; Ohigashi, H.; Tsuda, K. *Journal of the American Chemical Society* **2005**, *127*, 5746-5747.

(233) Ramirez-Gualito, K.; Alonso-Rios, R.; Quiroz-Garcia, B.; Rojas-Aguilar, A.; Diaz, D.; Jimenez-Barbero, J.; Cuevas, G. *Journal of the American Chemical Society* **2009**, *131*, 18129-18138.

(234) Nishio, M. *Physical Chemistry Chemical Physics* **2011**, *13*, 13873-13900.

(235) Cavallo, G.; Metrangolo, P.; Pilati, T.; Resnati, G.; Sansotera, M.; Terraneo, G. *Chemical Society Reviews* **2010**, *39*, 3772-3783.

(236) Amendola, V.; Fabbrizzi, L.; Mosca, L. *Chemical Society Reviews* **2010**, *39*, 3889-3915.

(237) Thanthiriwatte, K. S.; Hohenstein, E. G.; Burns, L. A.; Sherrill, C. D. *Journal of Chemical Theory and Computation* **2011**, *7*, 88-96.

(238) Nishio, M.; Umezawa, Y.; Hirota, M. *Journal of Synthetic Organic Chemistry Japan* **1997**, *55*, 2-12.

(239) Auffinger, P.; Hays, F. A.; Westhof, E.; Ho, P. S. *Proc. Natl. Acad. Sci. U. S. A.* **2004**, *101*, 16789-16794.

(240) Voth, A. R.; Hays, F. A.; Ho, P. S. *Proc. Natl. Acad. Sci. U. S. A.* **2007**, *104*, 6188-6193.

(241) Nishio, M.; Hirota, M.; Umezawa, Y. *The CH-[pi] interaction : evidence, nature, and consequences*; Wiley: New York, **1998**.

(242) Desiraju, G. R.; Steiner, T. *The weak hydrogen bond : in structural chemistry and biology*; Oxford University Press: Oxford ; New York, **1999**.

(243) Zhang, Y.; Ji, B. M.; Tian, A. M.; Wang, W. Z. *Journal of Chemical Physics* **2012**, *136*.

(244) Arunan, E.; Desiraju, G. R.; Klein, R. A.; Sadlej, J.; Scheiner, S.; Alkorta, I.; Clary, D. C.; Crabtree, R. H.; Dannenberg, J. J.; Hobza, P.; Kjaergaard, H. G.; Legon, A. C.; Mennucci, B.; Nesbitt, D. J. *Pure and Applied Chemistry* **2011**, *83*, 1619-1636.

(245) Metrangolo, P.; Resnati, G. *Science* **2008**, *321*, 918-919.

(246) Sredojevic, D.; Bogdanovic, G. A.; Tomic, Z. D.; Zaric, S. D. *Crystengcomm* **2007**, *9*, 793-798.

(247) Zhu, S.; Xing, C.; Xu, W.; Jin, G.; Li, Z. *Crystal Growth and Design* **2004**, *4*, 53-56.

(248) Zhu, S.; Xing, C.; Xu, W.; Li, Z. *Tetrahedron Letters* **2004**, *45*, 777-780.

(249) Law, K. S.; Schauer, M.; Bernstein, E. R. *Journal of Chemical Physics* **1984**, *81*, 4871-4882.

(250) Squire, D. W.; Bernstein, R. B. *Journal of Physical Chemistry* **1984**, *88*, 4944-4952.

(251) Tsuzuki, S.; Honda, K.; Uchimaru, T.; Mikami, M.; Tanabe, K. *Journal of the American Chemical Society* **2000**, *122*, 3746-3753.

(252) Burns, L. A.; Vazquez-Mayagoitia, A.; Sumpter, B. G.; Sherrill, C. D. *Journal of Chemical Physics* **2011**, *134*, 084107.

(253) Clark, T.; Hennemann, M.; Murray, J. S.; Politzer, P. *Journal of Molecular Modeling* **2007**, *13*, 291-296.

(254) Politzer, P.; Lane, P.; Concha, M. C.; Ma, Y.; Murray, J. S. *Journal of Molecular Modeling* **2007**, *13*, 305-311.

(255) Politzer, P.; Murray, J. S.; Concha, M. C. *Journal of Molecular Modeling* **2007**, *13*, 643-650.

(256) Politzer, P. *Halogen Bonding: Fundamentals and Applications. Structure and Bonding, 126 edited by Pierangelo Metrangolo and Giuseppe Resnati*, **2008**; Vol. 130.

(257) Ringer, A. L.; Figgs, M. S.; Sinnokrot, M. O.; Sherrill, C. D. *Journal of Physical Chemistry A* **2006**, *110*, 10822-10828.

(258) Sherrill, C. D.; Sumpter, B. G.; Sinnokrot, M. O.; Marshall, M. S.; Hohenstein, E. G.; Walker, R. C.; Gould, I. R. *Journal of Computational Chemistry* **2009**, *30*, 2187-2193.

(259) Arunan, E.; Gutowsky, H. S. *Journal of Chemical Physics* **1993**, *98*, 4294-4296.

(260) Chandrasekaran, V.; Biennier, L.; Arunan, E.; Talbi, D.; Georges, R. *Journal of Physical Chemistry A* **2011**, *115*, 11263-11268.

(261) Hobza, P.; Selzle, H. L.; Schlag, E. W. *Chemical Reviews* **1994**, *94*, 1767-1785.

(262) Tsuzuki, S.; Honda, K.; Uchimaru, T.; Mikami, M.; Tanabe, K. *Journal of Physical Chemistry A* **2002**, *106*, 4423-4428.

(263) Tsuzuki, S.; Honda, K.; Uchimaru, T.; Mikami, M.; Tanabe, K. *Journal of the American Chemical Society* **2002**, *124*, 104-112.

(264) Tsuzuki, S.; Uchimaru, T.; Sugawara, K.; Mikami, M. *Journal of Chemical Physics* **2002**, *117*, 11216-11221.

(265) Wheeler, S. E. *Journal of the American Chemical Society* **2011**, *133*, 10262-10274.

(266) Wheeler, S. E.; Houk, K. N. *Journal of the American Chemical Society* **2008**, *130*, 10854-+.

(267) Lu, Y. X.; Zou, J. W.; Wang, Y. H.; Yu, Q. S. *Chemical Physics* **2007**, *334*, 1-7.

(268) Cheng, L.; Wang, M. Y.; Wu, Z. J.; Su, Z. M. *Journal of Computational Chemistry* **2007**, *28*, 2190-2202.

(269) Lu, Y. X.; Zou, J. W.; Wang, Y. H.; Jiang, Y. J.; Yu, Q. S. *Journal of Physical Chemistry A* **2007**, *111*, 10781-10788.

(270) Metrangolo, P.; Meyer, F.; Pilati, T.; Resnati, G.; Terraneo, G. *Angewandte Chemie-International Edition* **2008**, *47*, 6114-6127.

(271) Metrangolo, P.; Neukirch, H.; Pilati, T.; Resnati, G. *Accounts of Chemical Research* **2005**, *38*, 386-395.

(272) Parisini, E.; Metrangolo, P.; Pilati, T.; Resnati, G.; Terraneo, G. *Chemical Society Reviews* **2011**, *40*, 2267-2278.

(273) Politzer, P.; Murray, J. S.; Clark, T. *Physical Chemistry Chemical Physics* **2010**, *12*, 7748-7757.

(274) Liu, B. K.; Wang, B. X.; Wang, Y. Q.; Wang, L. *Chemical Physics Letters* **2009**, *477*, 266-270.

(275) Di Palma, T. M.; Bende, A.; Borghese, A. *Chemical Physics Letters* **2010**, *495*, 17-23.

(276) Musgrave, A.; Wright, T. G. *Journal of Chemical Physics* **2005**, *122*.

(277) Ishikawa, S.; Ebata, T.; Ishikawa, H.; Inoue, T.; Mikami, N. *Journal of Physical Chemistry* **1996**, *100*, 10531-10535.

(278) Rademann, K.; Brutschy, B.; Baumgartel, H. *Chemical Physics* **1983**, *80*, 129-145.

(279) Dimopoulourademann, U.; Rademann, K.; Bisling, P.; Brutschy, B.; Baumgartel, H. *Berichte Der Bunsen-Gesellschaft-Physical Chemistry Chemical Physics* **1984**, *88*, 215-217.

(280) Even, U.; Rademann, K.; Jortner, J.; Manor, N.; Reisfeld, R. *Physical Review Letters* **1984**, *52*, 2164-2167.

(281) Leist, R.; Frey, J. A.; Ottiger, P.; Frey, H. M.; Leutwyler, S.; Bachorz, R. A.; Klopper, W. *Angewandte Chemie-International Edition* **2007**, *46*, 7449-7452.

(282) Leist, R.; Frey, J. A.; Leutwyler, S. *Journal of Physical Chemistry A* **2006**, *110*, 4180-4187.

(283) Hobza, P.; Spirko, V.; Havlas, Z.; Buchhold, K.; Reimann, B.; Barth, H. D.; Brutschy, B. *Chemical Physics Letters* **1999**, *299*, 180-186.

(284) Hobza, P.; Selzle, H. L.; Schlag, E. W. *Journal of Chemical Physics* **1993**, *99*, 2809-2811.

(285) Lu, W. Y.; Hu, Y. H.; Lin, Z. Y.; Yang, S. H. *Journal of Chemical Physics* **1996**, *104*, 8843-8851.

(286) Yeh, J. H.; Shen, T. L.; Nocera, D. G.; Leroi, G. E.; Suzuka, I.; Ozawa, H.; Namuta, Y. *Journal of Physical Chemistry* **1996**, *100*, 4385-4389.

(287) Sugawara, K.; Miyawaki, J.; Nakanaga, T.; Takeo, H.; Lembach, G.; Djafari, S.; Barth, H. D.; Brutschy, B. *Journal of Physical Chemistry* **1996**, *100*, 17145-17147.

(288) Yamamoto, N.; Hino, K.; Mogi, K.; Ohashi, K.; Sakai, Y.; Sekiya, H. *Chemical Physics Letters* **2001**, *342*, 417-424.

(289) Yamamoto, N.; Ohashi, K.; Hino, K.; Izutsu, H.; Mogi, K.; Sakai, Y.; Sekiya, H. *Chemical Physics Letters* **2001**, *345*, 532-538.

(290) Numata, Y.; Ishii, Y.; Watahiki, M.; Suzuka, I.; Ito, M. *Journal of Physical Chemistry* **1993**, *97*, 4930-4935.

(291) Bieske, E. J.; Rainbird, M. W.; Atkinson, I. M.; Knight, A. E. W. *Journal of Chemical Physics* **1989**, *91*, 752-761.

(292) Kwon, C. H.; Kim, H. L.; Kim, M. S. *Journal of Chemical Physics* **2002**, *116*, 10361-10371.

(293) Lembach, G.; Brutschy, B. *Chemical Physics Letters* **1997**, *273*, 421-428.

(294) Mons, M.; Lecalve, J.; Piuzzi, F.; Dimicoli, I. *Journal of Chemical Physics* **1990**, *92*, 2155-2165.

(295) Munteanu, C. R.; Cacheiro, J. L.; Fernandez, B.; Makarewicz, J. *Journal of Chemical Physics* **2004**, *121*, 1390-1396.

(296) Oh, J. J.; Park, I.; Peebles, S. A.; Kuczkowski, R. L. *Journal of Molecular Structure* **2001**, *599*, 15-22.

(297) Oh, J. J.; Park, I.; Wilson, R. J.; Peebles, S. A.; Kuczkowski, R. L.; Kraka, E.; Cremer, D. *Journal of Chemical Physics* **2000**, *113*, 9051-9059.

(298) Durant, J. L.; Rider, D. M.; Anderson, S. L.; Proch, F. D.; Zare, R. N. *Journal of Chemical Physics* **1984**, *80*, 1817-1825.

(299) Koplitz, B. D.; Mcvey, J. K. *Journal of Chemical Physics* **1984**, *80*, 2271-2282.

(300) Koplitz, B. D.; Mcvey, J. K. *Journal of Chemical Physics* **1984**, *81*, 4963-4968.

(301) Szaflarski, D. M.; Simon, J. D.; Elsayed, M. A. *Journal of Physical Chemistry* **1986**, *90*, 5050-5058.

(302) Murakami, J.; Kaya, K.; Ito, M. *Journal of Chemical Physics* **1980**, *72*, 3263-3270.

(303) Bieske, E. J.; Rainbird, M. W.; Knight, A. E. W. *Journal of Chemical Physics* **1989**, *90*, 2068-2069.

(304) Tonokura, K.; Nakamura, T.; Koshi, M. *Analytical Sciences* **2003**, *19*, 1109-1113.

(305) Frisch; GAUSSIAN 09 Rev.A: **2009**.

(306) Dreuw, A.; Weisman, J. L.; Head-Gordon, M. *Journal of Chemical Physics* **2003**, *119*, 2943-2946.

(307) Chai, J. D.; Head-Gordon, M. *Journal of Chemical Physics* **2009**, *131*.

(308) Yanai, T.; Tew, D. P.; Handy, N. C. *Chemical Physics Letters* **2004**, *393*, 51-57.

(309) Peach, M. J. G.; Helgaker, T.; Salek, P.; Keal, T. W.; Lutnaes, O. B.; Tozer, D. J.; Handy, N. C. *Physical Chemistry Chemical Physics* **2006**, *8*, 558-562.

(310) Mardirossian, N.; Parkhill, J. A.; Head-Gordon, M. *Physical Chemistry Chemical Physics* **2011**, *13*, 19325-19337.

(311) Wright, T. G.; Panov, S. I.; Miller, T. A. *Journal of Chemical Physics* **1995**, *102*, 4793-4803.

(312) Heger, H. J.; Boesl, U.; Zimmermann, R.; Dorfner, R.; Kettrup, A. *European Mass Spectrometry* **1999**, *5*, 51-57.

(313) Heger, H. J.; Zimmermann, R.; Dorfner, R.; Beckmann, M.; Griebel, H.; Kettrup, A.; Boesl, U. *Analytical Chemistry* **1999**, *71*, 46-57.

(314) Imhof, P.; Kleinermanns, K. *Chemical Physics* **2001**, *270*, 227-236.

(315) Walter, K.; Scherm, K.; Boesl, U. *Journal of Physical Chemistry* **1991**, *95*, 1188-1194.

(316) Potts, A. W.; Evardsson, D.; Karlsson, L.; Holland, D. M. P.; MacDonald, M. A.; Hayes, M. A.; Maripuu, R.; Seigbahn, K.; von Niessen, W. *Chemical Physics* **2000**, *254*, 385-405.

(317) Holland, D. M. P.; Edvardsson, D.; Karlsson, L.; Maripuu, R.; Siegbahn, K.; Potts, A. W.; von Niessen, W. *Chemical Physics* **2000**, *253*, 133-155.

(318) Cybulski, S. M.; Lytle, M. L. *Journal of Chemical Physics* **2007**, *127*.

(319) Jurecka, P.; Sponer, J.; Cerny, J.; Hobza, P. *Physical Chemistry Chemical Physics* **2006**, *8*, 1985-1993.

(320) Diri, K.; Krylov, A. I. *Journal of Physical Chemistry A* **2012**, *116*, 653-662.

(321) Amicangelo, J. C. *Journal of Physical Chemistry A* **2005**, *109*, 9174-9182.

(322) Western, C.; 7.1.108 ed. University of Bristol, 2010.

(323) Tauer, T. P.; Sherrill, C. D. *Journal of Physical Chemistry A* **2005**, *109*, 10475-10478.

(324) Hammond, C. J.; Ayles, V. L.; Bergeron, D. E.; Reid, K. L.; Wright, T. G. *Journal of Chemical Physics* **2006**, *125*.